

On the factors impacting the mechanical response of nanoporous gold-polymer composites

**Vom Promotionsausschuss der
Technischen Universität Hamburg**
zur Erlangung des akademischen Grades
Doktor-Ingenieur (Dr.-Ing.)
genehmigte Dissertation

von

Murilo Pereira Hablitzel

aus

Florianópolis, Brasilien

2022

Gutachter der Dissertation:

Prof. Dr Erica Lilleodden

*Institute of Materials Research, Materials Mechanics
Helmholtz-Zentrum Hereon, Germany*

Prof. Dr.-Ing. habil Alexander Düster

*Institute for Ship Structural Design and Analysis
Hamburg University of Technology, Germany*

Vorsitzender des Prüfungsausschusses:

Prof. Dr.-Ing. Bodo Fiedler

*Institute of Polymer Composites
Hamburg University of Technology, Germany*

Tag der mündlichen Prüfung:

17. Dezember 2021

DOI: <https://doi.org/10.15480/882.4110>

Acknowledgements

First and foremost, I want to sincerely thank my PhD advisor, Prof. Dr Erica Lilleodden, for the encouragement and guidance during my time at her department. Her passion for science, enthusiasm and scientific integrity shaped this work and my future career. I will be forever grateful for our time working together and her effort in my scientific development.

I would like to express my genuine gratitude to all the people who contributed to the success of this work. My sincere thanks to Dr Heike Gabrisch and Dr.-Ing. Henry Ovri for the support with TEM experiments and Dr Ingo Scheider for the guidance on my first steps with finite element simulations. Also, I extend my gratitude to Prof. Dr.-Ing. habil Alexander Düster for agreeing to review this work and his valuable suggestions regarding my thesis.

I would like to thank all my colleagues in the department of Experimental Materials Mechanics in Helmholtz Zentrum Hereon for their encouragement and friendship. It was a great pleasure to explore the fascinating world of micromechanics alongside such a fantastic team.

I am grateful for the time spent with all my colleagues in other departments of Helmholtz Zentrum Hereon and Integriertes Graduiertenkolleg (MGK). Financial support from the German Research Foundation (DFG) through SFB 986 Tailor-Made Multi-Scale Materials Systems project B4 is gratefully acknowledged.

Lastly, I express my profound thanks to my family for their encouragement, love and patience. My special thanks to my parents for providing the basis I needed to grow into the person I am today and to my beloved wife for being the light of my days and supporting me always.

Abstract

Nanoporous gold (NPG) is a bicontinuous network of nanoscale gold ligaments and pores, the dimensions of which can be adjusted to exploit strengthening at small ligament sizes. Nevertheless, its mechanics are limited by the lack of ductility under tensile loading. Recently, the impregnation of the open porous structure with an epoxy phase created a metal-polymer composite that combined strengthening at small structural length-scales with enhanced tensile ductility. The present work aims to clarify the effect of factors influencing the mechanical behaviour of composite materials, particularly the properties of the epoxy phase and interface – properties that are still unexplored in NPG-epoxy composites. To this end, a series of novel approaches were developed to investigate the independent contribution of each factor, focusing on the development of representative model samples, micromechanical testing, and finite element simulation.

A novel method to understand the effect of the composite microstructure in the epoxy was made possible by isolating the matrix phase. Taking inspiration from mining techniques, an approach based on gold etching in iodine-iodide solutions successfully leached out the Au from NPG-polymer composites. The remaining bi-continuous open porous polymer (NPP) was investigated using nanoindentation to explore possible size effects as those found in nanoporous gold. The interface was investigated using a model system where a single planar boundary between gold and epoxy was achieved. Using both nanoindentation approaches and novel microshear experiments, the interphase regime and interfacial strength were measured. Moreover, the experimental results inspired a modelling approach of the interfaces for finite element simulations, which was employed to study the interfacial behaviour as a function of the balance between the properties of constituent phases and interfaces. The interfacial model was also employed to simulate the effect of the interfacial strength on the mechanical response and delamination evolution of NPG-epoxy composites.

The findings from the investigations on the isolated factors improved the interpretation of the composite mechanical response. No evidence of a structural length-scale effect in the polymer was found, and the response of the isolated polymer phase could be well predicted by an isostrain law applied to the properties measured on the bulk polymer. Furthermore, no evidence supporting the presence of an interlayer was found between the gold and epoxy phases. The measurement of the interfacial strength showed that the interface in NPG-epoxy composite is the weakest link in the composite's deformation, which was also observed in the simulations. The isolated effect of the interfacial properties was attenuated in the composite by the interconnected structure, which in compression allows the load transfer even after interface failure.

Zusammenfassung

Nanoporöses Gold (NPG) ist ein bikontinuierliches Netzwerk aus nanoskaligen Ligamenten und Poren, deren Dimensionen eingestellt werden können, um die Festigkeitserhöhung bei kleinen Ligamentgrößen auszunutzen. Dennoch ist seine Mechanik durch einen Mangel an Duktilität unter Zugbelastung limitiert. Kürzlich brachte die Imprägnierung der offen-porösen Struktur mit einer Epoxidharz-Phase ein Metall-Polymer Komposit hervor, welches Festigkeitserhöhung bei kleinen strukturellen Längenskalen mit verbesserter Zugduktilität verbindet. Die vorliegende Arbeit zielt darauf ab, den Effekt von Faktoren zu klären, die das mechanische Verhalten von Kompositmaterialien beeinflussen, insbesondere die Eigenschaften der Epoxidharz-Phase und der Grenzfläche - Eigenschaften, die immer noch unerforscht sind in NPG-Epoxidharz Kompositen. Zu diesem Zweck wurden eine Reihe von neuartigen Vorgehensweisen entwickelt, um den unabhängigen Beitrag jeden Faktors zu untersuchen, mit dem Fokus auf die Entwicklung repräsentativer Modellproben, mikromechanischer Tests, und Finite Elemente Simulationen.

Eine neuartige Methode zum Verständnis des Effektes der Kompositmikrostruktur im Epoxidharz wurde möglich gemacht durch die Absonderung der Matrixphase. In Anlehnung an Bergbautechniken wurde das Gold erfolgreich mittels einer Jod-Jodid Ätzlösung aus NPG-Polymer Kompositen ausgewaschen. Das verbleibende bikontinuierliche offen-poröse Polymer (NPP) wurde mit Nanoindentation untersucht, um mögliche Größeneffekte zu erforschen, wie solche, die in NPG gefunden wurden. Die Grenzfläche wurde durch ein Modellsystem untersucht, in dem eine einzelne, ebene Grenze zwischen Gold und Epoxidharz verwirklicht wurde. Unter Verwendung von sowohl Nanoindentationsansätzen als auch neuartigen Mikroscherungsexperimenten wurden der Interphasenbereich und die Grenzflächenstärke gemessen. Darüber hinaus regten die experimentellen Ergebnisse einen Modellierungsansatz der Grenzflächen für Finite Elemente Simulationen an, der angewendet wurde, um das Grenzflächenverhalten als Funktion des Gleichgewichtes zwischen Eigenschaften der konstituierenden Phasen und der Grenzfläche zu studieren. Das Grenzflächenmodell wurde auch zur Simulation des Effektes der Grenzflächenfestigkeit auf die mechanische Antwort und Delaminationsentwicklung der NPG-Epoxidharz Komposite verwendet.

Die Ergebnisse aus den Untersuchungen der isolierten Faktoren verbesserten die Interpretation der mechanischen Antwort der Komposite. Es wurde kein Nachweis gefunden für einen strukturellen Längenskaleneffekt im Polymer, und die Antwort der isolierten Polymerphase konnte vorhergesagt werden durch ein Isostraininggesetz, angewendet auf gemessene Bulk-Polymereigenschaften. Desweiteren wurden keine Anzeichen gefunden für die Anwesenheit einer

Interphase zwischen der Gold und der Epoxidharz Phase Die Messung der Grenzflächenfestigkeit zeigte, dass die Grenzfläche in NPG-Epoxidharz Kompositen das schwächste Glied in der Kompositverformung ist, was auch in den Simulation beobachtet wurde. Der isolierte Effekt der Grenzflächeneigenschaften wurde im Komposit abgeschwächt durch die miteinander verbundenen Strukturen, die in Kompression den Lasttransfer selbst nach Grenzflächenversagen ermöglicht.

Content

1	Introduction.....	1
1.1	Motivation and objectives.....	1
1.2	Structure of the thesis.....	3
2	Background.....	5
2.1	Mechanics of NPG-polymer composites.....	5
2.1.1	Size effect in NPG	7
2.1.2	Size effect in polymers.....	8
2.1.3	Metal-polymer interface.....	9
2.2	Role of an interface in composite materials.....	11
3	Methods	15
3.1	Sample preparation	15
3.1.1	Nanoporous gold.....	15
3.1.2	NPG-polymer composite.....	16
3.1.3	Planar interface samples	17
3.1.4	Nanoporous polymer.....	18
3.2	Microstructural characterization	21
3.2.1	FIB-SEM dual system beam.....	21
3.2.2	TEM	23
3.3	Chemical analysis utilizing energy-dispersive x-ray spectroscopy	26
3.4	Micromechanical behaviour characterization	26
3.4.1	Nanoindentation.....	26
3.4.2	Microcompression.....	30
3.4.3	Interfacial shear test	33
3.5	FEM simulation.....	37
3.5.1	Boundary conditions and materials properties	39
4	The mechanical response of the polymeric phase.....	41
4.1	Considerations on the bulk polymer properties.....	41
4.2	Composites made from polymeric infiltration	44
4.2.1	Leaching of Au in NPG-polymer composites	45

4.2.2	Morphology of the isolated polymeric phase.....	47
4.2.3	Mechanics of the isolated polymer phase.....	49
4.3	Conclusions.....	52
5	On measuring the mechanical characteristics near the gold-epoxy interface.....	53
5.1	Interlayer formation.....	53
5.2	Local mechanical response near a planar interface.....	56
5.2.1	Line of indentations on the bulk materials.....	57
5.2.2	Properties crossing an inclined interface	61
5.2.3	Analysis of the transitional properties.....	64
5.3	Conclusions.....	69
6	The effect of the interfacial strength	71
6.1	Measuring the bonding strength between gold and epoxy.....	71
6.1.1	Failure mode identification	71
6.1.2	Interfacial shear strength.....	76
6.2	Finite element method for a gold-epoxy interface.....	79
6.2.1	Simulating the interfacial shear strength test.....	82
6.2.2	The effect of interfacial properties on the interfacial behaviour	85
6.3	Conclusions.....	90
7	The overall mechanical response of NPG-polymer composites.....	91
7.1	On the effect of the interfacial property	91
7.2	On the contribution of each individual phase.....	100
7.2.1	Considerations of the strengthening of the gold phase.....	103
7.3	Conclusions.....	109
8	Summary and future work.....	111
8.1	Summary.....	111
8.2	Suggestions for future work	113
	Bibliography	115
	Curriculum Vitae	131

Nomenclature

A	contact area of the indenter
A_o	area of the microcolumn
A_{int}	interfacial area
a	square root of the projected contact area
$C_{sneddon}$	compliance of the half-space materials
C3D8	8-node brick elements
C3D10	10-node quadratic tetrahedron
CSM	continuous stiffness measurement
CSMAX	maximum stress-based damage initiation criterion for cohesive surfaces
D	diameter of the microcolumn
D_p	flat punch diameter
$\langle D \rangle$	mean ligament size of the NPG structure
D200S5	200 nm of indentation depth and spacing of 5 times the indentation depth
D300S7	300 nm of indentation depth and spacing of 7 times the indentation depth
D_{bottom}	diameter of the column at the bottom
D_s	damping coefficient
D_v	scalar damage variable
E	elastic modulus of the materials
E^*	complex modulus
E'	storage modulus
E''	loss modulus
E_{epoxy}	elastic modulus of epoxy
E_f	elastic modulus of the film
E_r	reduced elastic modulus
E_{gold}	elastic modulus of gold
E_i	elastic modulus of the indenter
E_s	elastic modulus of the substrate
EDS	energy-dispersive x-ray spectroscopy
FEA	finite element analysis
FEM	finite element method

FIB	focused ion beam
G_c	damage or the fracture energy
G_m	shear modulus of the matrix
h	contact depth of the indenter, displacement
h_{column}	displacement of the microcolumn
h_{LF}	load frame displacement
h_{max}	maximum displacement
h_{raw}	raw displacement
h_s	displacement of the surface
$h_{substrate}$	displacement of the substrate
$h_{surface}$	surface height identified at initial contact by the system
H	hardness
H_o	initial column height
H_0	null hypothesis
H_p	height of the polymeric part
HCS	harmonic contact stiffness
HRTEM	high-resolution TEM
ISE	indentation size effect
K	cohesive stiffness matrix
K_f	load frame stiffness of the nanoindentation instrument
K_s	spring stiffness
l	side of square cross-section microcolumn
l_f	length of a fibre
n	population size
NPG	nanoporous gold
NPP	nanoporous polymer
P	load
P_{column}	load applied on the microcolumn
P_{max}	maximum load
RV	representative volume
S	elastic contact stiffness
S_a	specific surface area
$S_{substrate}$	stiffness of the substrate
SEM	scanning electron microscope

t	nominal traction stress vector
t_f	film thickness
TEM	transmission electron microscopy
WD	work distance
\bar{x}	mean value
Y_n	interfacial strengths on the normal direction,
Y_s	interfacial strengths on the shear direction,
α	numerically determined scaling parameter
α_{int}	ratio between the interfacial strengths under tension and shear
β	constant that depends on the geometry of the indenter
$\dot{\gamma}_{gold}$	work hardening rate of gold
δ	separation
ϵ	constant of the indenter
ϵ_{eng}	engineering strain
ϵ_m	strain subjected to the matrix
ν	Poisson's ratio of the investigated materials
ν_f	Poisson's ratio of the film
ν_i	Poisson's ratio of the indenter
ν_s	Poisson's ratio of the substrate
σ	standard deviation
σ_{eng}	engineering stress
σ_f	fibre axial stress
σ_y^{loc}	local strength
$\sigma_{y,epoxy}$	yield stress of epoxy
$\sigma_{y,gold}$	yield stress of gold
τ_{45°	shear stress at the 45° plane
τ_i	shear stress at the interface
ω	harmonic frequency

1 Introduction

1.1 Motivation and objectives

Nanoporous gold (NPG) is an ideal model material for studying nanoscale plasticity and size-dependent mechanical response [1–4]. The bicontinuous network made of nanoscale gold ligaments is tailorable in structural length-scale, and it is relatively easy to fabricate. More recently, the interest in NPG has increased due to potential applications in catalysis, sensing, and actuation. The promising NPG functionality originates from the nanoscale porosity, high surface area to volume ratio, and large reversible strain amplitude [5–7]. Nevertheless, understanding the mechanical behaviour is a critical aspect of any NPG application.

The mechanical response of NPG exhibits tension-compression asymmetry due to densification under compression with stable and uniform plastic flow but density reduction under tension with brittle failure of NPG structure. Recently, a new design strategy was developed as an alternative to improve the NPG tensile ductility. It consisted of infiltrating epoxy into the pore volume of NPG samples, which enhanced the stress distribution under loading, improving the tensile ductility [8]. It was observed that the NPG network maintains its geometry, and the polymer impregnation forms an interpenetrating phase of a continuous polymer network. Therefore, NPG-polymer composites are bicontinuous network structures with a structural length scale dictated by the initial NPG sample [9, 10]. The mechanics of the NPG-polymer composites is dependent on NPG's microstructural parameters, such as ligament relative density and mean ligament size. Mechanical characterizations using micromechanical techniques have shown that a weaker size effect is observed in the hardness and yield strength than pure NPG and bulk gold. Also, the elastic response shows the influence of the NPG load-bearing ligament structure connectivity [11].

The mechanical response of NPG-polymer composite, as a composite material, is a function of the reinforcement phase, i.e., the interconnected Au ligament network, the matrix, i.e., the continuous polymer structure, and the interface's capacity to transfer load between the phases. Much of the understanding of its mechanical behaviour comes from characterisation efforts performed on the NPG previously to the polymer infiltration, and the contributions of the

polymeric phase and the interface properties remain unexplored. Initiatives to investigate the independent contribution of each one of the pieces are complicated due to the complex geometry and structural length scale of the interconnected phases. Here, the contributions of the polymeric phase and interface are investigated in NPG-polymer composites. The interaction with the NPG geometry is circumvented by utilizing model samples with simplified geometry and physically isolating the composite's polymeric phase. Furthermore, the composite geometry impact in the constituent phases and their interaction in the interfacial behaviour is analysed in the composites' overall mechanics. Hence, four basic questions are raised:

1. How do the small length-scales affect the properties of the polymeric phase within the composite structure?
2. How does a gold-polymer interface affect the nearby local mechanical characteristics?
3. How does the bonding strength affect the interfacial behaviour?
4. What is the influence of the interface properties in the NPG-epoxy composites?

The present thesis is focused on the above four questions for composites made of the infiltration of epoxy into NPG structures. A four-fold investigation of the composite was carried out as illustrated in Figure 1.1, focusing on polymer phase characterization, interface characterization, FEM (finite element method) interfacial modelling and composite properties. Additionally, the effect of the ligament structure on the dislocation activity of NPG is discussed based on experimental results. The scientist approaches of the present thesis are as follows:

- Develop a processing route for nanoporous polymer (NPP), which consists of leaching the Au from NPG-polymer composites, maintaining the geometry and length-scale of the polymeric phase intact. Characterize NPP structures with contrasting structural length-scale using micromechanical techniques to elucidate its mechanical behaviour and potential size effects. Establish an approach to predict the polymeric phase's contribution in the composite response based on the bulk polymer property and the respective volume fraction.
- Investigate the interface between gold and epoxy to detect material properties variation (i.e., the presence of an interphase) or if the measurement of properties shows variation with the proximity to the interface.
- Develop a methodology to measure the interfacial strength of gold-epoxy model samples with a simplified geometry. Evaluate the influence of a size-dependent response according to the interfacial area.
- Develop an approach to model the interface of gold-epoxy systems for finite element simulations. Clarify the influence of the interfacial properties on the mechanical behaviour of the model samples and extrapolate to the analysis of NPG-epoxy composites.

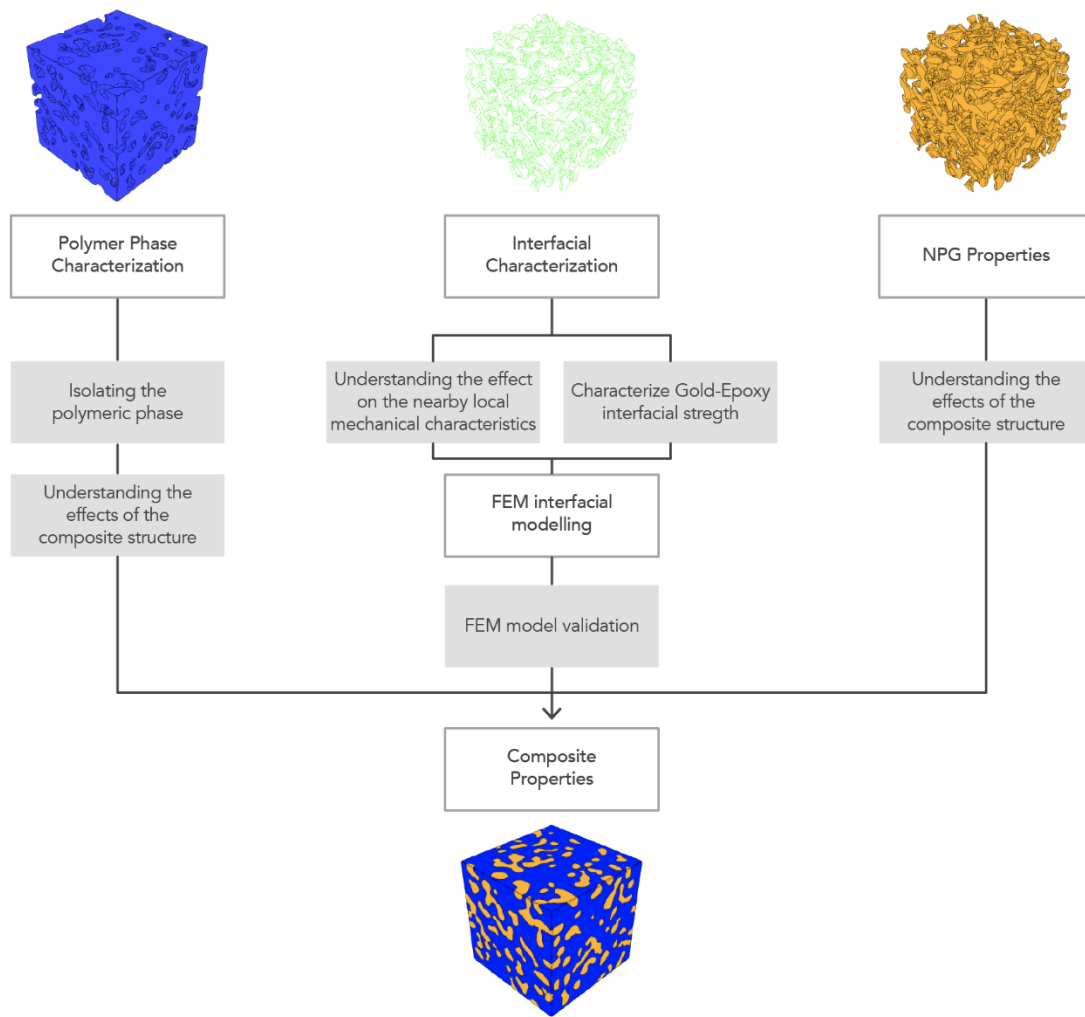


Figure 1.1: Schematic view of the scientific approaches to approach the independent objectives in this thesis and their combination in understanding the composite response.

1.2 Structure of the thesis

Based on the objectives and the scientific approaches, this thesis is structured as follows:

- In Chapter 2, the thesis's background is presented, including the mechanics of NPG composites and the size-dependent mechanical response of its constituent phases. The metal-polymer interface is also introduced, showing experimental work in NPG-epoxy composites. Lastly, the mechanical influence of the interface is reviewed in reinforced composites.
- Chapter 3 introduces the fabrication of composite and model samples and the experimental approaches of the micromechanical characterization methods utilized in this

thesis, e.g., nanoindentation and interfacial shear strength based on microcompression testing. The bases for the FEM simulations are introduced.

- Chapter 4 elucidate the effect of the composite structure on the epoxy phase. A novel approach to fabricate nanoporous polymer and circumvent the influence of the NPG structure is presented. A series of nanoindentation was carried out to evaluate the composite's morphology and structural length-scale effect on the NPP properties.
- Chapter 5 is dedicated to investigating the presence of an interphase and how the local mechanical response is altered near a gold-epoxy boundary. Composites and planar interfacial samples are analysed here by several techniques, e.g., chemical analysis, transmission electron microscopy (TEM) microscopy, nanoindentation.
- Chapter 6 focuses on the measurement of the interfacial strength between gold and epoxy. A technique is developed based on the microcompression of microcolumn with inclined interfaces, which allowed for the determination of microshear response. The interfacial property is separated from the microcolumn response, and it was used as the basis for the FEM interfacial modelling.
- Chapter 7 brings the finding from the previous chapters together to understand the overall mechanical properties of NPG-polymer composites. The composite's mechanical response was simulated using the FEM approach developed in the last chapter, which revealed the influence of the interfacial properties and allowed the comparison of the interfacial behaviour with experimental results. Furthermore, the strengthening of the Au phase is evaluated in terms of the dislocation activity within the ligament structure.
- Chapter 8 summarizes the findings of the work and provides brief suggestions on future works.

2 Background

This chapter introduces the mechanics of NPG-polymer composites. Here, each constituent phase is reviewed in terms of the size-dependent mechanical response, which is potentially activated due to the composite's small structural length-scale. The characteristics of a typical metal-polymer interface are introduced in perspective to the potential impact on the mechanics of composite materials and the particular case of NPG-epoxy composites. To this end, the stress conditions and the role of the bonding strength on the composite's properties are given to polymer reinforced composites.

2.1 Mechanics of NPG-polymer composites

Nanoporous gold (NPG) is a nanoscale porous material made of gold ligaments whose size can be adjusted to exploit strengthening at a sub-micron scale. [12]. The relatively easy tailoring of its structural length-scale makes the NPG an ideal model system for studying size-effects on the plasticity of nanostructures. Additionally, the high porosity allows for significant deformation under compression, which contrasts with other nanomaterials [13]. The densification of the ligament network imposed during the accommodation of strain leads to an apparent work hardening at the macroscopic scale, promoting stable and uniform plastic flow in compression [14, 15]. However, the opposite occurs under tensile loading, with deformation inducing a decrease in density of the NPG structures leading to work softening and a brittle failure [16–18].

Wang and co-workers presented an alternative to circumvent the tension-compression asymmetry of the NPG by infiltrating the open porosity with a polymer phase [15]. The polymer improved the stress distribution under tensile loading, which increased the ductility. However, adding a second phase created a more complex structure that motivated the investigation of the mechanical response of these novel materials. Figure 2.1 shows results from Wang's work [15]; it shows the stress-strain behaviour of millimetre-sized samples under compressive loading. The plot shows the response of NPG and NPG-epoxy composites at a variety of ligament sizes and bulk

epoxy samples. The inset presents an NPG sample before and after compression, which illustrates the absence of transverse plastic flow. Some important remarks were claimed from that study:

- The presence of a yielding point in the composite reflected the property of the polymeric phase,
- The strength of both NPG and the NPG-epoxy composite increased with the decrease of the ligament size,
- At any ligament size, the composite material was "much stronger" than each of its constituents' phases.

Furthermore, other studies addressed the overall mechanical properties of the NPG-polymer composites using macromechanical techniques [9, 19], micromechanical techniques [11], and simulations [20–22]. Nevertheless, the actual contribution considering the potential size-dependent response of the constituent phases and the interface remain unsolved.

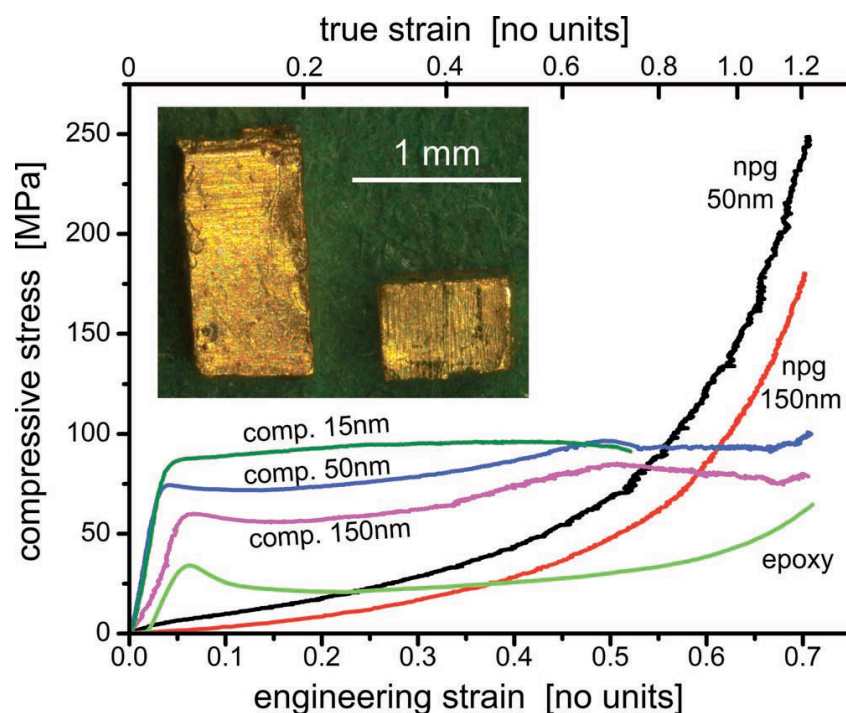


Figure 2.1: Stress-strain curves of millimetre-sized cuboid samples of NPG, NPG-epoxy composite and bulk epoxy. The inset presents the side view of an NPG sample before and after the compression to an engineering strain of 0.6, illustrating the absence of transverse plastic flow. This plot was taken from [15]

2.1.1 Size effect in NPG

A size effect in the plasticity of gold is well known, and it is commonly accepted that plastic deformation in small volumes requires higher stresses than in bulk samples. Some of the size-dependent behaviour are artefacts of the constraints of the surrounding regions of the analysed volumes, e.g. grain size hardening [23, 24] and confinement of dislocations within a thin film due to the presence of a substrate [25]. Although these extrinsic mechanisms have been vastly investigated, they can not explain the size effect from unconfined geometries [26]. Intrinsic size effects arise when single crystals are deformed in small, unconstrained volumes, usually explained by strain gradients, dislocation starvation effects and truncation hardening [26–28]. An example can be found in the size-dependent response of microcolumns' compression of single-crystal gold, caused by dislocation starvation hardening. In that case, the dislocations leave the crystal more quickly than they multiply, which requires continual dislocation nucleation during deformation [26, 27].

The nanoporous gold microstructure creates the conditions to activate the same size-dependent mechanisms from the compression of Au microcolumns but in a 3D structure. Not surprisingly, high strength has been reported for NPG with small ligament sizes [29, 30]. Figure 2.2 (a) shows a summary presented by Biener et al. [31] and extended by Mameka et al. [19], displaying experimental measurements on micro and nano-gold objects and nanoindentation of NPG. As can be observed by the local strength, σ_y^{loc} , the trend smaller is stronger is consistent on all the presented data. Biener et al. showed that the yield strength in very fine NPG, with average ligament size of 10 nm, reaches the theoretical shear stress for Au [32]. The plot in Figure 2.2 (b) shows the strengthening of samples with decreasing ligament size obtained by nanoindentation experiments, in perspective to the theoretical maximum yielding stress and the typical yield stress from bulk gold.

In NPG networks, the deformation is dominated by the bending of the ligaments that form the open-cell structure. More recently, Dou's modelling work showed that the deformation is mainly confined to the cell hinge, causing a lattice rotation which accounts for the influence of geometrically necessary dislocations to the NPG strengthening [33]. This hypothesis was later supported by TEM microscopy, showing the concentration of defects on the Au structure located in the nodes of NPG networks [1]. Additionally, TEM imaging has been used to reveal the dislocation activity in many micromechanical investigations, including micro dog-bone [34] and microcolumns [35].

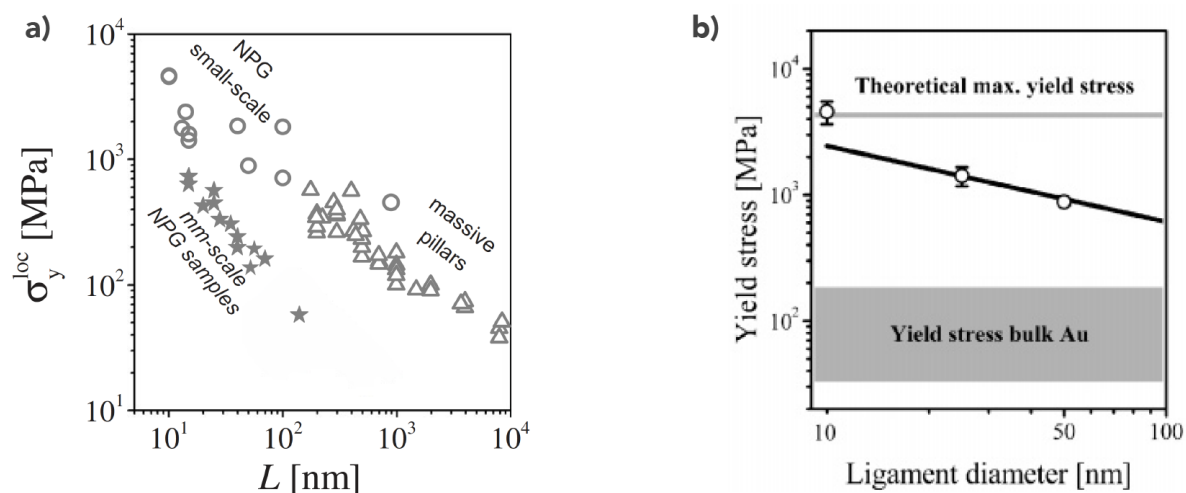


Figure 2.2: (a) Size-dependent strength in NPG showed by the local strength, σ_y^{loc} , versus the mean ligament diameter, L . The plot shows experimental data from compression of gold pillars (open triangles), mm-scale NPG samples (grey stars) and nanoindentation on NPG (open circles). Adapted from [12]. (b) Yield strength versus the ligament diameter of NPG with decreasing ligament sizes showing the reaching of the theoretical shear stress for Au. Adapted from [32].

2.1.2 Size effect in polymers

Although the mechanics of polymer materials are unique in terms of the viscoelastic response, whenever the boundary of the continuum mechanics is pushed, polymers may also present the trend "smaller is stronger". In the case of polymer materials, a size-dependent mechanical response has been experimentally observed in various polymers. Some examples are epoxy [36–42], polystyrene (PS) [43, 44], polypropylene (PP) [45], polycarbonate (PC) [43, 44], polymethyl methacrylate (PMMA) [43, 44, 46], polyimide (PI) [47], nylon (PA66) [47], polydimethylsiloxane (PDMS) [48–52], polystyrene acrylonitrile (SAN) [44] and polyvinyl chloride (PVC) [44]. Different hypotheses were proposed in the literature as an explanation for the observed size effects. Some examples of mechanisms are friction [52], higher-order displacement gradient models [36–40, 46, 53–55], changes in the material properties through the thickness (heterogeneity of the material) [43, 49] and surface effects [56, 57].

Furthermore, the complexity of the length scale-dependent deformation in polymers is complicated by the varied molecular structures of polymers and their rate and temperature sensitiveness. The polymer size-dependent deformation has been observed in various experiments, such as nanoindentation [36, 43] and microbeam bending [37, 45]. Nanoindentation experiments are commonly used to study size effects due to the relatively easy adjustment of the analysed volume by controlling the indentation depth. Shallow indentations probe small volumes on the sample's surface and reveal strengthening at smaller length-scales, typically referred to as an

indentation size effect (ISE). Figure 2.3 shows summary results presented by Han containing the hardness versus indentation depth data for various polymers [58]. As can be observed, the hardness response increases with decreasing indentation depth for all of the considered polymers. However, the magnitude of the ISE and the indentation depth at which the hardness response starts to increase differs significantly among the different polymers.

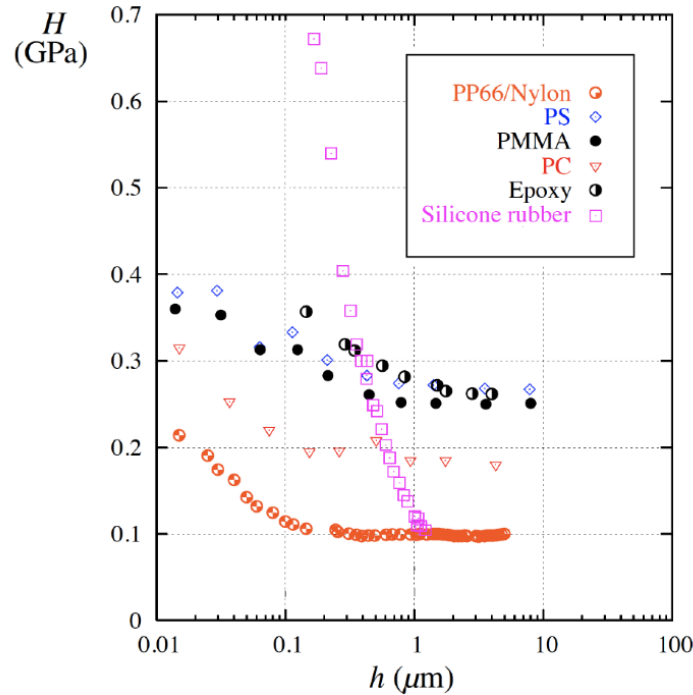


Figure 2.3: Size-dependent response in various polymers showed by hardness versus indentation depth. The plot displays the indentation size effect at shallow depths. Adapted from [58].

2.1.3 Metal-polymer interface

To understand the interaction in a metal-polymer interface, it is necessary first to define the physical boundary formed between the two materials. Polymeric interphase is typically formed in a polymer being cured against a solid substrate [59]. This transitional zone may differ from a sharp solid-solid boundary by displaying a gradient of properties due to the accommodation of the polymeric chains onto the rough metal surface [59, 60]. Additionally, the interfacial area definition is complicated by the potential fractal nature of a metal-polymer boundary. Even an apparent sharp surface at a macroscale is generally not smooth at smaller length-scales which directly affects the measurable contact area between the two phases. Thus, the interface as a 2D boundary varies in size according to the scale of the surface features, observation method, and the analysed length-scale.

The interaction in a metal-polymer interface combines mechanical interlocking and interfacial interaction [61]. Depending on the coupling materials, the interfacial interaction may lead to a weak physical interaction to a strong chemical reaction with the potential formation of an interlayer. Additionally, chemisorption of the polymeric chains at the vicinity of the interface can limit the motion of the chains. The end-groups attraction onto the metal substrate and the temperature might cause the polymer to adopt a three-dimensional conformation or a quasi-two-dimensional conformation [60]. The ordering at the proximity to the interface can even induce crystallization to amorphous polymers [62]. Nevertheless, these phenomena are limited to a couple of nanometres from the metal boundary. Interactions over tens of nanometres, reported on thin films, are explained only by weak van der Waals forces [63].

The presence of a metal surface may modify the polymeric mechanical response beyond the molecules in direct contact. The impact on the polymeric properties can be explained by the local chemical composition variation due to the adsorption of some chemical components. A classic example is the concentration of amines, which are often used as a hardness component in epoxy mixtures, and are prone to be absorbed by the metal surface affecting the local concentration [64–66]. Since the mechanical response of epoxy varies according to the amine concentration, the local mechanical properties at the vicinity of the interface can be affected. Palmese et al. have shown that the flexural modulus can be doubled by tuning the amine concentration on the epoxy resin [66].

In the case of gold-epoxy interfaces, Hu investigated interfacial failure via micromechanical analyses in NPG-epoxy composites [11]. The delamination of the interface was observed while uniaxially compressing microcolumns. The deformation led to lateral expansion localized at the microcolumn's top and bottom, which is consistent with a double-barrel deformation due to the friction with the indenter on top and constraints from the substrate on the bottom. Moreover, Hu used a focused ion beam (FIB) slice and view technique to create a 3D-reconstruction of the deformed microcolumn and identified interfacial delamination between the epoxy and the gold phase only in the strongly deformed regions. Figure 2.4 shows an adapted image taken from [11] showing a 3D reconstruction section of a strongly deformed region, in which the gold ligaments are shown in yellow, and the pores formed due to the delamination are shown in green. The delamination took place in highly curved regions and formed "horse-shoe" shaped delamination zones. Furthermore, the analysis of the angles normal to this delamination and the loading axis showed that the majority of the debonding is oriented perpendicularly to the loading, which points to a tension induced delamination mechanism.

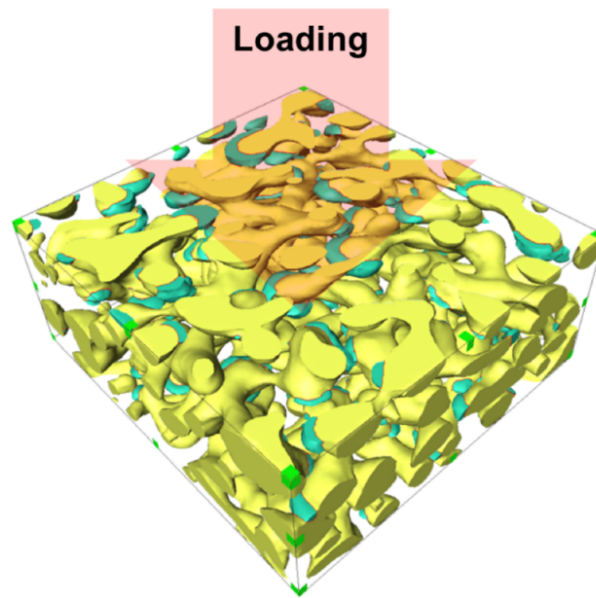


Figure 2.4: 3D reconstruction of a strongly deformed region after the compression of a microcolumn made of NPG-epoxy composite, showing the gold ligaments in yellow and the porous in green. The delamination formed "horse-shoe" shaped delamination. Adapted from [11].

2.2 Role of an interface in composite materials

The mechanical response of reinforced materials depends on three factors: properties of the reinforcement phase, properties of the matrix, and the effectiveness of the bond between the reinforcement and matrix in transferring stress across the interface. The first two factors are usually investigated by characterizing each phase separately, but the latter depends on the contact pair's structural complexity combined with the interaction between the constituent phases. The mechanics of load transfer at the interface is primarily a mechanical process and often considers a perfect bonded surface pair [67]. Nevertheless, processing conditions and the interaction between the constituent phases can lead to complex interfacial regions [68–71]. Here, a distinction is necessary between an interface and an interfacial region. While the former is the shared surface between the constituent phases with zero thickness, the latter is the volume affected by the phases' boundary. This section briefly reviews the interface's contribution to the composite structural integrity. The following aspects are discussed: stress conditions at the interfaces, intrinsic properties of an interface, and the effect of the bonding strength in the overall properties of composite materials.

Understanding the stress condition near the interface is crucial for predicting the mechanics of composites materials with very distinct constituent phases, e.g., the polymer reinforced composites. The interfacial region is prone to concentrated stresses because of the load applied to the structure, the mismatch in thermal expansion and shrinkage [67, 72]. Additionally, the interfaces can also modify the interfacial region, acting as a nucleation site, preferential adsorption site, and being a locus of chemical reactions [72].

In terms of examining the stress condition at the interface, the shear-lag model initially proposed by Cox and further developed by others is the most widely used model to describe the micromechanics of load transfer [73–75]. The model centres on the idea that tensile stresses are transferred from a matrix to the reinforcement phase through interfacial shear stresses. It assumes perfectly elastic phases, planar and perfectly bonded interfaces, and a regular arrangement between reinforcement and matrix [67, 74, 75]. In a short fibre embedded in a matrix, the model allows for relatively simple approximated solutions. Figure 2.5 (a) shows a schematic diagram representing a short fibre of length l_f embedded in a matrix subjected to a strain ϵ_m . The applied load leads to a differential displacement between fibre and matrix in the fibre direction. The fibre axial stress σ_f and shear stress τ_i at the interface can be estimated along the fibre length as represented in Figure 2.5 (b). As can be observed, the shear stress peaks at the fibre end then decay rapidly away from them. On the other hand, the axial stress is minimized near the fibre ends then increases to its average value in the middle of the fibre. The shear-lag model is known to be inaccurate whenever the fibres' end is not perfectly bonded to the matrix. In these cases, the short fibres' load-carrying capability is compromised and becomes reduced compared to a continuous fibre subjected to the same external loading. Nevertheless, this approach has provided a firm basis for understanding the loading conditions at the interface of many composites and determining their interfacial properties [76, 77].

A distinction should be made whenever an interlayer is present regarding the local mechanical response at the interfacial region. The local property assumes a distinct value from the other phases at an interlayer length, in contrast to a gradual transition in the absence of an interlayer [78–80]. However, the local mechanical property variation in the latter is an artefact of the border's constraints (border effect). The interface itself has surface properties, and the most relevant is the bonding strength [72, 77]. The bonding strength is the force that holds the surfaces together, and it is a direct result of the adhesion forces and the interfacial conditions. During the loading of composite materials, the load transfer occurs as long as the interface can withstand the stress levels at the interfacial region [67, 77]. However, the bond can only withstand loading until a limit, and then each phase is free to accommodate the strain separately. Although weak interfaces are explored as a toughness mechanism in the design of some composites [69, 71, 77, 81], the breaking of the interfacial bonds limits the load-bearing capability and often leads to the composite's failure.

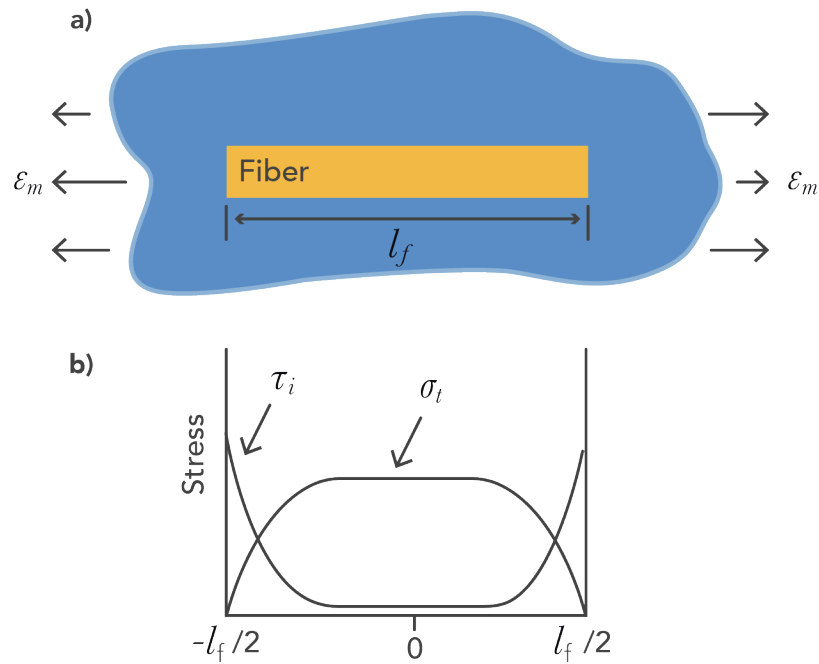


Figure 2.5: (a) Schematic showing the deformation around a single fibre embedded in a polymeric matrix under axial loading. (b) plot presenting the variation of the axial stress σ_f and interfacial shear stress τ_i according to the fibre's length. Adapted from [77]

The interfacial strength can be experimentally evaluated by a series of mechanical tests such as a pull-out test [82, 83], fragmentation test [84, 85] or transverse tensile test [86, 87]. Nevertheless, the interpretation of the strength measured by these methods is limited since the interfacial strength may vary according to the loading direction. Therefore, the maximum stress which an interface can withstand is often described for a specific loading direction. An alpha-factor describes the ratio between the interfacial strength for under tension and shear as follow:

$$\alpha_{int} = \frac{Y_s}{Y_n} \quad (4.1)$$

where Y_s and Y_n are the interfacial strengths on the shear and normal direction, respectively. The α_{int} value was studied using the cruciform specimen method, which typically revealed values greater than one [88–93]. Moreover, the higher strength in the shear direction was investigated, and it was attributed to frictional resistance, which occurs whenever the phases slide over each other [89].

The interfacial property can impact the overall mechanical response of composites. As an example, a series of studies have investigated the influence of the interfacial bonding on the overall stiffness and strength of polymer reinforced composites. In the case of stiffness, the degree of adhesion plays no effect on the observed elastic stiffness [72, 94–96]. The composites display their maximum stiffness whenever there is full contact between the phases, reinforcing the importance

of processing conditions to avoid defects in the interfacial region [72]. On the other hand, the strength and ultimate strain can be tailored by controlling the interface property. An example of this principle can be found in Kenyon's work [95], in which coupling and debonding agents were used in a glass bead-filled epoxy to demonstrate the effect of the bonding strengths. Figure 2.6 shows a stress-strain curve adapted from Kenyon's work for a glass-bead filled epoxy with the same volume fraction but different interfacial treatments. As can be observed, all treatments initially show the same stiffness, and the strength increases whenever the bonding is enhanced.

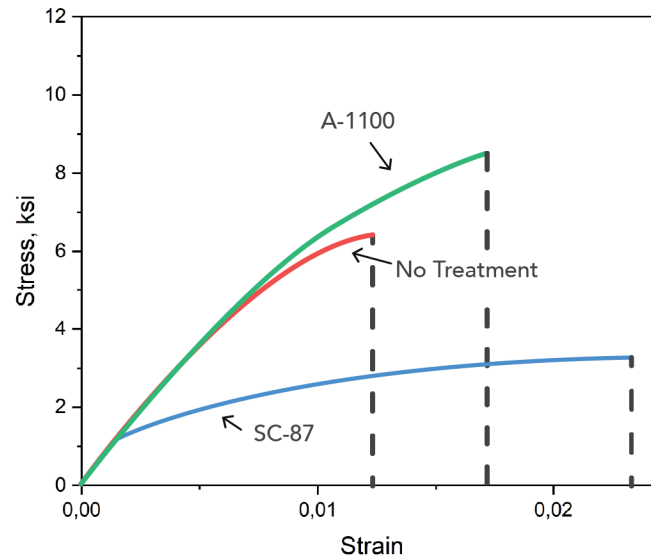


Figure 2.6: – Stress-strain behaviour of glass bead-epoxy composites, showing the influence of the interfacial strength on the overall response of the composite materials. The three curves represent surface treatments that modified the interfacial strength: A-1100 (coupling agent), no treatment and SC-87 (debonding agent). Adapted from [95].

3 Methods

This chapter introduces the fabrication methods for the samples experimentally investigated in this work: NPG, NPG-epoxy composite, and model samples containing planar interfaces between gold and epoxy. The nanoporous polymer (NPP) processing is also introduced utilizing two potential gold etching approaches: pure Hg and iodine-iodide solution. The characterization procedures employed in this thesis are also presented, focusing on microstructural characterization, chemical analysis, and micromechanical testing. Lastly, the basis for the FEM simulation utilized on the interfacial modelling is presented, showing the boundary conditions and constituent laws.

3.1 Sample preparation

3.1.1 Nanoporous gold

The NPG samples used in this work followed the processing route established by Wang, in which mm-sized samples were fabricated by electrochemical dealloying [97, 98]. First, $\text{Au}_{25}\text{Ag}_{75}$ ingots were produced by arc melting Au (99.995%, ChemPur, Germany) and Ag (99.99%, ChemPur, Germany), followed by homogenization by annealing at 850 °C. The ingot wire was cut in mm-sized samples, and the surfaces were polished to allow micromechanical experiments.

The dealloying took place in a three-electrode electrochemical cell with a luggin capillary controlled by a potentiostat. Details on the solutions, electrodes, and processing parameters can be found in the detailed protocol developed by Wang [97, 98]. After the dealloying, the NPG samples were washed in ultra-purified water and dried in vacuum. The as-dealloyed NPG structure is very fine, with a mean ligament size around 20 nm. Coarsening of the Au-ligaments by annealing in an IRF 10 infrared furnace (Behr, Germany) was conducted following the parameter established by Hu [11].

3.1.2 NPG-polymer composite

The processing route of the NPG-polymer composites used in this work is summarized in Figure 3.1. The NPG structures were impregnated with an epoxy resin, made by mixing Bisphenol F epoxy resin (BER 20, Buehler, Germany) and amine hardener (BEH 20, Buehler, Germany). The polymer impregnation took place in a commercial vacuum impregnation unit (CitoVaca, Struers, Germany) to avoid bubbles. After the cure of polymeric resin, the samples were cut using a diamond wire saw to fit them on a standard SEM sample stub. Finally, the surfaces to be analysed were mechanically polished. Then, the samples were mounted in SEM stubs using a silver paste, which also was applied on the side surfaces of the samples to avoid charging during electron imaging. Figure 3.2 shows a SEM micrograph of the surfaces of a NPG sample (a) and a composite (b).

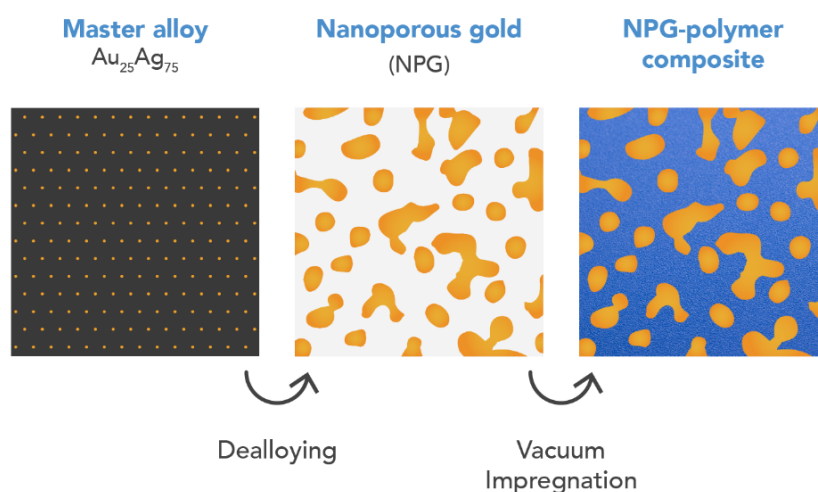


Figure 3.1: Main steps on the processing route of the NPG-epoxy composites used in this work. This image was partially published in [99]

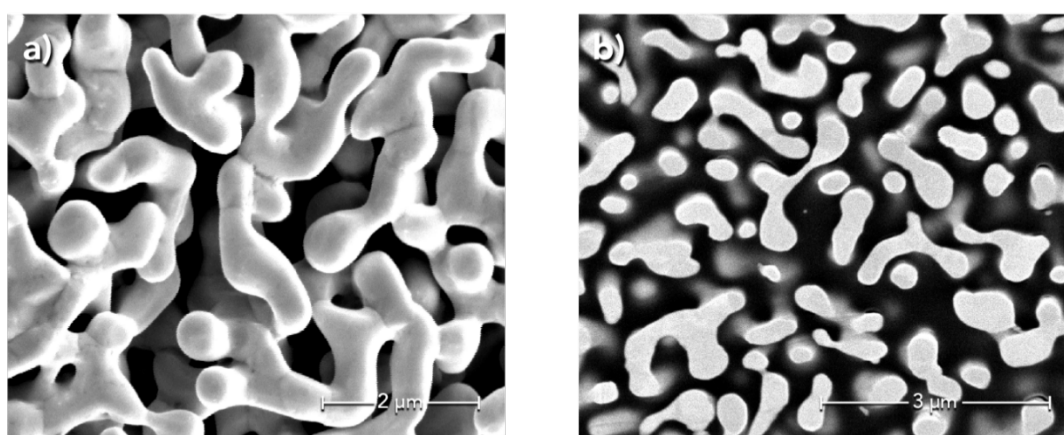


Figure 3.2: SEM micrographs of a mechanically polished surface of a NPG sample (a) and a polymer infiltrated NPG structure (b). The gold ligaments are shown bright and epoxy in grey.

3.1.3 Planar interface samples

The processing route of the model samples with planar interfaces used in this work is summarized in Figure 3.3. First, a laminated piece of bulk gold (99,99% purity, MaTeK, Germany) was cut in fillets with approximate dimensions of 0.25 x 5 x 25 mm. The fillets were annealed at 850 °C for 12 hours to obtain a large grain structure. Then, a metal wire structure was bent to hold the gold fillet at a specific inclination angle to the ground. Superglue was applied on the fillet base in contact with the ground. After the glue was cured, the metal wire structure could be removed. Finally, the gold was impregnated using the same procedure and epoxy resin as the NPG-epoxy composites fabrication. Cutting, polishing and mounting followed the processing developed for the composite's fabrication.

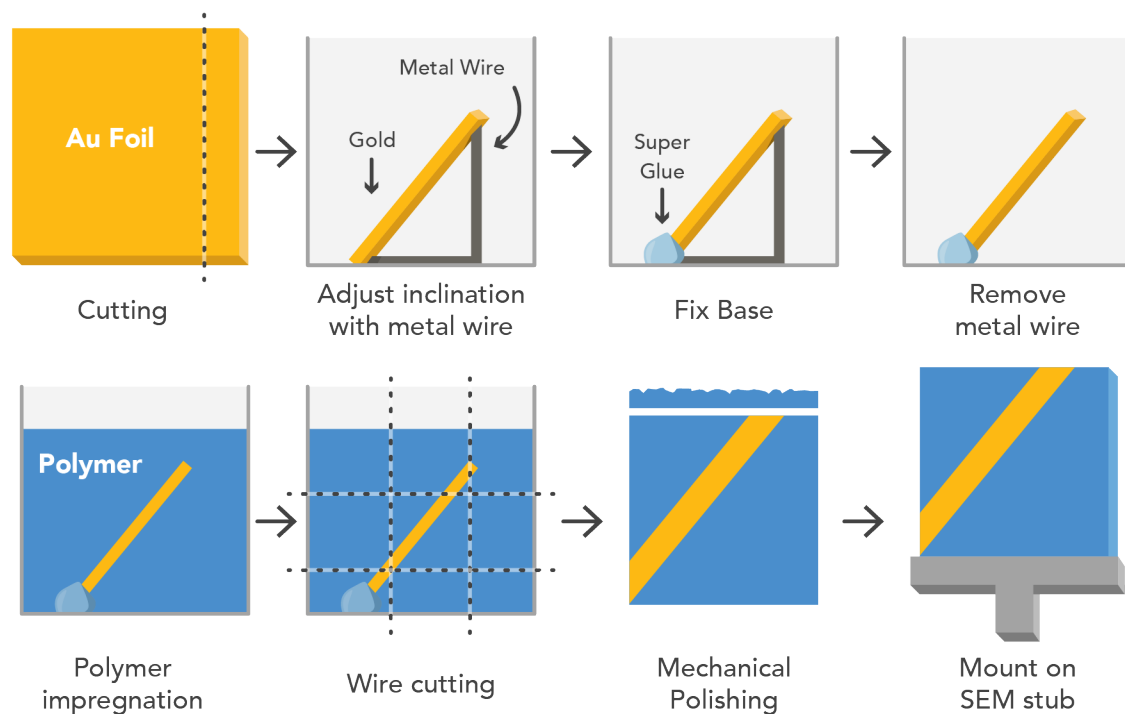


Figure 3.3: Processing route of planar interface samples developed in this work. The laminated piece of bulk gold was mounted at a specific angle for the polymeric vacuum impregnation. The sample was then cut, mounted and polished allowing for micromechanical experimentation.

The planar interface investigated in this work took inspiration from the morphology and geometry of the NPG-epoxy composite interfaces. Figure 3.4 (a) presents a SEM image showing a cross-section in the composite in which it is possible to observe the geometries at the boundary between the gold ligaments and the epoxy phase. Whenever a cross-section cuts a ligament, the interface under the upper surface would rarely be perpendicular; more likely, the morphology of the ligaments would result in an angle to the upper surface. The inset in Figure 3.4 (a) illustrates this idea for a single ligament. Measurements performed directly on the composite structures are

complicated due to complexity and the small length-scale of the ligament structure. Therefore, a planar interface with a 45° inclination was used in this work to allow for a systematic investigation. Figure 3.4 (b) shows a SEM micrograph of the planar interface used here. Later on, FIB was used to mill a cross-section perpendicular to the surface at the boundary between gold and epoxy phases, and SEM imaging was utilized to measure the angle between the phases.

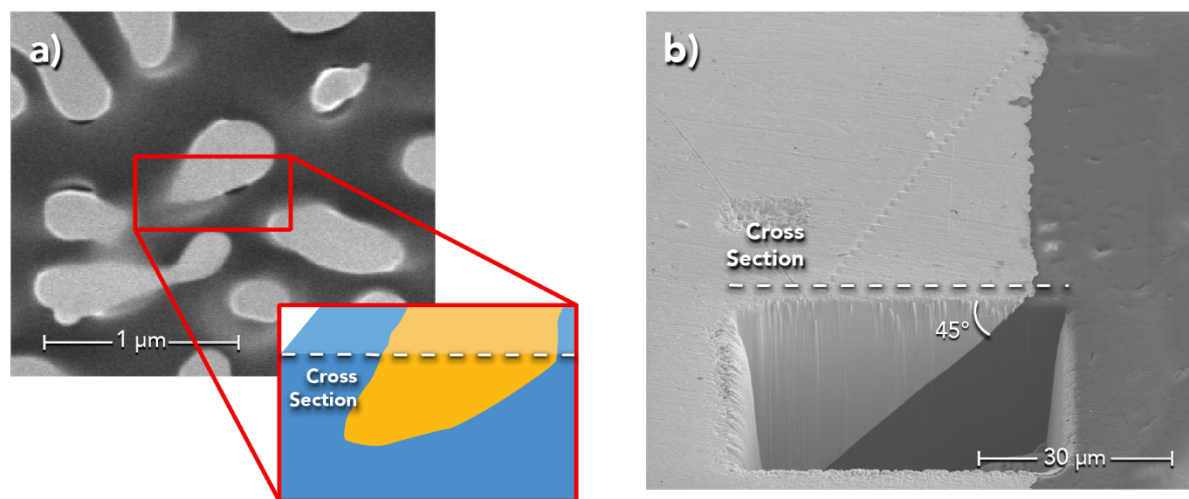


Figure 3.4: (a) SEM image showing the interface geometry in a NPG-epoxy composite. The inset illustrates the inclination to the upper surface whenever a cross-section cut a ligament. (b) SEM image of a mechanically polished surface of a planar interface with an inclination of 45° from the sample's upper surface. The FIB milled cross-sections were performed perpendicular to the surface to confirm the angle between the phases. Gold appears in bright colour in both pictures, while the epoxy is shown in grey.

3.1.4 Nanoporous polymer

In this work, inspiration from the extraction metallurgy of gold was taken to leach out the Au phase from the NPG-epoxy composites. This approach allowed to investigate the uncoupled mechanical properties and potential size effects in the polymeric phase of such nanostructured composites. A novel processing route was developed in this study to fabricate bicontinuous nanoporous polymer (NPP) structures that maintain the exact morphology and length-scale of the polymer phase in the NPG-polymer composites. The etching methods evaluated and the details of the developed processing route are described in this section.

Gold etching

Gold etching is a fundamental process in the fabrication of many microscale devices employed in advanced technologies. Semiconductors, optoelectronic, and microsystems are examples of industries where the controlled leaching of gold is necessary [100, 101]. Additionally, gold etching technologies are crucial in mining operations [102–104]. Therefore, processes that follow the same principles are used to extract gold from ores and fabricate microchips. As the majority of mining techniques, thin-film patterning is traditionally performed by wet etching [100, 105, 106]. This approach consists of direct contact between the gold and liquid solution, in which the etching solutions contain two essential components: complexing ligand and oxidant agent. The former is responsible for forming stable Au(I) complexes. Some of the suitable ligands are cyanide, chloride, iodide, and bromide. The latter adjusts the surfaces' potential at a value where significant gold dissolution can occur [100].

In the case of technology to remove the Au from NPG polymer composites, a wet system would have the advantage of filling cavities and establishing contact with the Au within the ligament structure. For this reason, a wet etching technology was selected in this work. Similar to a wet etching process, a technology based on liquid mercury can be used to leach out gold from the ores. Although mercury is extremely harmful to many living organisms, this method is still often used in small gold mining operations in sub-developed countries [107, 108]. The pure liquid mercury is poured over the granulated ores, forming an amalgam phase. As shown in the phase diagram in Figure 3.5, a series of Au-Ag intermetallic components are formed at room temperature [109, 110].

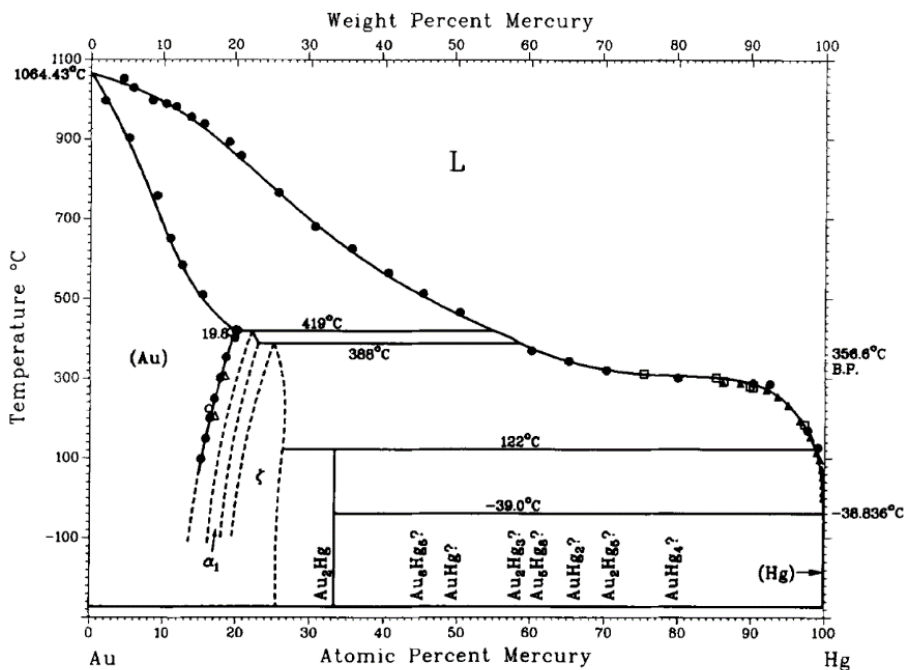


Figure 3.5: Phase Diagram for an Au-Hg System. Adapted from [110].

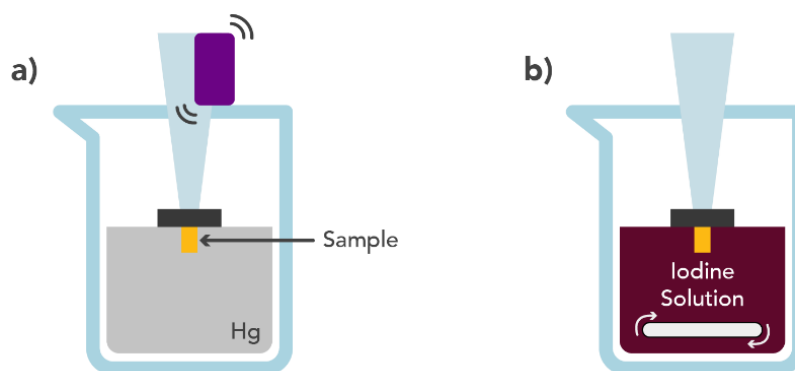
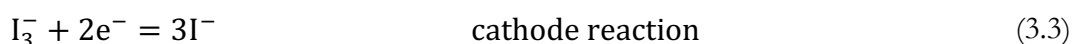
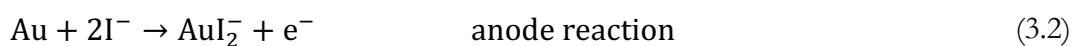


Figure 3.6: Schematic showing the experimental setup for the etching processes of NPG-epoxy composites. In the Hg approach (a), agitation was applied by a vibrating device attached to the pipette, while in the iodine-iodide approach (b), the solution was stirred.

In this study, the solubility of gold in liquid mercury was explored. Since Hg is liquid at room temperature, the NPG-composite samples could be submerged, forcing contact with the Au ligaments, as shown in the schematic of Figure 3.6 (a). The composites samples with approximate dimensions of 1 x 1 x 2 mm were mounted in a SEM stub and placed on a pipette tip. Gold solubility in mercury is 0.13 at. % at 25 °C, so 1 g of solid gold could be dissolved in approximately 8 g of liquid mercury. A sufficient amount of mercury (99.999% purity, MaTeck, Germany) was poured into Becker, where the sample was submerged. A vibrating device attached to the end of the pipette applied a continuous agitation. The samples were submerged for 40 hours, and the samples' surface was then observed using SEM imaging.

A second approach based on a wet etching technology was developed using an iodine-iodide solution, a solution frequently used in leaching Au because iodine forms the most stable complexes in aqueous solutions with gold [111]. This process initiates when iodine reacts with iodide ions forming triiodide, which then acts as an oxidant for the gold leaching according to the following electrochemical reaction [100, 112]:



The setup used for this procedure was similar to the one used in the Hg approach. However, a stirring agitation was implemented during the submerged period, as represented in Figure 3.6 (b). After the treatment in the iodine-iodide solution, the samples were washed in deionized water and dried in air. Figure 3.7 schematically shows the processing route of the epoxy-infiltrated NPG composites and the subsequent step to produce NPP.

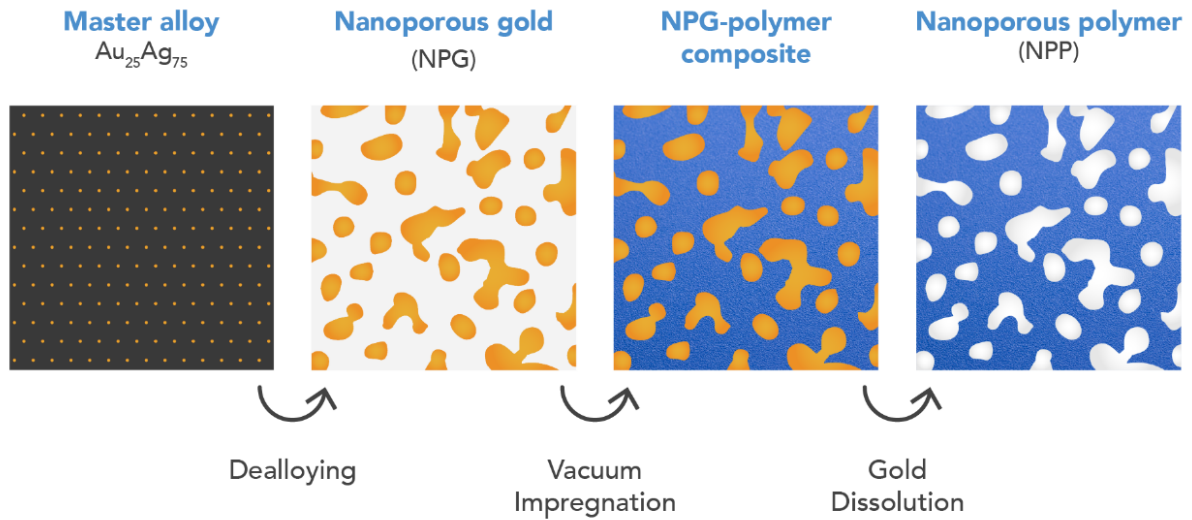


Figure 3.7: Schematic on the main steps of the fabrication of nanoporous polymer (NPP) developed in this work. This image was already published in [99]

3.2 Microstructural characterization

3.2.1 FIB-SEM dual system beam

A Nova Nanolab 200 dual beam system (FEI, USA) equipped with in-situ platinum (Pt) injection system and an Omniprobe micromanipulator was used in this work for sample imaging, preparing lamellas for transmission electron microscopy (TEM) and fabricating microcolumns for micromechanical experiments. A typical Focused Ion Beam (FIB) - Scanning Electron Microscope (SEM) dual-beam system combines a vertical electron beam column and a tilted focused ion beam column in a single platform, as shown schematically in Figure 3.8. The former provides a beam of focused electrons accelerated and then used to scan over the sample surface, creating an image. Similarly, the latter provides a beam of ions, usually Ga^+ , that can be focused on extremely small spot size, usually on the order of 5-20 nm [113–115].

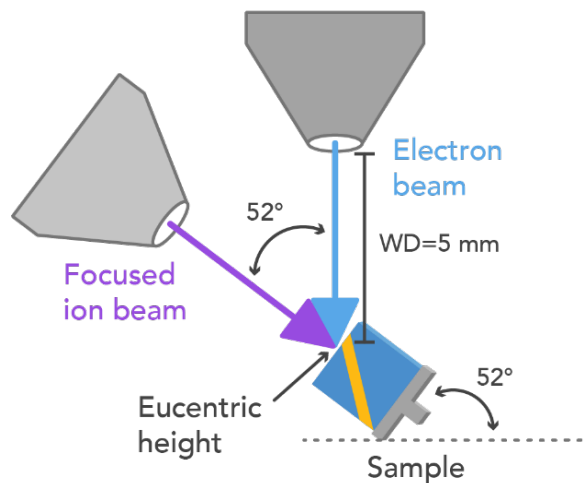


Figure 3.8: Schematic illustrating a FIB-SEM dual beam system with a sample in the standard milling position. The electron beam and the focused ion beam cross at the same point of the sample surface whenever the sample is at the eucentric height. This specific work distance (WD) is 5 mm for the employed equipment.

Ligament size measurement

An imaging processing technique based on BoneJ plugin for the Fiji software package was utilized to measure the size of the structures analysed in this work. BoneJ uses the largest sphere analysis to assess the dimensions of binary pictures, which provides a systematic method to evaluate the ligament size of NPG samples and the corresponded porous size. First, SEM imaging is used to capture the ligament structure on the surface of the sample. Then the image is converted to a binary form, and later BoneJ is run to apply the largest sphere analysis [116]. Each one of these steps is shown in Figure 3.9 using, as an example, a NPG structure with a mean ligament size of 550 nm.

In the case of the NPP samples, the ligament size was measured in cross-sections fabricated on the edge of the samples perpendicular to the upper surfaces to avoid any surface effect originated by etching treatment. Therefore, the main steps of the fabrication process of the cross-section are the following:

- a) Coarse cross-section milling of rectangular shape on the edge of the sample perpendicular to the upper surface, as shown in Figure 3.10 (a). The typical dimension of the milling pattern was $20\ \mu\text{m} \times 20\ \mu\text{m} \times 20\ \mu\text{m}$ using a 5 nA current.
- b) Fine cleaning cross-section milling carried out to remove the rough surfaces produced by the coarse milling step using a 0.3 nA current.
- c) The sample is then re-mounted to ensure that the SEM beam would image the milled cross-section perpendicularly, as shown in Figure 3.10 (b).
- d) Further image processing followed the same steps as the process done for the NPG samples.

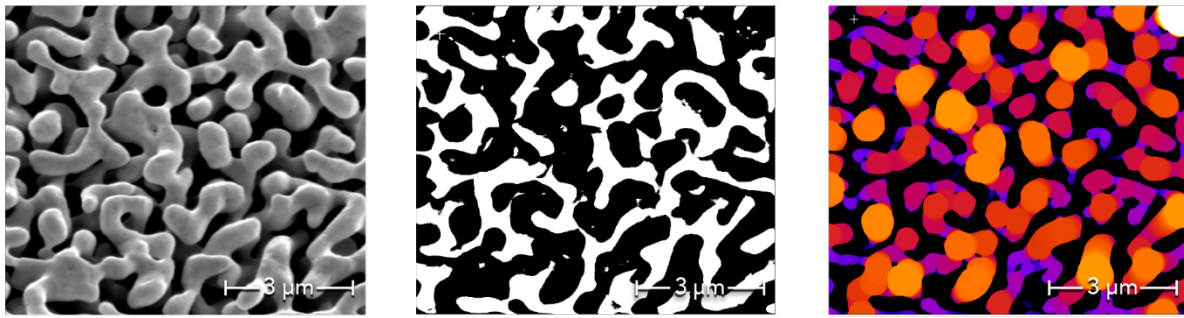


Figure 3.9: Evolution of the images used during the measurement of the ligament size of NPG structures. The initial micrograph of the NPG structure is binarized using Fiji software, then BoneJ plugin carries out the largest sphere analysis.

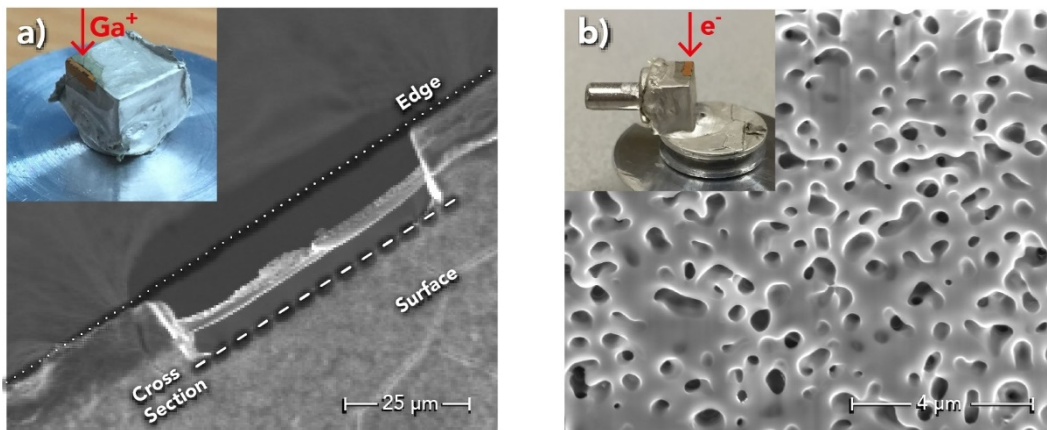


Figure 3.10: SEM micrographs showing the upper surface in which the cross-section was milled on the edge of a NPP sample in (a) and the cross-section itself in (b). The insets present the sample setup oriented to the beam direction for milling and imaging the cross-section.

3.2.2 TEM

A CM200 Transmission Electron Microscope (Philips, Germany) operated at 200 kV, and a Titan 80-300 Transmission Electron Microscope (FEI, USA) operated at 300 kV were used in this work. The former was used to investigate the interfacial region between gold and epoxy in NPG-epoxy composites, while the latter was used to examine the dislocation activity in deformed NPG structures. Similar to a SEM, TEM systems are used to obtain magnified images of samples. However, an electron beam is accelerated to transmit through a sample, allowing for higher magnification but limiting the sample thickness [117–119]. A TEM operation is well described in the literature; it consists of generating an electron beam and controlling it with apertures and magnetic lenses. After transmitting through the sample, detectors capture the signals, forming an image [119].

High-resolution TEM (HRTEM) can be used to obtain higher magnifications, which is often useful for visualising samples' crystallinity in real space. The analysed sample must be oriented along a zone axis to observe the crystal lattice from the lattice fringe spacing. The images in HRTEM reproduce the periodicity of a crystal structure but do not necessarily represent the atomic position. Even at lattice resolution, their interpretation needs to take in considerable variation in the sample thickness, as the aberrations in the objective lens, defocus, and astigmatism [119–122]

Lamella preparation

In this work, all the lamellae investigated in the TEM were fabricated by FIB milling. Although the method for fabricating thin lamella can be found in the literature [123, 124], NPG lamella preparation is particularly challenging. First, gold is a dense material, which increased the necessity for a thinner lamella. Whenever the NPG ligament size was bigger than the lamella's predetermined thickness (below 100 nm), the porosity of the NPG compromised the structural integrity of the lamella. Some of the samples investigated in this work were fabricated from NPG with 400 nm of mean ligament size. For these cases, the lamellae's structural integrity was only possible because the NPG structure was previously impregnated with epoxy.

A second approach developed to obtain electron transparency samples consisted of using very fine NPG structures, which mean ligament sizes of 20 and 50 nm. This approach avoids the necessity of polymer impregnation. However, the thinning down of the lamellae was still limited due to a severe bending observed in thickness below 100 nm. It was observed that no matter the ligament size, the electron transparency was compromised whenever two ligaments overlapped. Thus, the imaging of these samples was limited to regions with a single ligament thick.

These fine NPG structures were used to investigate the dislocation activity within the ligament structure. The surface was indented using a 15 μm diameter flat punch that reached 1 μm deep to promote plasticity in the analysed regions. The main steps of the fabrication process are the following:

- a) Deposition of an 800 nm thick Pt layer over the flat punch indentation or area of interest to minimise ion damaging.
- b) Coarse cross-section milling of two trenches on both sides of the deposited Pt. The trench's typical dimension was 40 μm x 30 μm x 30 μm using a 3 nA current.
- c) Fine cleaning cross-section milling carried out to remove the rough surfaces produced by the coarse milling step using a 0.5 nA current.
- d) The lamella is then tilted to an angle of 7 degrees and partially cut-free from its base and sides using a current of 0.5 nA. The lamella is afterwards attached to the Omniprobe with a thin layer of Pt.

- e) After cutting it free from the trench, the lamella is lifted out and attached to a finger of a TEM Cu grid. Then, the lamella is further thinned down, using a current of 0.3 nA.
- f) A final step to remove the ion-damaged surface layer on the lamella is done at a glancing angle using low voltage and current, 5 kV and 70 pA, respectively.

Two lamellae ready for TEM investigation are shown in Figure 3.11. They represent the two strategies of the lamellae used in this investigation: (a) coarse NPG impregnated with epoxy and (b) fine NPG structure. An area of a single ligament thick is shown for the fine NPG structure in (c). The lamella thickness, measured by SEM, was kept below 100 nm for all lamellae investigated in this work.

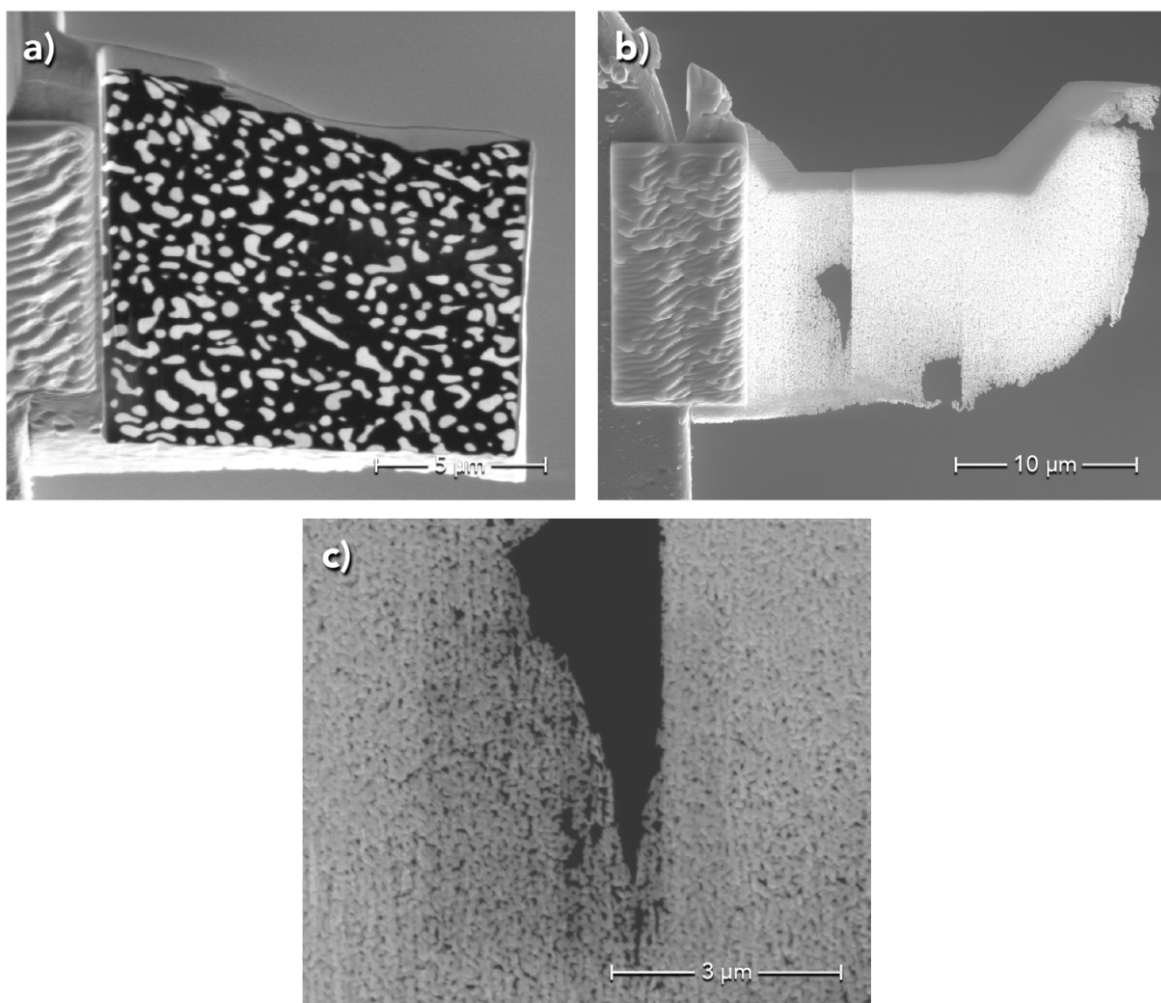


Figure 3.11: SEM images of the FIB milled lamellae used in the works. (a) and (b) show a lamella made from a coarse NPG-epoxy composite and a fine NPG structure, respectively. (c) shows a region at higher magnification in the NPG where the ligaments do not overlap. This image exemplifies the regions used for high-resolution TEM imaging.

3.3 Chemical analysis utilizing energy-dispersive x-ray spectroscopy

Chemical analyses were conducted in this work using an in-situ EDAX spectrometer attachment to the SEM at a voltage of 15 kV. This technique allowed for the elemental microanalysis of controlled regions of the samples, which was explored to determine the efficiency of the gold removal during the processing of nanoporous polymer structures. Additionally, a mapping feature enabled the observation of the element distribution at the interfacial regions between gold and epoxy planar interface samples, which correlated SEM observation with the local element composition. In both cases, the specified voltage was selected to identify the presence of gold [125].

The energy-dispersive x-ray spectroscopy (EDS) system relies on the same incident electron beam produced by the SEM to generate characteristic X-rays in the specimen's atoms. This signal is originated from the elastic scattering from the impact of the electrons on the sample. After the impact, the atoms are ionized, and during the return to their ground state, characteristic X-rays is emitted. A photon-energy sensitive detector then captures the X-ray emission. Finally, the characteristic energy contains the information necessary to identify the elements present in the specimen [126–129]

3.4 Micromechanical behaviour characterization

3.4.1 Nanoindentation

A Nanoindenter XP (MTS Corp., USA) was used in this work to mechanic characterize nanoporous gold and nanoporous polymer samples. Additionally, a series of indentations in line crossing a planar interface was carried out to measure the transitional properties between gold and epoxy. Nanoindentation measurements are commonly used to characterize materials in small volumes with a spatial resolution at a sub-micron scale [130–132]. A typical experiment consists of penetrating an indenter into a surface while the load is continuously measured as a function of the indentation depth until the withdrawal from the material. Figure 3.12 (a) shows a schematic representation of a load, P , versus displacement, h , for a typical nanoindentation experiment.

The indenter's geometry plays an essential role in the stress distribution during the contact with the surface, and it needs to be well defined to allow for the calculation of the contact area

[133–135]. Different indenter types can be used, such as spherical, Knoop, Vickers, cube corner, flat punch, and Berkovich indenters. Many studies rely on the Berkovich indenter because they are manufactured easier to sharper, contributing to more precise control over the indentation process [136]. Nevertheless, flat punch geometry produces a well-defined stress field under the indenter and ensures a constant contact area throughout the test [137, 138]

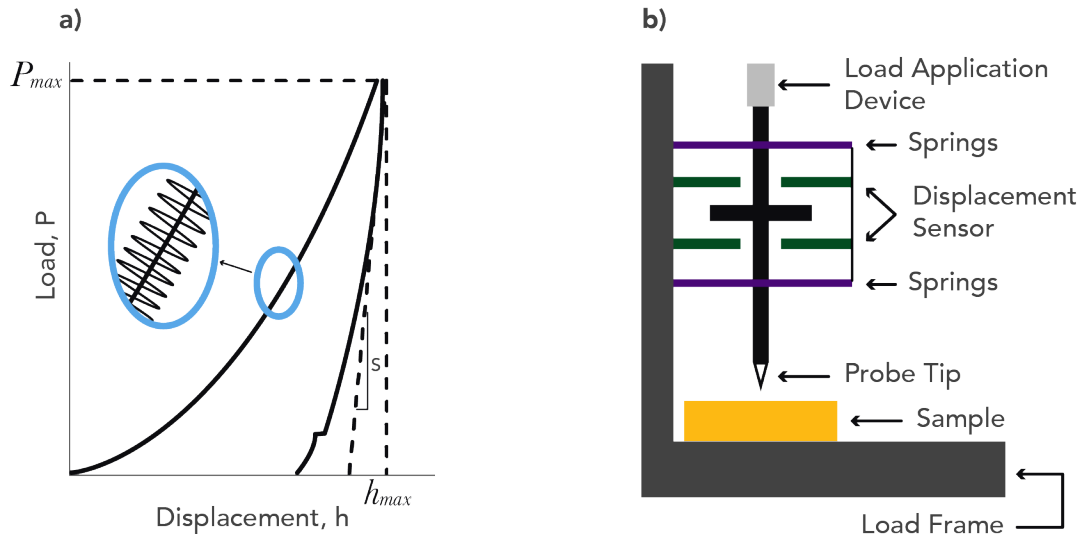


Figure 3.12: (a) Schematic representation of a typical nanoindentation experiment showing a load-displacement curve. Small dynamic oscillation and unloading cycles are applied during the loading portion, characteristic of continuous stiffness measurement (CSM) mode. S , P_{max} and h_{max} are the initial unloading stiffness, the peak load and maximum displacement, respectively. (b) Schematic illustration of a typical nanoindenter apparatus.

Figure 3.12 (b) shows a schematic representation of the setup used in this work. The load that drives the indenter tip into the sample's surface is applied using an electromagnetic actuator, while the capacitive sensor is used to measure the displacement [131]. The load and displacement resolution of the instrument used in this work are 50 nN and 0.01 nm, respectively. Additionally, the characteristic string constant, K_s , is 91 N/m. In terms of analysing the data from nanoindentation tests, the Oliver-Pharr [139] method is frequently used to calculate the hardness and the elastic modulus from a measurement. It assumes that a material deforms elastically and plastically during loading, but only elastic deformation is recovered during the unloading. Therefore, the elastic contact stiffness, S , can be estimated from the initial slope of the unloading segment, and it is related to the projected contact area of the indenter, A , by:

$$S = \left(\frac{dP}{dh} \right) = 2E_r \beta \sqrt{\frac{A}{\pi}} \quad (3.5)$$

where β is a constant that depends on the geometry of the indenter and E_r is the reduced elastic modulus which can be used to determine the elastic modulus of the materials, E , by offsetting the deformation of the indenter according to:

$$\frac{1}{E_r} = \frac{1 - \nu^2}{E} + \frac{1 - \nu_i^2}{E_i} \quad (3.6)$$

where E_i is the elastic modulus of the indenter and ν and ν_i represent the Poisson's ratio of the investigated materials and indenter, respectively. Additionally, the hardness, H , of a material can be determined in terms of the maximum load, P_{max} , by:

$$H = \frac{P_{max}}{A} \quad (3.7)$$

The accuracy of the measurement of both properties strongly depends on the precision of the inputted contact area. Generally, sink-in occurs on the rim of the indentation, as represented schematically in Figure 3.13. Therefore, the area function given by the indenter's geometry needs to be corrected based on the maximum displacement, h_{max} , and displacement of the surface, h_s . Finally, the contact depth of the indenter, h , can be calculated by:

$$h = h_{max} - \epsilon \frac{P_{max}}{S} \quad (3.8)$$

The constant ϵ depends on the indenter geometry, and it is equal to 0.75 and 1 for Berkovich and flat punch indenters, respectively.

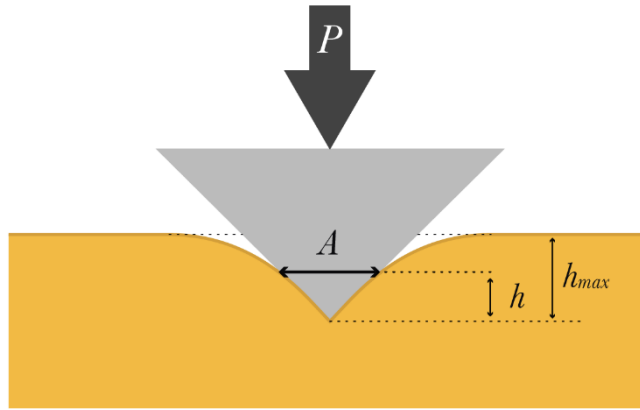


Figure 3.13: Schematic showing a lateral view from an elastoplastic material under the influence of a conical indenter. The image shows the load (P), the contact area of the indenter (A), the maximum measured displacement (h_{max}), and contact depth of the indenter (h).

In this work, the indentations followed a "continuous stiffness measurement" (CSM) approach. This method allows for the determination of the mechanical properties as a function of the indent depth by measuring the stiffness continuously during the loading segment. Thus, CSM implies that a small dynamic oscillation with a high frequency over the force signal is imposed, and

the corresponding displacement signal is measured continuously as a function of the indentation depth with a frequency-specific amplifier [139, 140]. The amplitude of the force oscillation represented schematically in Figure 3.12 (a) needs to be sufficiently small to avoid additional influence on the deformation process.

Although the elastic modulus is often used to describe the elastic property of materials, a more elaborated analysis is required whenever viscoelasticity comes to play. Polymer materials present the ability to both store and damp energy. In the case of dynamic loading, a phase shift between loading and displacement occurs. The complex modulus, E^* , is a phase vector, which combines both responses of the polymer materials:

$$E^* = E' + iE'' \quad (3.9)$$

where E' is the storage modulus, which quantifies the ability to store energy elastically and E'' is the loss modulus which quantifies the ability to damp out energy. The storage modulus can be equal to the elastic modulus for materials with insignificant damping [141, 142].

The complex modulus can be measured using a dynamic mechanical analysis in indentation testing [141, 143]. After the indenter establishes contact with the surface, a compression oscillation is applied, then and the response of the material can be used to determine the amount of energy stored and damped. Similar to an elastic solution, the storage modulus of a polymer is given by:

$$E' = \frac{S}{2\beta} \sqrt{\frac{\pi}{A}} \quad (3.10)$$

where β is a constant depending on the indenter geometry and A is the contact area. On the other hand, the loss modulus can be determined using the damping coefficient, D_s , and the harmonic frequency, ω .

$$E'' = \frac{\omega D_s}{2\beta} \sqrt{\frac{\pi}{A}} \quad (3.11)$$

In the investigations on the NPG structures and planar interface samples, the properties were obtained using a CSM system equipped with a Berkovich indenter. The indentations were carried out to a prescribed maximum indentation depth varying from 0.1 to 3 μm using an indentation strain rate of 0.05/s and a displacement oscillation amplitude of 2 nm. In the investigation of NPP structures, a series of nanoindentations were carried out to clarify the role of the microstructural length-scale on their mechanics. First, the storage modulus was obtained using a CSM system with a 15 μm diameter flat punch indenter. The indentations were carried out at a strain rate of 0.02/s down to 3 μm , then an oscillation amplitude of 50 nm was applied over a frequency range of 1 to 45 Hz. A second set of nanoindentations was conducted using a Berkovich indenter tip to evaluate the hardness of the NPP structures. Here, indentation to a prescribed maximum indentation depth of 5 μm was carried out using an indentation strain rate of 0.05/s and a displacement oscillation amplitude of 2 nm.

Flat punch indentations were also carried out to measure the elastic modulus of the samples. For these cases, Sneddon's equation was used as an alternative to circumvent the sink-in effect while considering a cylindrical punch indenting an elastic half-space [144]. The analytical expression to calculate the compliance of the half-space materials, $C_{sneddon}$, associated with the deformation is given by:

$$C_{sneddon} = \frac{(1 - \nu^2)\sqrt{\pi}}{2E\sqrt{A}} \quad (3.12)$$

Therefore, the relation between the elastic contact stiffness and the elastic modulus is given by:

$$E = \frac{S}{D_p} (1 - \nu^2) \quad (3.13)$$

where D_p is the flat punch diameter, and S can be obtained from the initial unloading segment.

3.4.2 Microcompression

Microcompression technique is a micromechanical characterization method capable of measuring the stress-strain behaviour at a micrometre and sub-micrometre scale. It consists of compressing a microcolumn with a defined cross-section area with a flat-punch indenter in a nanoindentation instrument. Since it was first reported by Uchic [145, 146], it has been vastly utilized to characterize various materials such as metals [147] and polymer [148]. The schematic of a typical microcompression testing is shown in Figure 3.14, in which the initial height, H_0 , and diameter, D , are represented for a microcolumn. The relatively simple geometry results in a uniform and uniaxial stress state, which typically results in a nominally constant deformation of the microcolumns. Therefore, the analysis of microcompression is relatively straight forward, especially when compared with nanoindentation testing.

In this work, the compression of the microcolumns utilized a nanoindenter XP (MTS Corp., USA) equipped with a flat punch indenter with a diameter of 15 μm for the ex-situ microcompression experiments. The CSM mode with a 2 nm oscillation and a frequency of 45 Hz at a constant strain rate of 0.005/s was employed. A typical experiment consists of a loading segment until the prescribed maximum displacement, followed by a 30 s hold segment before an unloading segment.

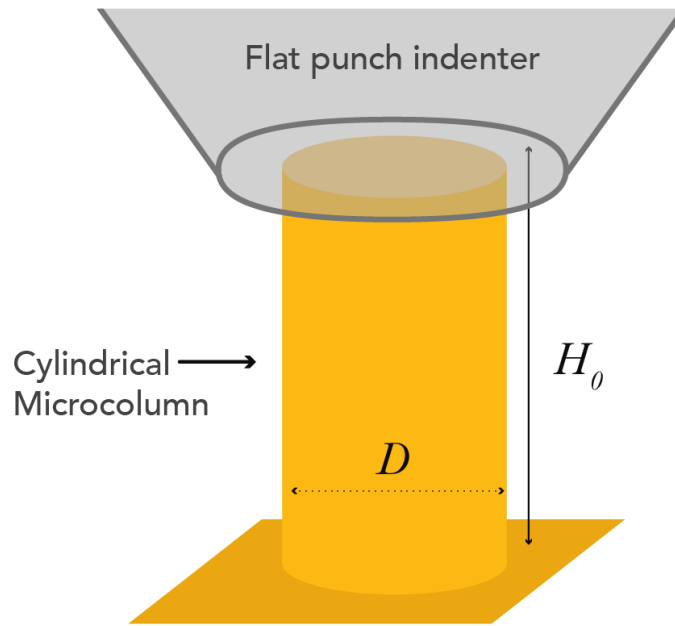


Figure 3.14: Schematic showing a microcompression of a cylindrical microcolumn by a flat punch indenter. It is indicated the initial height, H_0 , and the diameter, D , of the microcolumn.

Microcolumn fabrication for microcompression testing

The FIB fabrication of the microcolumns utilized in this work consisted of two single-pass milling steps, as follow:

- SEM was used to locate the position in which the microcolumns should be milled.
- The first step of single-pass milling is done to create a cylindrical structure with 35 and 16 μm of outer and inner diameter, respectively. A high current was used for this coarse milling (3 nA).
- The second step of single-pass milling takes place using a circular pattern since all microcolumns were cylindrical. Again, the inner diameter is equal to the final diameter of the microcolumn, and fine milling was used with currents of 0.3 nA.

Table 3.1: Typical dwell-times used in this thesis on the fabrication of microcolumns using two steps single-pass milling.

	Solid Gold	Solid Epoxy	NPG	NPG composite
1 st Step	5 ms	3.5 ms	1.5 ms	3 ms
2 nd Step	7 ms	5 ms	2.5 ms	4 ms

Since the removal rate by FIB varies according to the materials, the microcolumn fabrication differed in the dwell time. In this study, microcolumns were fabricated in solid gold, solid epoxy, NPG, and NPG-composites. Examples of typical microcolumns for each material are shown in Figure 3.15 (a), (b), (c) and (d), respectively. The microcolumn fabrication using a single-pass milling approach produced microcolumns with adequate tapering in all materials tested here. The typical dwell-time for the first and second milling steps for each material is shown in Table 3.1.

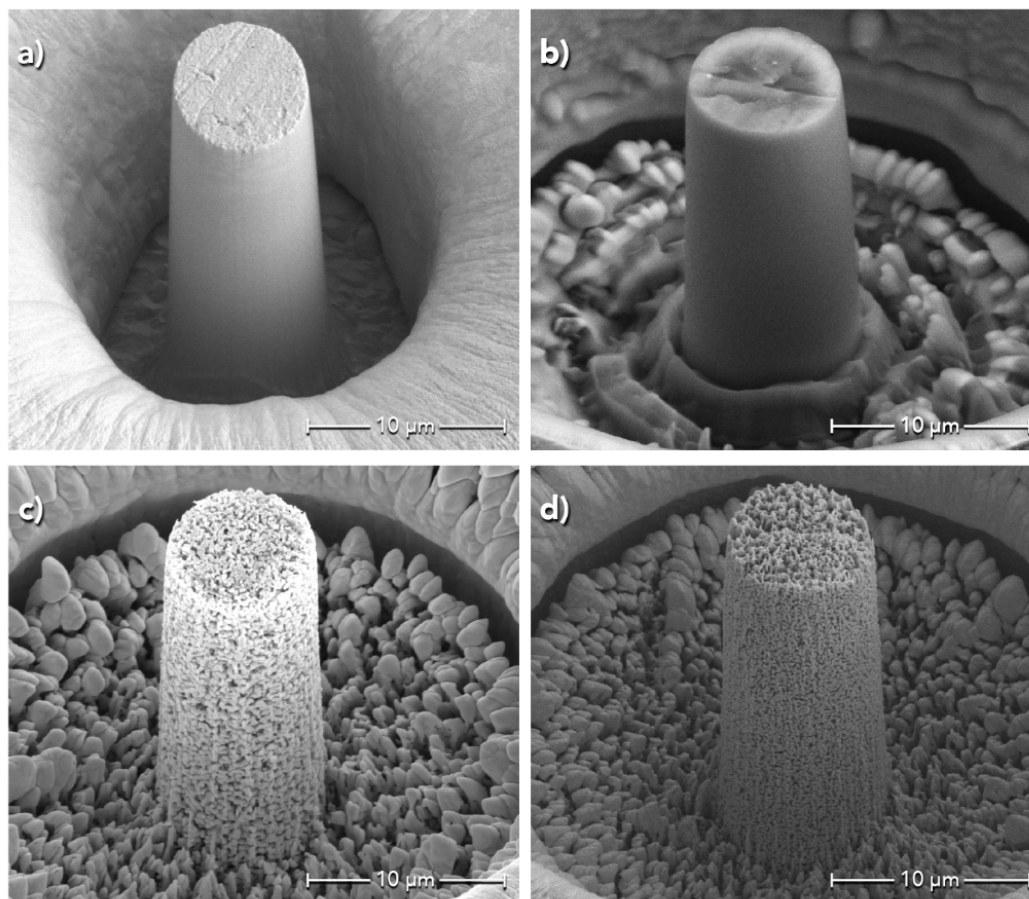


Figure 3.15: Typical microcolumns fabricated using two steps single-pass milling in solid gold (a), solid epoxy (b), NPG (c) and NPG composite (d).

Compression analysis

In the measured displacement, the overall compliance during a microcompression test includes the microcolumn compliance, the compliance associate with the substrate being pushed by the microcolumn, and the load frame compliance. Since the compliances, in this case, are additive, the displacement of the microcolumn, h_{column} , is given by:

$$h_{column} = h_{raw} - h_{surface} - h_{LF} - h_{substrate} \quad (3.14)$$

where h_{raw} is the raw displacement given by the system, $h_{surface}$ is the surface height identified at initial contact by the system, h_{LF} is the load frame displacement and $h_{substrate}$ is the substrate displacement. The load frame displacement is determined according:

$$h_{LF} = \frac{P_{column}}{K_f} \quad (3.15)$$

where P_{column} is the applied load and K_f is the load frame stiffness of the nanoindentation instrument. Sneddon's equation is used to determine the substrate displacement, and it can be expressed as:

$$h_{substrate} = \frac{P_{column}}{S_{substrate}} = \frac{(1 - \nu^2)P_{column}}{ED_{bottom}} \quad (3.16)$$

where $S_{substrate}$ is the stiffness of the substrate and D_{bottom} is the diameter of the column at the bottom.

The expressions for the engineering strain, ε_{eng} , can be obtained from Equation 3.14, as followed:

$$\varepsilon_{eng} = \frac{h_{column}}{H_0} \quad (3.17)$$

where H_0 is the initial height of the microcolumn measured by SEM imaging. Additionally, the expression for the engineering stress, σ_{eng} , for a cylindrical microcolumn is delivered by:

$$\sigma_{eng} = \frac{P_{column}}{A_0} = \frac{P_{column}}{\frac{\pi}{4}D^2} \quad (3.18)$$

where P_{column} is the load applied, A_0 and D are the area and the diameter of the microcolumn, respectively. Moreover, the yield stress was defined using an approach based on the loading stiffness described in [149, 150]. Finally, the elastic modulus, E , is obtained by combining the Equations 3.17 and 3.18, as follow:

$$E = \frac{\sigma_{eng}}{\varepsilon_{eng}} = \frac{P_{column}H_0}{h_{column}A_0} \quad (3.19)$$

3.4.3 Interfacial shear test

Evaluating the interface's mechanical integrity is a long-standing topic of interest in composite materials and coating technologies. Chen recently developed a new testing protocol to evaluate the shear strength in interlayers between coating-substrates systems [151, 152]. In this type of experiment, a bi-material cylindrical microcolumn containing an inclined interface is compressed uniaxially until the interface collapses. Generally, a 45° angle between the phases is

used to maximize shear from the column's compression. The compression is done by a flat punch indenter in a nanoindentation device to obtain the load-displacement response and identify the maximum load in which the interface collapses [151–154]. In this work, a similar approach was employed to evaluate the interfacial shear strength between gold-epoxy systems using two types of bi-material microcolumns: cylindrical and square cross-sectional microcolumns. Figure 3.16 shows a schematic of interfacial shear strength testing for a cylindrical microcolumn in (a) and a square cross-sectional (b). The diagram also contains the initial column height, H_o , the height of the polymeric part, H_p , and interfacial area, A_{int} , in terms of the side, l , and diameter, D , of the microcolumns.

The protocol developed by Chen served as a base for the experimental investigation developed in this work [151]. Nevertheless, since the microcolumns' fabrication involves a lathe milling approach, some adjustments were necessary to investigate a polymer-metal system. Although lathe milling produces "taper-free" microcolumns, it also highly exposes the materials to the ion beam. The interaction between materials and ions can alter the mechanical properties measured by micromechanical experiments [147, 148]. Therefore, an alternative using single-pass milling was developed to produce microcolumns with adequate geometries. Single-pass milling consists of slowly scanning the beam just once over the same area, spiralling from outside to inside. The combination of the incident angles and redeposition resulted in deeper cuts, reducing the tapering of the final microcolumns [27, 113].

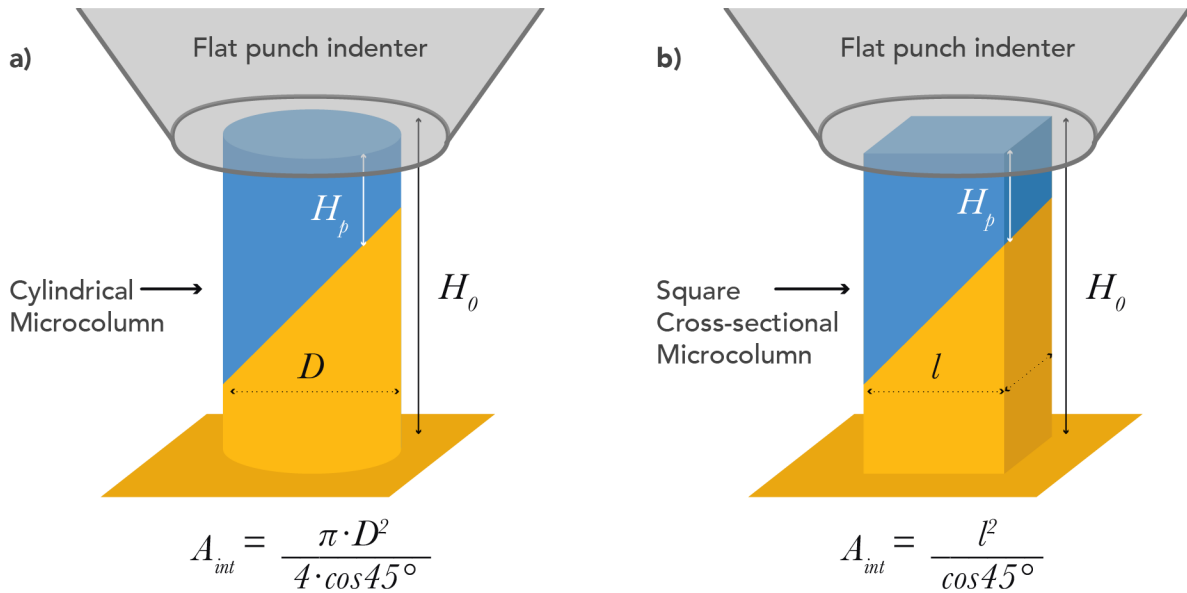


Figure 3.16: Schematic showing interfacial shear strength tests from cylindrical (a) and square cross-sectional (b) microcolumns. A flat punch indenter is driven into the top of the microcolumns. It is indicated the height of the microcolumns, H_o , the height of the polymeric part, H_p , and the calculated interfacial areas, A_{int} , for both geometries.

Furthermore, the compression of the microcolumns followed a similar approach as the nanoindentations carried out in this work. A nanoindenter XP (MTS Corp., USA) equipped with a flat punch indenter with a diameter of 15 μm was used for the ex-situ microcompression experiments. The CSM mode with a 2 nm oscillation and a frequency of 45 Hz at a constant strain rate of 0.005/s was employed. A typical experiment consists of a loading segment until the prescribed maximum displacement. Due to the nature of the test, the analysis of the collected data is limited after the interfacial failure. Nevertheless, the details and possible interpretations are further discussed in Chapter 6.1.

Microcolumn fabrication for interfacial shear testing

Samples containing a planar interface between gold and epoxy were used to fabricate microcolumns with size in the micrometre scale using FIB milling. The following is a list of the main steps used in the fabrication process:

- SEM was used to locate the position of the interface between gold and the epoxy.
- The first step of single-pass milling was done to create a cylindrical structure with 35 and 16 μm of outer and inner diameter, respectively. This coarse milling step used a relatively high current (3 nA) and a dwell time of 3 ms. The positioning of the circular pattern in the FIB imaging and the resultant milled structure by SEM imaging is shown in Figure 3.17 (a) and (b).
- For the cylindrical microcolumns, the second step of single-pass milling takes place using a circular pattern, in which the inner diameter is equal to the final diameter of the microcolumn. Fine milling is used here with currents of 0.3 nA and dwell time varying from 3 to 4 ms according to the microcolumn height. The positioning of the circular pattern in the FIB imaging and the resultant milled structure by SEM imaging is shown in Figure 3.17 (c) and (d).
- For the square cross-sectional microcolumns, the second milling step takes place using four rectangular patterns. They are positioned according to Figure 3.17 (d), leaving an intact square in the middle, in which the dimensions account for the microcolumn's side. Again, fine milling was used (0.3 nA), and the dwell time varied from 3 to 4 ms according to the height of the microcolumn.

The polymer height of the microcolumns could be adjusted by positioning the milling patterns closer or farther from the interface. Furthermore, the interfacial area between gold and epoxy in each microcolumn was measured in the SEM before the microcompression. This area was then used in the calculation of the interfacial shear strength.

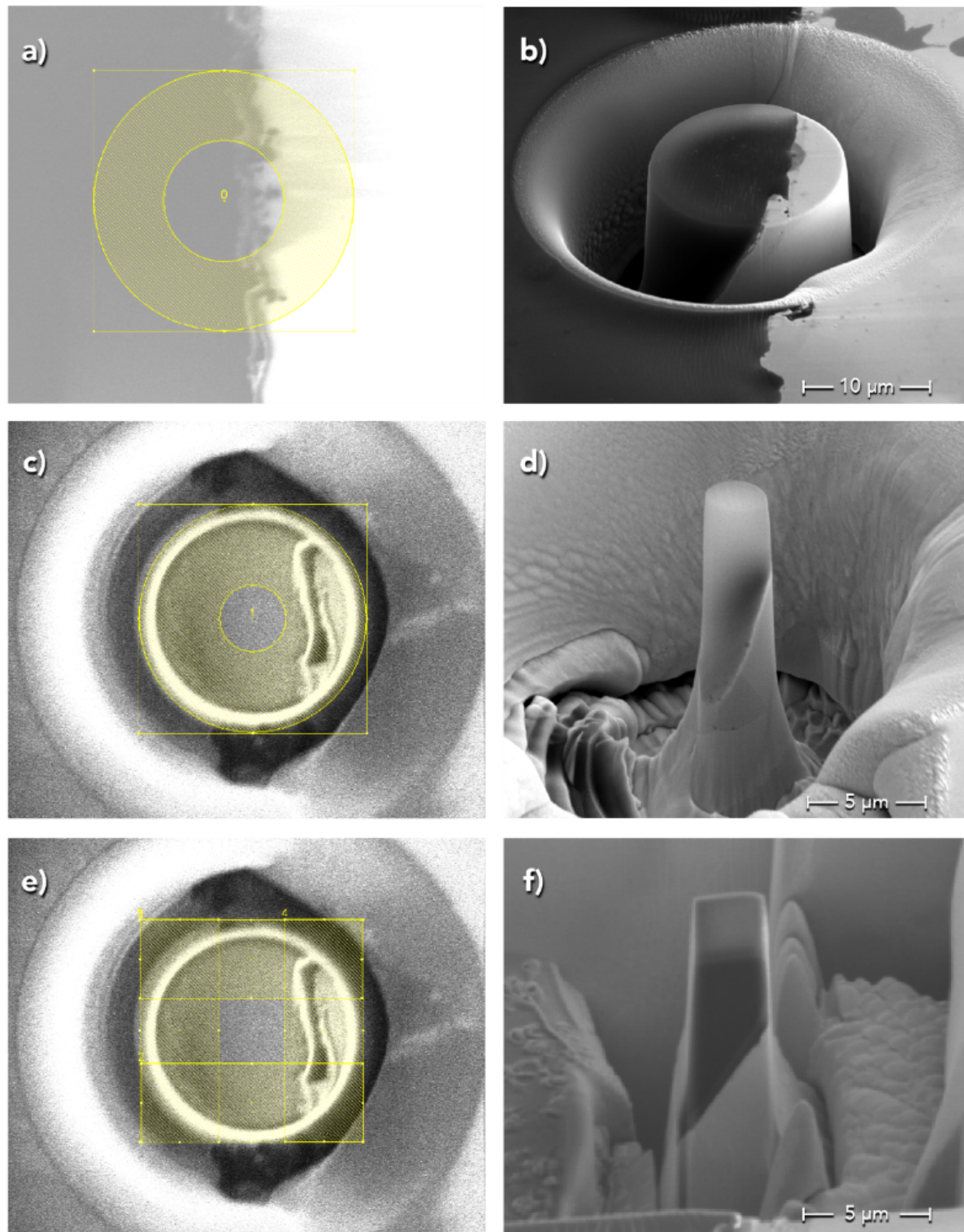


Figure 3.17: Steps on the fabrication of cylindrical and square cross-sectional microcolumns for interfacial shear strength testing. A structure is coarse milled first to facilitate the subsequent removal of materials (b), then single pass-milling is used to fabricate cylindrical (d) and square cross-sectional (e) microcolumns. The position of the milling pattern in the FIB imaging for each one of the previous steps can be found in (a), (c), and (e), respectively.

Shear analysis

Extracting the interfacial strength response from a microcolumn compression test requires considering several critical issues, most of which are inherent to a regular compression test. Therefore, factors such as the geometry and aspect ratio of the microcolumns, the misalignment to the flat punch, the deformation of the underlying material, the friction between the indenter and the top of the microcolumn would impact the measured values [155–160]. As an already established good practice, the microcolumn aspect ratio between 2:1 and 4:1 is a good compromise between barrelling and buckling. Additionally, keeping the misalignment angle lower than 1° avoids several artefacts that underestimated the measured properties [155]

Specific to microcolumns containing an inclined interface, the angle between the phases and the interfacial area are crucial to estimate the representative shear stress in which the interface collapses. Assuming that the shear failure of the interfacial regions initiates with a uniform shear deformation and that before the initiation, the stress is uniaxially distributed, the critical interfacial shear stress at the interfacial plane, τ_{45° , is given by:

$$\tau_{45^\circ} = \frac{P_{max} \cdot \sin \theta}{A_{int}} \quad (3.20)$$

where P_{max} is the maximum load, A_{int} is the interfacial area, and θ is the angle between the phases to the top of the microcolumn. Furthermore, the analysis of the measured displacement in the interfacial shear strength testing followed the same adjustment performed on analysing the microcompression experiments presented in the last section.

3.5 FEM simulation

Finite element simulations were carried out using Abaqus v.6.14 (Dassault Systems Simulia Corp, France) to evaluate the effect of the bonding strength on gold-epoxy systems. First, the compression of microcolumns with an inclined interface was simulated using a three-dimensional model. The simulated microcolumns contained the same dimensions as the physical experiments carried out to investigate the interfacial shear strength described in Chapter 6.1. For this purpose, the ABAQUS mesh generator was used to create the finite element mesh that consists of 8-node brick elements (C3D8). The approximate length of each element edge was requested to be smaller than an eighth of the column's side. An example of FE-mesh for a microcolumn with an inclined interface is shown in Figure 3.18 (a). In all simulations, the materials assigned to the top and bottom parts of the microcolumns were epoxy and gold, respectively. The constitutive law for each material is described later in this section.

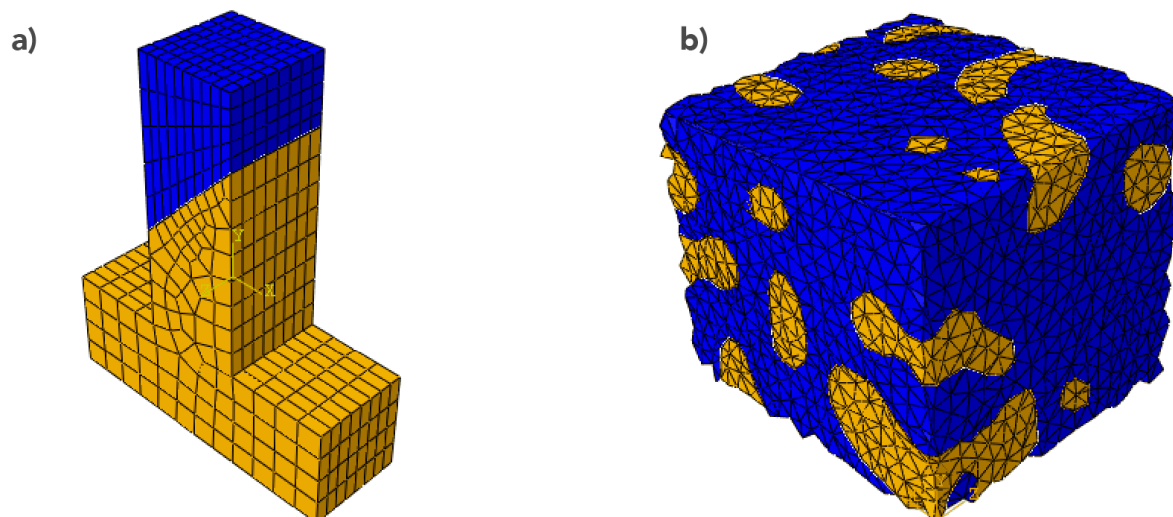


Figure 3.18: (a) 3D mesh of 8-node brick elements (C3D8) used to model the microshear test, the top and bottom sections were assigned the properties for epoxy and gold, respectively. (b) 3D mesh of 10-node quadratic tetrahedron elements (C3D10) used to model the NPG-epoxy composite compression. This mesh consists of a section of a larger mesh made from the reconstruction of the NPG-epoxy composites made by a FIB slice and view technique [11]. In both meshes, the elements assigned with the epoxy and gold properties are represented in blue and yellow, respectively.

Second, a finite element approach was also utilized to simulate the compression of NPG-epoxy composite. Kaixiong Hu first developed a FIB based slice and view technique to create a 3D reconstruction of NPG [11]. Moreover, he used Amira software to generate a triangular surface mesh based on the NPG's 3D reconstructions, converted to a C3D10 mesh (10-node quadratic tetrahedron). In this mesh, the element size was kept small enough to preserve the Au ligaments' geometry [11]. Further, an epoxy phase was added to the model filling the porosity on the initial NPG mesh. Hu simulated the compressive response of these structures, assuming a perfect bonded interface between the two phases that stayed bonded throughout the compression [11]. In this work, the composite's 3D mesh created by Hu based an expanded model accounting for the interfacial behaviour between gold and epoxy materials.

The experimental investigation with the inclined interfaces inspired the development of a surface-based cohesive behaviour approach to simulate the interface in the interfacial shear strength test and the compression of NPG epoxy composites. Since the assignment of a surface property made the model exceptionally computationally demanding, the total volume simulated was reduced compared to previous works. An example of FE-mesh for a NPG-epoxy composite is shown in Figure 3.18 (b). Here, the input for the interfacial behaviour was taken from the microshear experiments. The details of the development of interfacial modelling are described in Section 6.2.

3.5.1 Boundary conditions and materials properties

The boundary condition applied to the microcompression model of the interfacial shear strength testing is illustrated in Figure 3.19 (a). The load was applied as a homogeneous displacement of all nodes on the top side of the microcolumn. Meanwhile, a symmetry boundary condition ($y_0=0$) was applied to the bottom surface on the bottom part of the microcolumn. All nodes on the side faces of the microcolumn were free to move during the uniaxial compression simulation. Regarding the boundaries on the composite simulations, symmetric boundary conditions were applied to the nodes on the planes $x_0, y_0, z_0 = 0$, as shown in Figure 3.19 (b). The load was applied as a homogeneous displacement in all the nodes of the opposite surfaces (x_1, y_1, z_1) accordingly to the analysis.

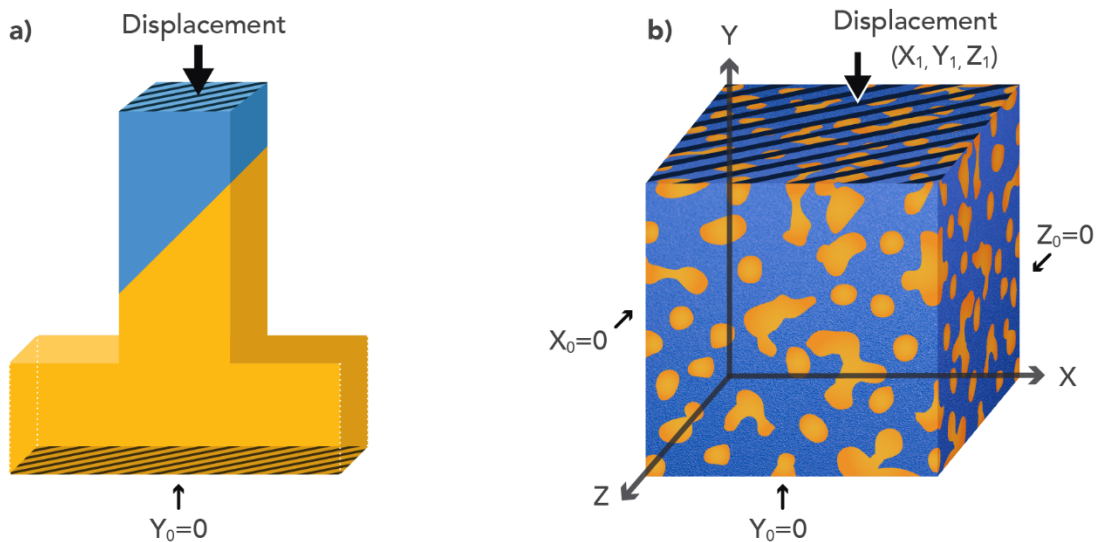


Figure 3.19: Symmetry boundary condition was applied in (a) to the nodes on the bottom surface of the gold part of the microcolumn while the displacement was applied to the top nodes of the epoxy part, as represented by the black arrow. The symmetry boundary conditions in (b) were applied to the nodes on the planes $x_0, y_0, z_0 = 0$, while the displacement was applied to the nodes of the surface, as represented by the black arrow.

In this study, the same constitutive laws from similar works were adopted for describing the properties of gold and epoxy phases. Although gold's size effect and epoxy's time-dependent response are not considered, this approach was capable of a reasonable fit to the experimental results. It considers an isotropic elastic-linear plastic stress-strain relation, as illustrated in Figure 3.20. In terms of the actual properties, gold's yield stress, elastic modulus, and work hardening are 700 MPa, 81 GPa, and 1000 MPa, respectively. Moreover, for the epoxy, an elastic modulus of 4.7 GPa and hardness of 97 MPa were considered. No work hardening was considered for the epoxy property. Finally, the Poisson's ratio of gold and epoxy computed were 0.42 and 0.35, respectively.

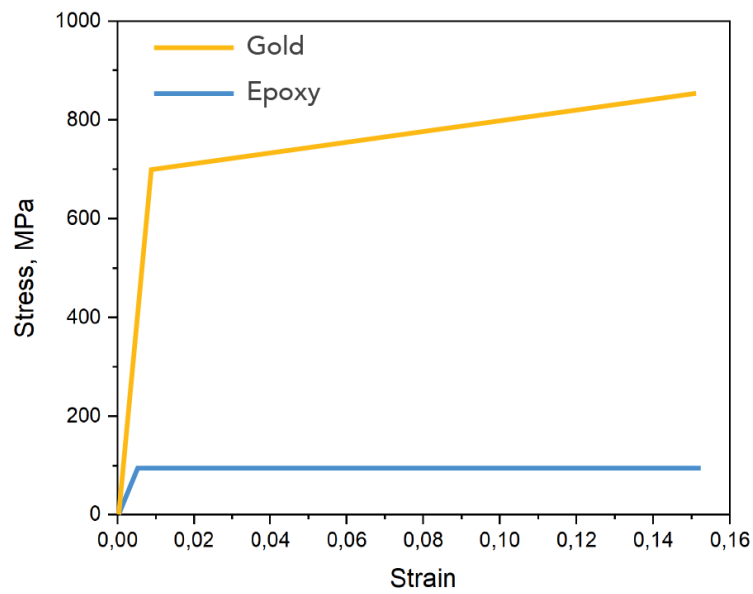


Figure 3.20: Plot showing the constitutive laws for gold and epoxy used in this work, represented by the yellow and blue lines, respectively. Constitutive law of gold with yield stress $\sigma_{y,gold} = 700$ MPa, elastic modulus $E_{gold} = 81$ GPa and work hardening rate $\dot{\gamma}_{gold} = 1000$ MPa. Constitutive law of epoxy with yield stress $\sigma_{y,epoxy} = 97$ MPa, elastic modulus $E_{epoxy} = 4.7$ GPa and no work hardening.

4 The mechanical response of the polymeric phase

In this chapter, the independent mechanical response of the polymeric phase of NPG-epoxy composites is investigated. Questions regarding the influence of the sub-micron scale of the polymer phase in the composites, the possible presence of an interlayer, and the complex morphology of the NPP structure are addressed experimentally. First, the effect of the small length-scales in bulk epoxy is investigated by carrying out shallow nanoindentation measurements. Then, the nanoporous polymers are introduced as the separated polymeric phase from NPG-polymer composites, which allowed for the investigation of the effects of the small length-scale and the morphology on these structures. A better understanding of the presence of an interlayer and the possible impact on the mechanical response was obtained by comparing NPP samples with fine and coarse structures. Finally, the results from the micromechanical characterization of the NPPs structures are then presented and discussed.

4.1 Considerations on the bulk polymer properties

In this study, nanoindentation experiments were carried out to evaluate the size-dependent mechanical response of the epoxy used in the NPG-polymer composites. Here the measurements were conducted in polished bulk samples, as shown in Figure 4.1 (a). CSM method was used to measure the hardness and elastic modulus as a function of the indentation depth, as described in Chapter 3.4.1. The measurements are reproducible, reaching $2\ \mu\text{m}$ at a maximum load of 18 mN approximately. The average modulus and hardness for ten measurements as a function of the indentation depth are shown in Figure 4.1 (b) and (c), respectively. As can be observed in both plots, the response presents an exponential decay as a function of displacement until a plateau appears. The bars representing one standard deviation about the mean show a considerable variation at small depths, which can typically indicate heterogeneities on the polymer composition or surface roughness, inducing errors in determining the contact area [161].

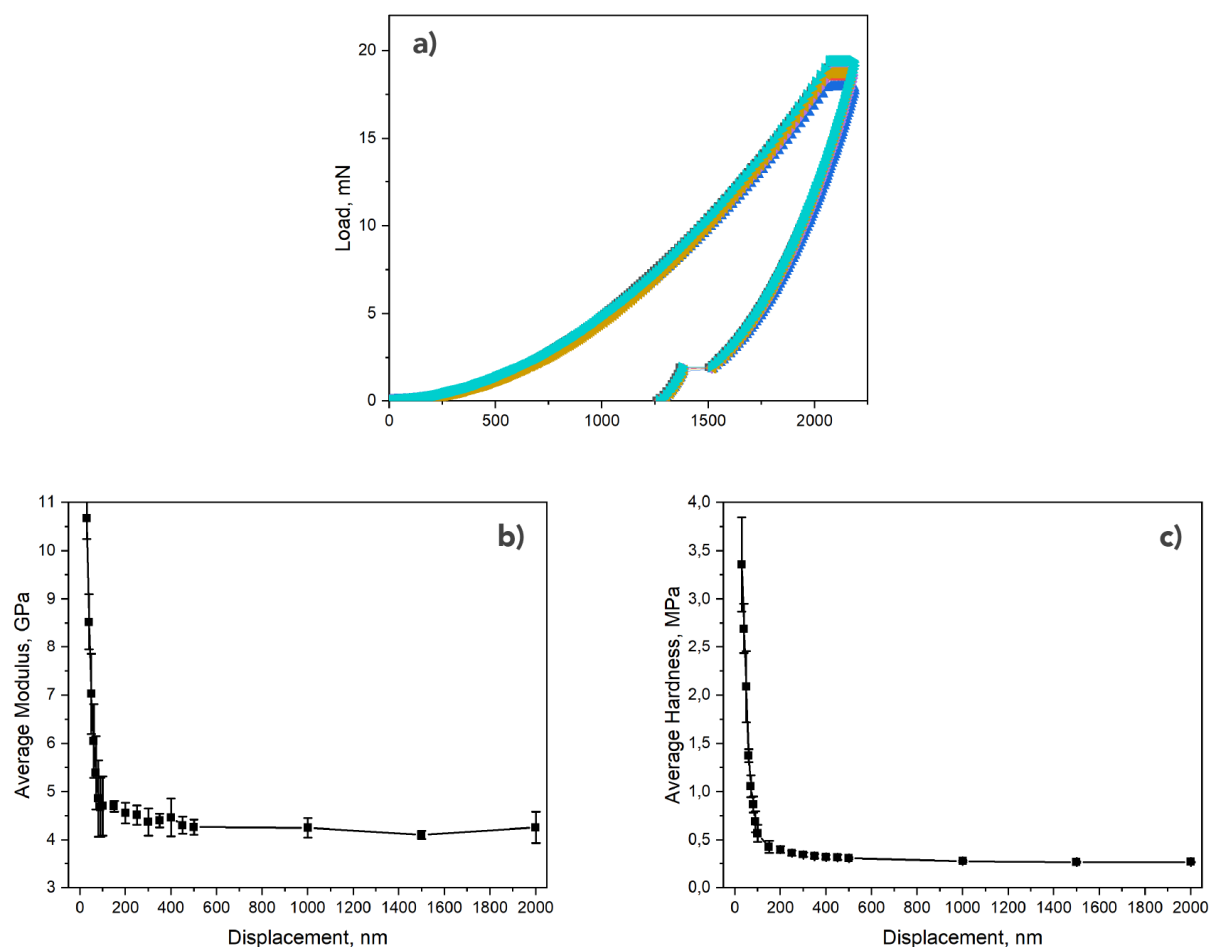


Figure 4.1: (a) Load-displacement curves from 10 nanoindentation tests in bulk epoxy. The displacement plateaus are associated with creep relaxation during the hold segments in the loading cycle. (b) and (c) shows the average elastic modulus and hardness from continuous stiffness measurement as a function of the indentation depth, respectively. Each data point represents an average of 10 measurements, and the error bars indicate one standard deviation about the mean value.

These results agree with many studies in the literature showing experimentally observed length scale-dependent deformation of epoxies by nanoindentation testing [16, 22–27]. Although graphically, a trend on the average values indicates ISE on hardness and modulus, a statistical analysis is necessary to reduce the uncertainties in comparing data at different depths. Figure 4.2 shows a section of the values measured in the plots from Figure 4.1 (b) and (c), in which it is possible to observe the overlapping of averages and standard deviation at small depths.

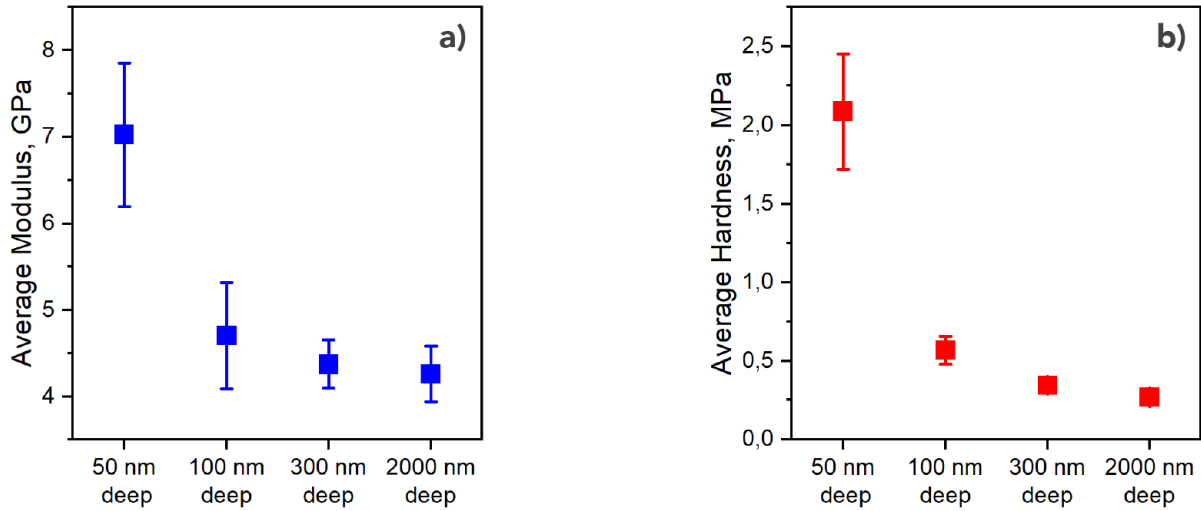


Figure 4.2: (a) and (b) present the bulk epoxy average elastic modulus and hardness, respectively, from continuous stiffness measurement in the depths analysed on the t-tests. Each data point represents an average of 10 measurements, and the error bars indicate one standard deviation about the mean value.

In this investigation, traditional hypothesis testing was used to investigate the indentation depth involved in the ISE of bulk epoxy. A two-sample t-test allows the comparison between average results of two populations determining if the difference is statistically significant or if it is due instead to random chance. In this context, a population is a group of measurements carried out under the same circumstances, e.g., indentations carried out at the same indentation depth. Here, t-tests were conducted to compare three sets of pairs of populations, as follows:

- Properties at 50 nm against properties at 300 nm,
- Properties at 100 nm against properties at 300 nm,
- Properties at 300 nm against properties at 2000 nm.

In a t-test, the null hypothesis H_0 states that there is no statistically significant difference between the two populations, and it can be rejected whenever the calculated t-value is greater than a critical value that depends on the level of significance. The t_{value} can be calculated according to:

$$t_{value} = \frac{\bar{x}_1 - \bar{x}_2}{\sqrt{\frac{\sigma_1^2}{n_1} + \frac{\sigma_2^2}{n_2}}} \quad (4.1)$$

Where \bar{x} , σ , n are the mean value, the standard deviation and the population size, respectively. The subscripts 1 and 2 represent the two populations in a set. If the calculated t_{value} is greater than a critical value, the H_0 can be rejected, which suggests a statistically significant difference between the two populations. The calculated t-values for hardness and modulus are

presented in Table 4.1. It is considered a normal distribution, and for 18 degrees of freedom, the critical values for a confidence level of 95% and 99,9% are 2.11 and 3.922, respectively.

Table 4.1: t_{value} calculated for the comparison of different indentation depths into bulk epoxy. The red font was used to represent values smaller than the critical values, in which the hypothesis of no statistical difference in the comparison can not be rejected.

Property	t_{value} 50 nm to 300 nm	t_{value} 100 nm to 300 nm	t_{value} 300 nm to 2000 nm
Hardness	12.675	7.855	10.279
Modulus	7.115	1.553	0.840

In the case of hardness, t_{value} is greater than the critical values in all comparisons. This indicates a factor acting on the measured values according to the indentation depth, which could be evidence of size effects. Nevertheless, the critical values in modulus are greater than the t-values in the comparisons between 100 to 300 nm and 300 to 2000 nm. This means that the null hypothesis can not be rejected for these comparisons, and there is no statistically significant difference between these groups. The difference found between 50 to 300 nm is unlikely to be due to size effects. Instead, at indentation depths below 100 nm, the calculation of the contact area is susceptible to bluntness on the indenter tip [57].

4.2 Composites made from polymeric infiltration

The open porous polymeric structure remaining from the Au-etching of NPG-epoxy composites is presented in this section. Figure 4.3 shows a cross-section milled in a representative NPG-epoxy composite before the Au etching in which the mean ligament size of the NPG was 400 nm. The Au ligaments appear in the bright phase, and the dark phase is the polymeric structure. A low voltage was used in this picture (2 kV), revealing the Au ligaments surrounded by the polymer phase entirely. The mean ligament sizes of the NPG from the composites presented in this section were 50 nm and 400 nm, and here they are referred to as fine and coarse NPP structures, respectively.

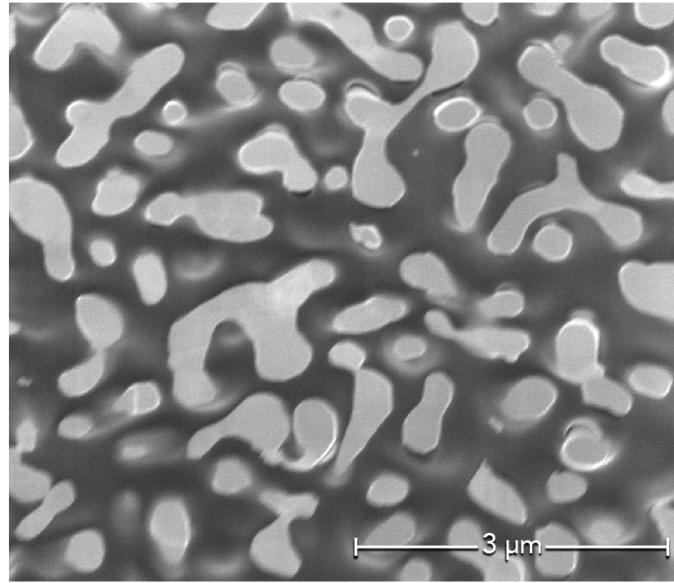


Figure 4.3: SEM micrograph showing a FIB milled cross-section of a NPG-epoxy composite with a ligament size of 400 nm. The gold ligaments appear in a bright colour and the epoxy in grey.

4.2.1 Leaching of Au in NPG-polymer composites

Figure 4.4 shows the surface of an NPG-epoxy composite with a mean ligament size of 200nm that was submerged in liquid mercury for 40 hours. The SEM imaging at a low voltage reveals that some exterior features were leached out, leaving open holes on the surface. Nevertheless, by increasing the electron beam voltage, it is possible to recognize the gold ligaments below the immediate surface of the polymer. The mercury was not able to penetrate the small ligament structure, and the dissolution of the NPG was restricted to the superficial features of the sample. This behaviour can be readily explained by the high surface energy of the liquid mercury that prevented direct contact with the Au inside the submicron ligament structure.

Fortunately, the treatment using the iodine-iodide solution was more effective. In this case, the dissolution started on the surface, where the solution first established contact with the NPG. Thereupon, as the NPG was dissolved, the solution penetrated the core of the sample. Figure 4.5 (a) shows the aspect of a surface of an NPG-epoxy composite sample treated in the iodine-iodide solution. Figure 4.5 (b) shows a cross-section of the same composite after just one hour in the iodine-iodide solution. It is possible to distinguish the leaching out of the nanoscale Au ligaments on the surface region and their presence at the core of the samples. The cross-section was prepared with a Ga^+ based focused ion beam (FIB) at a final aperture current of 0.1 nA to ensure an adequate smoothness of the analysed surfaces.

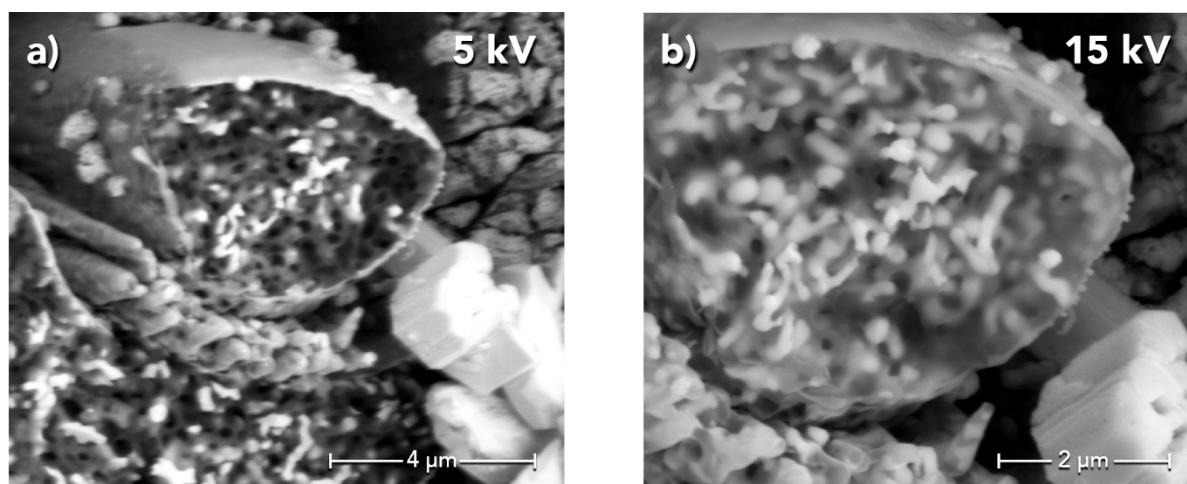


Figure 4.4: SEM micrograph showing the microstructure at the surface of an NPG-epoxy sample after 40h submerged in liquid mercury. A low voltage is applied in (a) revealing some small open holes on the sample's surface, indicating the partial removal of Au ligaments. Nevertheless, increasing the voltage in (b) showed that the gold ligaments are still present underneath the outer surface.

It was observed that the iodide-iodine solution was not able to effectively remove the Au from the deep regions of composites made from very fine NPG (mean ligament size of 20 nm). Figure 4.6 (a) shows the resulting microstructure after the etching process. The schematic in Figure 4.6 (b) presents a further increase in magnification on the removing front showing that the small porous structure gets blocked, which prevents the penetration of the solution into the sample. This behaviour was only found on very fine structured samples; for NPG ligaments larger than 20 nm, the solution was able to complete leach out the Au.

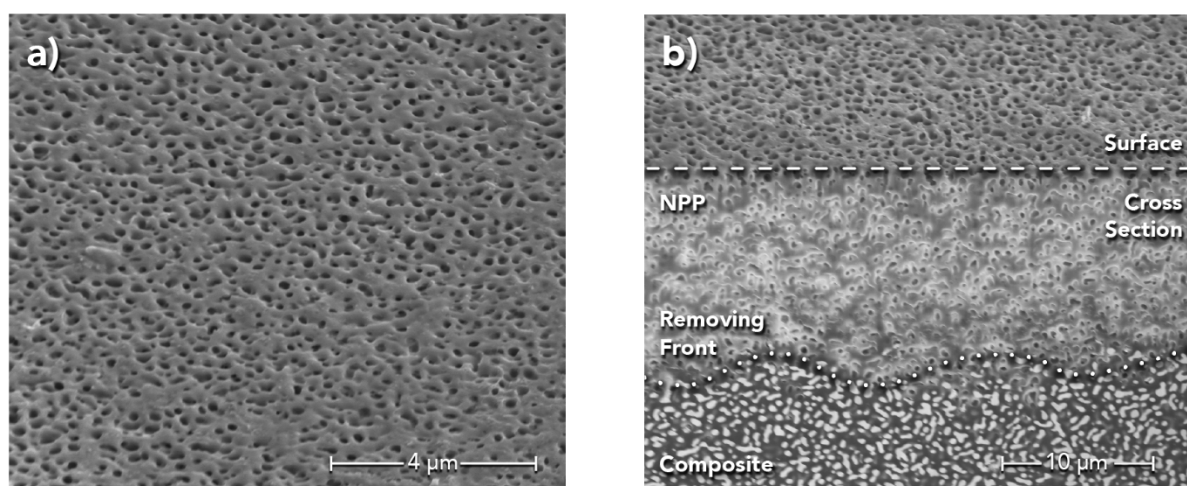


Figure 4.5: SEM micrographs showing the microstructure after a short period in iodine-iodine treatment. (a) shows the outer surface of the sample and (b) a FIB-milled cross-section, in which the removing front of Au can be observed.

All the nanoporous polymer samples fabricate in this work were prepared using a wet etching approach based on the iodide-iodine solution. It was found that the Au removal rate was directly related to the NPG ligament size. Stirring agitation and long periods of more than 24 h were sufficient to dissolve the small NPG ligaments from volumes large enough to ensure reliable micromechanical measurements.

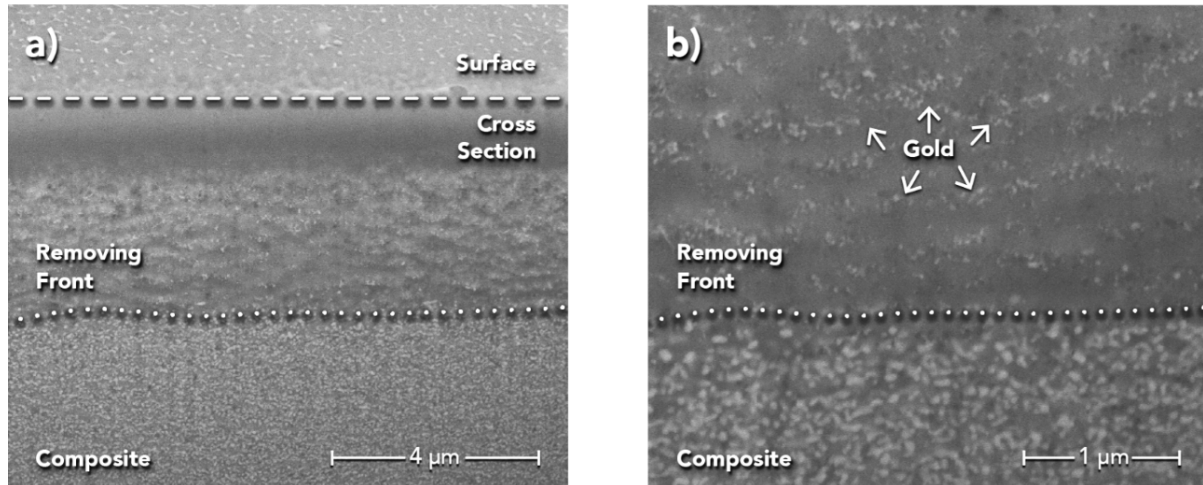


Figure 4.6: (a) SEM micrograph showing the microstructure in a FIB milled cross-section of a very fine NPG-epoxy composite treated in iodine-iodine solution. Some ligaments were partially leached out; however, gold can still be observed behind the removing-front in (b).

4.2.2 Morphology of the isolated polymeric phase

After the iodine-iodide treatment, the Au phase is completely removed, and the polymer phase is left preserved. Similar to the NPG, these nanoporous polymers are bicontinuous structures made of polymer and porous. Figure 4.7 (a) shows the aftermath in a sample in which the NPG before the etching procedure had a mean ligament size of 400nm. A cross-section was prepared using FIB milling, revealing that Au was entirely removed from the interior of the sample.

In addition to the SEM imaging, energy dispersive x-ray spectroscopy (EDS) was carried out and confirmed the absence of gold on the NPP structures. The EDS spectrum is shown in Figure 4.7 (b); this analysis was conducted in an EDAX spectrometer attachment to the SEM at a voltage of 15 kV, which is sufficient to identify the presence of gold [125]. The in-situ EDS allowed the mapping feature to localize the distribution of the elements on the sample surface. The section in Figure 4.7 (b) shows the arrangement of the carbon element overlapping with the features of the analysed microstructure, and the iodide element spread in a lower intensity. Only 1% of the atoms on the sample surface was quantified as iodine by the EDS analysis after washing the sample for 24h.

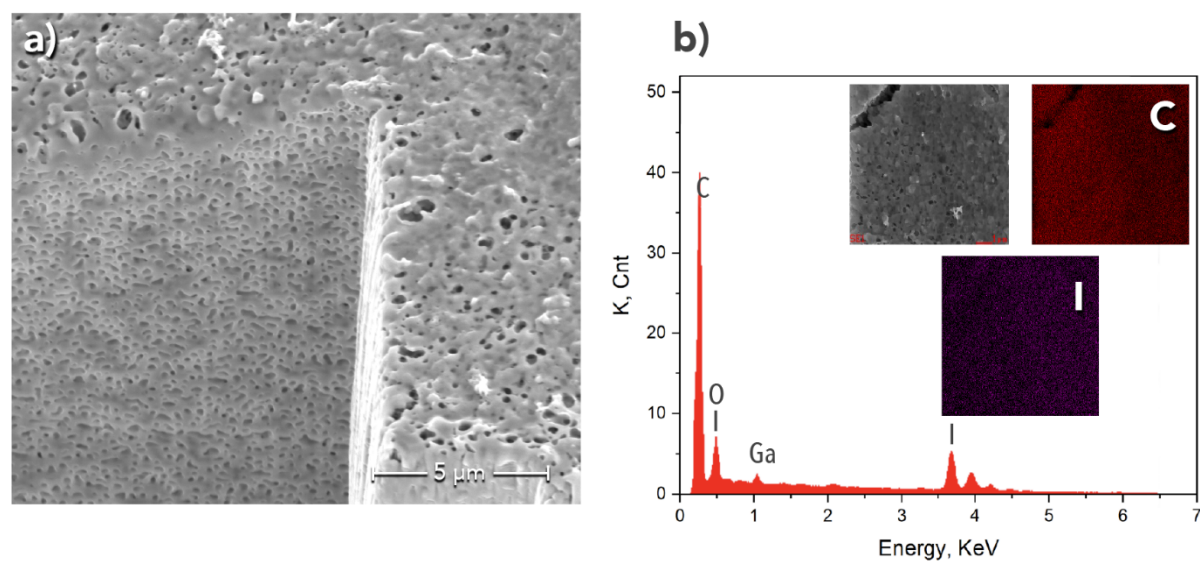


Figure 4.7: (a) SEM micrograph showing a FIB milled cross-section on the aftermath microstructure in a sample in which the NPG before the etching procedure had a mean ligament size of 400nm. (b) EDS spectra of NPP sample after the etching treatment, showing no presence of gold element. The gallium and iodine peak in the spectra are present because of the FIB milling of the cross-section and the etching treatment, respectively. The inset pictures present the elemental mapping of carbon and iodine.

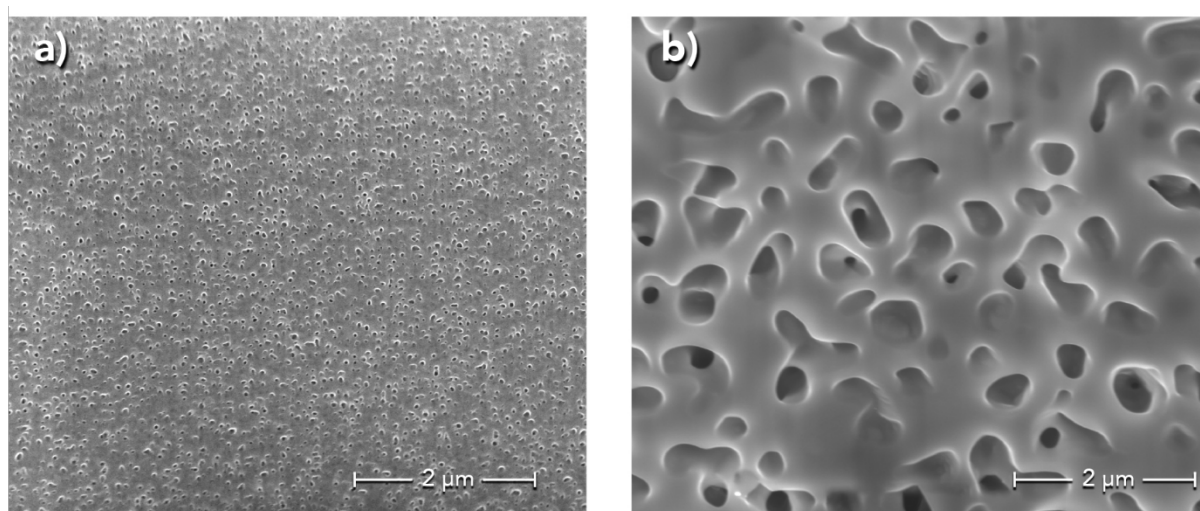


Figure 4.8: FIB milled cross-section of nanoporous polymer (NPP) showing at same magnification a fine (a) and a coarse (b) structures. This image was already published in [99]

Figure 4.8 shows SEM micrographs of FIB milled cross-sections at the same magnification from the two NPP configurations investigated in this study. Although the structures are similar, the porosity was tailored to achieve a different length scale. The bicontinuous NPG network structure dictated the microstructural length-scale of the NPP structures, in a self-similar way, the pore size of NPG, the ligament size of the polymer phase is found to be approximately two times larger than the ligament size of the gold phase. BoneJ plugin for the Fiji software package was

utilized to measure the mean pore size from both NPP configurations. Figure 4.8 (a) and (b) presents fine and coarse NPP structures, with mean ligament size of approximately 100 and 600 nm, respectively.

4.2.3 Mechanics of the isolated polymer phase

A series of nanoindentations were carried out to investigate the effect of the microstructural length-scale on the NPP mechanics. The influence of the iodine-iodide solution on the polymer phase was also investigated by indenting the bulk polymer before and after submitting it to the leaching treatment. First, the storage modulus was obtained using continuous stiffness measurements equipped with a 15 μm diameter flat punch indenter. The indentations were carried out to 3 μm displacement, followed by a hold segment in load with an applied oscillation amplitude of 50 nm over a frequency range of 1 to 45 Hz, followed by unloading. A second set of nanoindentations was conducted using a Berkovich indenter tip to evaluate the hardness of the NPP structures. The storage modulus, which represents the ability to store deformation energy in an elastic manner, was observed to be constant over the tested frequency range for all samples. More importantly, it was found that no significant difference in mechanical response between the bulk polymer before and after being treated to the leaching solution was found. This indicates that the polymer preserved its mechanical integrity during the long period of immersion in the iodine-iodide solution and allows the NPP data to be interpreted as representative of its properties in the Au-epoxy composite structure. Furthermore, a prediction of the storage modulus of the NPP was computed using the bulk polymer results assuming an isostrain condition [162] and the known volume fraction of the polymer phase of 75%. The isostrain prediction serves as a very good lower bound to the data.

It was found that the storage modulus obtained by flat-punch indentation on the coarse and fine NPP samples showed similar behaviour across the frequency range, as shown in Figure 4.9 (a). These results suggest that the microstructural length-scale does not affect the amount of elastic stored energy of the NPP samples, consistent with microcompression studies of bulk epoxy [163]. The corresponding loss moduli from the same set of indentations are shown in Figure 4.9 (b). The loss modulus, which represents the measure of the energy dissipation, was found to be two orders of magnitude lower than the storage modulus, which indicates the predominant elasticity of this material system. Interestingly the fine NPP behaved differently to the coarse NPP, maintaining the dissipated energy over the tested frequency range, while the coarse NPP showed a decrease in the loss modulus with increasing frequency.

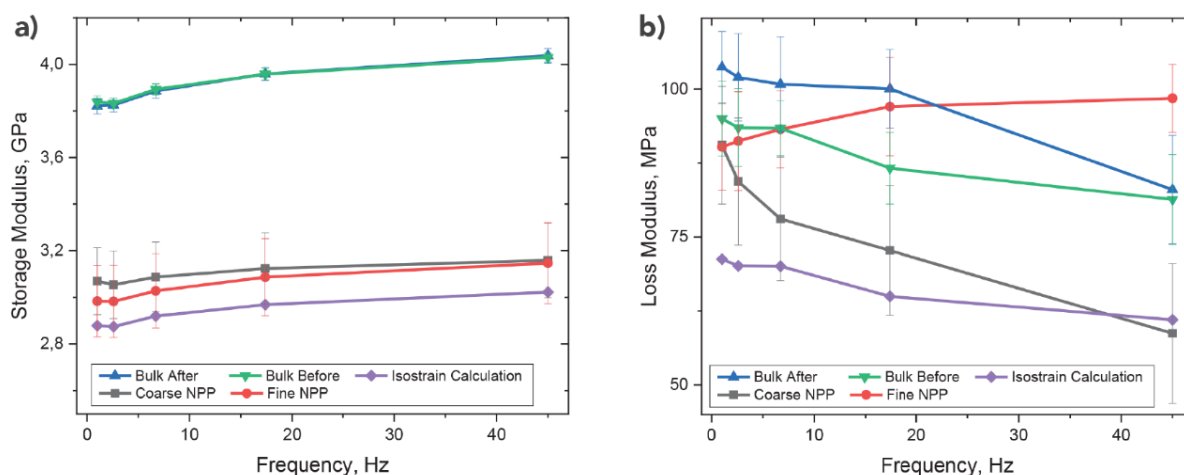


Figure 4.9: (a) The storage modulus and (b) loss modulus as a function of excitation frequency for the coarse NPP (black), the fine NPP (red), and the bulk polymer before (green) and after (blue) leaching solution treatment, and the isostrain calculated response (purple) based on the bulk measurement. Each data point represents an average of 15 measurements, and the error bars indicate one standard deviation about the mean value. This image was already published in [99]

Generally, frequency sensitivity in polymers is understood in terms of molecular motion [164], which can be strongly inhibited if the molecules are highly cross-linked [165] or strongly anchored by particles [166]. Conversely, the motion could be facilitated by the addition of a plasticizer [167]. Some studies have shown that relaxation of the constraints to motion can also be achieved by introducing free surfaces into the system [168, 169]. It is suggested here an interpretation of the difference between coarse and fine NPP based on the higher internal free surfaces of the smaller structured NPP, which might facilitate molecular motion in the vicinity of the pores. Although both NPP samples have the same volume fraction of polymer, the surface area of the fine NPP is larger due to its smaller microstructural length-scale. The molecular motion occurs at a much smaller scale than the pore size [170], resulting in the correlation with internal surface area and not on the volume occupied by the porous phase. At lower frequencies, the structures have sufficient time for relaxation, and the response of the fine and coarse NPP structures converge.

Berkovich indentations are needed here to compare the hardness of the samples. The sharp tip ensures plastic deformation instead of the elasticity dominated response of flat punch indentations. However, identifying the actual contact area can be difficult, especially for polymeric materials prone to various types of time dependency. The load divided by the square of the contact stiffness, P/S^2 , is a directly measured experimental parameter that does not depend on the contact area; it is proportional to the hardness and inversely proportional to the square of the modulus [140]. Since the flat punch indentation results indicated that the elastic response is independent of the microstructural length-scale, any variation in the P/S^2 should reflect changes in the hardness.

Figure 4.10 (a) presents the ratio between load and stiffness squared by the indentation depth from three representative curves showing the response of coarse and fine NPP structures and the bulk epoxy scaled using the isostrain law.

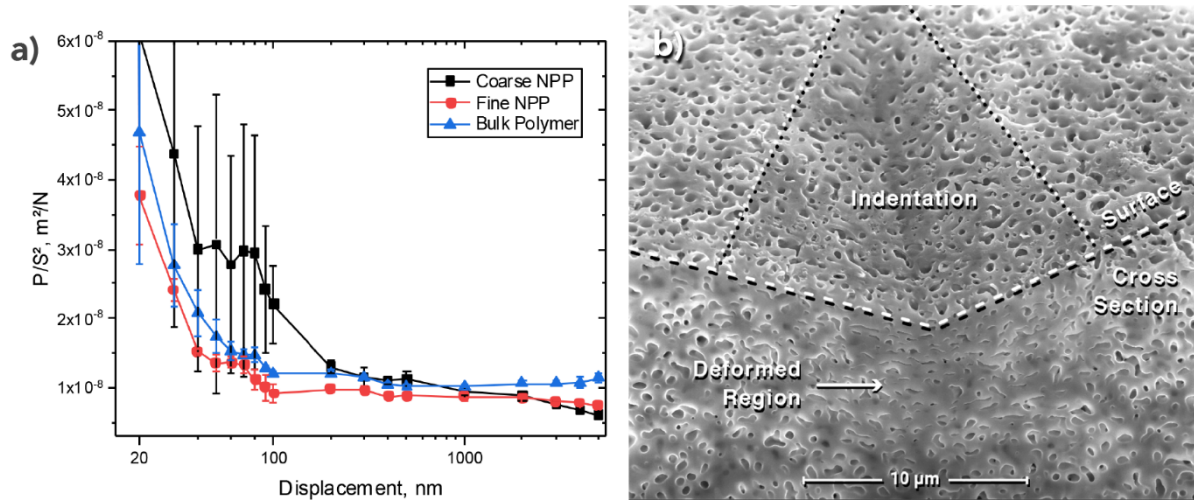


Figure 4.10: (a) The load divided by the square of the stiffness response, as a proxy for the hardness divided by the square of elastic modulus, as a function on indentation depth for the fine NPP (red line), the coarse NPP (black line) and the bulk polymer (blue line). Each data point represents an average of 10 measurements, and the error bars indicate one standard deviation about the mean value. (b) An SEM micrograph of a cross-section through an indent in the fine NPP sample revealing the densification below the indenter. The image is taken with the sample tilted 52° to reveal the indented surface and the cross-section. This image was already published in [99]

The indentations on bulk epoxy revealed an indentation size effect at depths smaller than 100 nm. Studies have shown that the indentation size effect in polymers might be attributed to the formation of strain gradients caused by a molecular kinking mechanism [38]; epoxies are prone to exhibit this behaviour due to their aromatic components [162]. A similar behaviour could be clearly identified in the fine NPP but not in the coarse NPP. Instead, a strong scatter in the initial response of the coarse NPP is observed, expectedly due to the proximity between indentation depth and ligament size resulting in the indenter tip touching single ligaments or pores for the first few hundred nanometres. After the first hundred nanometres, the response for coarse and fine NPP could not be differentiated. Using the measured modulus from the flat punch indentation, the indentation hardness is computed from the P/S^2 data in the plateau region to be 110 MPa. However, both fine and coarse responses are shown to deviate from the scaled bulk behaviour at deeper indentation depths. This behaviour is readily explained by the densification of the porous structure, leading to an increase in the effective modulus and thus a decrease in P/S^2 . An SEM micrograph of a cross-section made using FIB through an indent into the coarse NPP structure is shown in Figure 4.10 (b). The reduced pore size in the vicinity of the indent is observed, confirming such densification.

4.3 Conclusions

The existence of size-dependent mechanical response in epoxy was evaluated by nanoindenting bulk samples and characterizing size tailored structures of nanoporous polymers. Indentation size effect was observed in the bulk polymer in the hardness response. However, no statistically significant difference was found to support the hypotheses of a size-dependent elastic modulus. A trend also observed in the response of the small structured nanoporous polymer.

It was found that a standard approach used in the mining industry for leaching Au from rocks can be adapted to nanoporous Au composite materials in order to create novel nanoporous polymer (NPP) structures. The treatment of NPG-epoxy composites in an iodine-iodide solution led to bicontinuous NPP structures. Nanoindentation studies showed that the solution did not degrade the epoxy phase. It was found no evidence supporting the influence of the structure size in the elastic or plastic response, and the modulus of the NPP structures could be well predicted by an isostrain law applied to the modulus measured on bulk epoxy using the corresponding volume fraction. The storage modulus was found to be two orders of magnitude higher than the loss modulus for all samples, as expected for bulk epoxy resin. Nonetheless, significant differences in the loss moduli were found; the fine NPP showed a constant if not increasing loss moduli with excitation frequency, while both the coarse NPP and bulk epoxy showed a decreasing modulus. The preservation of the energy dissipation across all tested frequencies in the fine NPP with an inherently high specific surface area points to the role of free surfaces in the relaxation of polymeric chains.

5 On measuring the mechanical characteristics near the gold-epoxy interface

In this chapter, the mechanical characteristics near the gold-epoxy interface are investigated using planar interfaces as a simplified model sample to NPG-polymer composites. The planar interface sample was utilized as an alternative to circumvent the influence of the complex morphology and geometry of the composite. Questions regarding the presence of interlayer are addressed experimentally. An interlayer would display a region with constant properties and defined thickness, while a direct transition between two phases may result in a gradient of the local mechanical properties. Both possibilities are covered by the approaches in this chapter. First, the presence of an interlayer was investigated by chemical analysis, observing the distribution of gold elements near the interface. Then, transmission microscopy was used to image at very high magnification the interfacial region of NPG-epoxy composites. Finally, a better understanding of local transitional mechanical properties between gold and epoxy was obtained by carrying out a series of nanoindentations in line crossing the phases' boundaries. Furthermore, the impact of the nanoindentation parameters, e.g., depth or spacing, was estimated for the lines on the bulk materials and crossing the interfaces. Lastly, the local properties were analysed in terms of the proximity to the interface and the bulk properties.

5.1 Interlayer formation

This section aims to evaluate the presence of an interlayer between gold and epoxy phases, using planar interfacial samples and the NPG-epoxy composites itself. Under typical conditions, an interlayer between bulk metal and the bulk polymer could be explained by two possibilities: an oxide layer, previously present on the metal's surface [171, 172], or a layer originated by the interaction and association of two phases [68]. Regarding the oxide layer, gold is known as the noblest of the metals, typically forming unstable oxides [171, 173]. Therefore, in contrast to most metals [172, 174, 175], the presence of an oxide layer is not predominated on gold surfaces [173,

176]. In electrolyte-controlled conditions in which an oxide layer is formed on the surface of gold electrodes, the final oxide layer is often described as very thin with thickness below 1 nm [171]. Additionally, Canning and colleagues have observed that oxygen does not adsorb into a gold surface [177]. Therefore, any interlayer formation would necessarily occur from the interface into the polymer phase, and the gold phase can be assumed as a constant solid material.

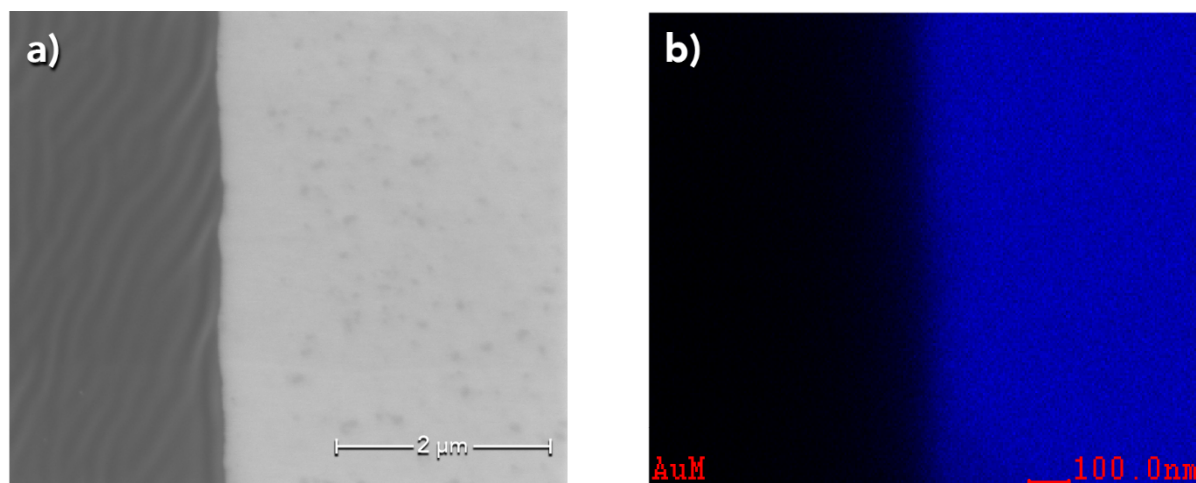


Figure 5.1: (a) SEM micrograph of a planar interface between bulk gold and epoxy showing a sharp boundary between the phases. (b) Gold elemental mapping from in-situ EDS showing the sharp distribution of gold in blue and no diffusion into the epoxy phase.

The interaction and association with gold were investigated using chemical analysis. The adsorption of gold element into the epoxy phase was examined in a planar interface. The SEM image in Figure 5.1 (a) shows a sharp interface between bulk gold in bright colour and the embedded epoxy in grey. At this observed interfacial region, an in-situ EDS spectrometer using an elemental mapping feature was used to observe the gold element distribution. The gold mapping in blue presented in Figure 5.1 (b) shows a sharp interface, at least at this scale. The few blue pixels in the polymer phase do not necessarily imply gold diffusing toward the polymer phase. Instead, this can be associated with the limit of the measurement resolution.

A second approach to evaluate the interfacial region utilized in this work consisted of imaging the interface with a transmission microscope at very high magnifications. This method was explored by Putz et al. to investigate the interlayers as thin as a couple of nanometres between metal and polymer systems [68, 178]. In this study, inspiration was taken from Putz et al. [68] to investigate the interface formed between gold and epoxy. The methodology developed to fabricate for the first time FIB milled lamellae from NPG-epoxy composites is explained in Section 3.2.2.

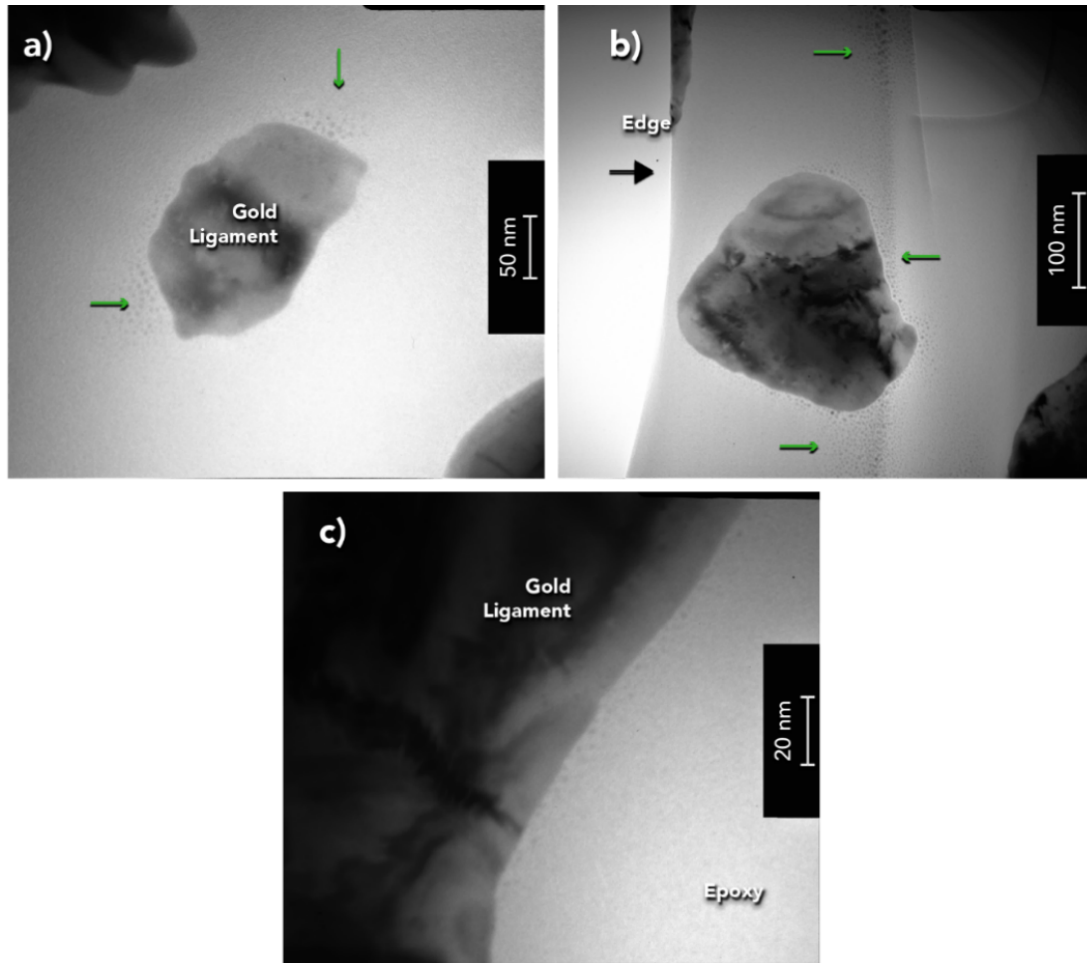


Figure 5.2: (a) and (b) show TEM micrographs of Au-ligaments embedded in epoxy. The black arrows indicate the edge of the lamella, and consequently, the edge of the epoxy phase. The green arrows indicate the epoxy's degradation due to the interaction with the high voltage electron beam. (c) shows at higher magnification the boundary between the two phases in which no interlayer can be observed.

The TEM images presented in Figure 5.2 (a) and (b) show the cross-section of two ligaments embedded in the epoxy. The gold phase appears in dark colours, and the epoxy surrounds the ligaments. In Figure 5.2 (b) is possible to observe the edge of the lamellae, which is indicated by a black arrow. Additionally, green arrows indicate small bubbles-like shapes observed near the Au-ligaments and on the edge of the lamella. It was observed that these features originated from the degradation of the epoxy by the high voltage electron beam, which is a well know artefact of the TEM imaging polymer [179, 180]. Not surprisingly, it was observed that the intensity of the degradation increased by increasing the exposure time and the voltage of the beam. A closer look at higher magnification into the very boundary between the two phases is shown in Figure 5.2 (c). No interlayer can be observed between the Au ligament and the epoxy phase, and the interface appears as a sharp boundary. The interlayers reported in the literature have a thickness extending from couples to hundreds of nanometres [172, 174, 175, 181], and consequently, they would be visible at the analysed length-scale.

5.2 Local mechanical response near a planar interface

Although it was found no evidence supporting the presence of an interlayer, the mechanical response near an interface between gold and epoxy is still an open question. Therefore, a series of nanoindentations were carried out in a line crossing a planar interface to reveal the local transitional property between the two phases. Nanoindentation technique is often used as a reliable method to measure the mechanical response from small volumes [139], which was essential to combine adequate spatial resolution and reliable mechanical property measurements. The geometry and morphology of the interfacial region play an essential role in the local properties. As discussed in Section 3.1.3, a sharp perpendicular boundary is unlikely due to the Au ligaments' morphology in the NPG-epoxy composite. Therefore, the planar interface selected in this study with a 45° inclination is a simplified sample model for the composite structure that allows for a systematic study. In these samples, the gold phase decreases in thickness with the proximity to the interface, as shown in Figure 5.3. The arrows indicate the nanoindentation line and the increasing thickness of gold under it. Thus, the gold thickness is a factor of the distance to the boundary and the phases inclination. In this section, the indentation line parameters are optimized first separately in the bulk materials, and then their impact is evaluated on the measured transitional response.

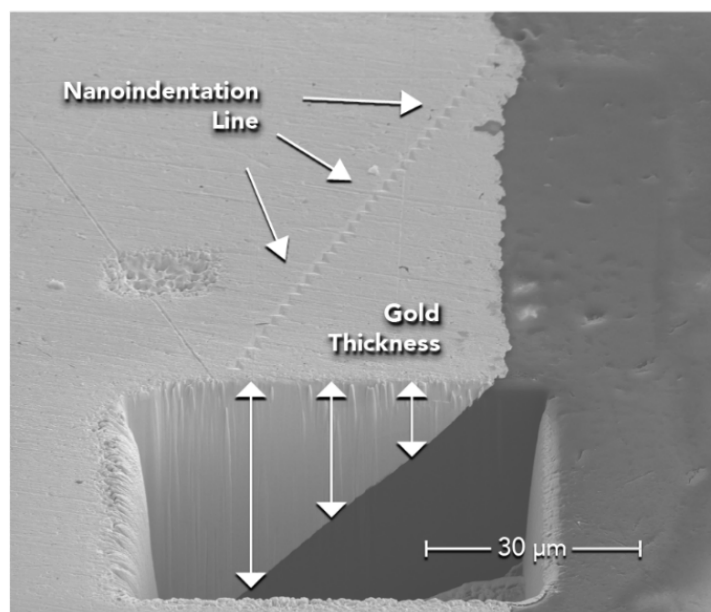


Figure 5.3: Schematic showing a SEM picture on an inclined interface between a planar gold-epoxy sample, in which FIB was used to mill a cross-section. The 45° inclination between the phases results in a decreasing gold thickness with the proximity to the interface. The arrows indicate a line of nanoindentations crossing the interface and the decreasing gold thickness with the proximity to the interface.

5.2.1 Line of indentations on the bulk materials

This section focuses on optimizing the parameters for the indentation lines performed first separately on each bulk material. The objective was to develop a single indentation protocol capable of a satisfactory spatial resolution in the line direction combined with a suitable reproducibility among the measured values in both materials. Although small indentations would allow for a higher number of measurements per length, the small volumes tested in shallow indentations are more sensitive to noise (uncontrolled variations on the experiment). A second possibility was to reduce the spacing between the indentations. Often the spacing is defined relatively to the indentation depth, and according to the material, the spacing between the indentations as large as 20 times the indentation depth should be utilized [182]. Questions regarding the interaction between indentation depth and spacing among indentation and the difference in behaviours between the indentations performed in gold and epoxy reinforce the necessity for a detailed investigation.

An experimental analysis was designed considering two factors: indentation depth and spacing among the indentations. Figure 5.4 shows the sample tree illustrating a crossed experiment with eight repetitions for each configuration. Here, the indentation depth was investigated in 3 levels: 100, 200, and 300 nm. Additionally, four spacing levels between the indentation were evaluated: 5, 7, 10, and 15 times the indentation depth. Although a small spacing could result in overlapping of the indentation plastic zones and even overlapping of the contact areas, these configurations were investigated as an alternative to increasing the spatial resolution of the indentation lines. Thus, for a reliable characterization of a material, the indentations should not impact one another.

The hardness and modulus results from 192 indentations separated by each material are presented in Figure 5.5, in which the colours represent the different indentation depths within each investigated level of spacing. In this experiment, 12 indentation protocols are evaluated as the combination of the two investigated factors. The bars represent an average of 8 measurements within each treatment, and the error bars indicate one standard deviation about the mean value. A two-way analysis of variance (ANOVA) was performed to analyse the data presented in Figure 5.5. This statistical hypothesis test is often used in quantitative outcome experiments with two categorical explanatory variables [183, 184]. In this case, the considered variables were the indentation depth and spacing among indentations. ANOVA analysis allows testing the significance of the main effect of the factors and the interaction between them, which calculates a separated probability value (p-value) for each factor and their interaction. The definition of the p-value is the probability of obtaining outcomes as extremes as the ones observed, assuming a correct null hypothesis (no relationship between the measured effects and the tested factors). Typically, a p-value smaller than 0.05 indicates strong evidence favouring the alternative hypothesis (an existing relationship between the measured effects and the tested factors).

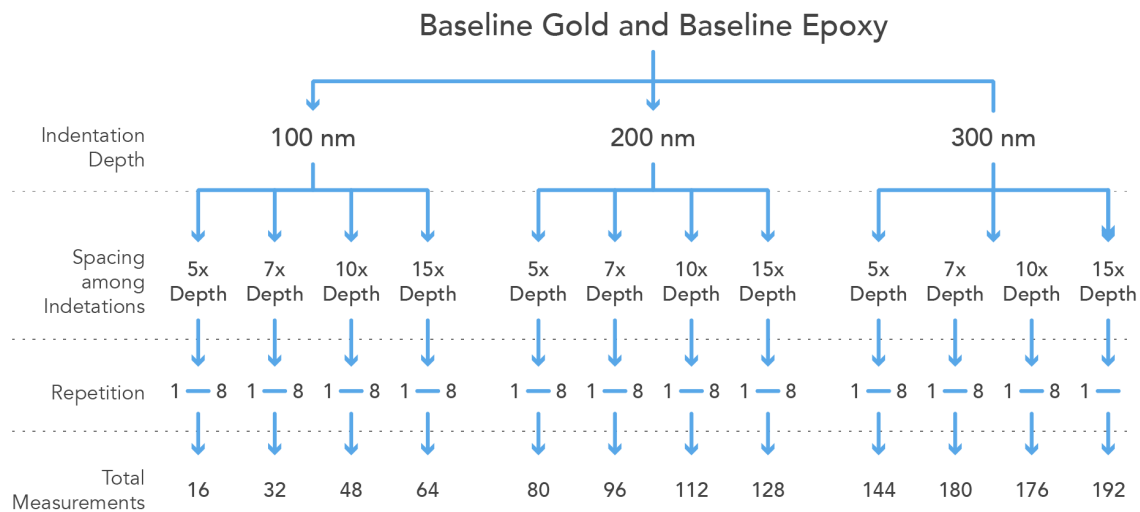


Figure 5.4: Sample tree designed to study the optimization of the indentation lines parameters, evaluating two factors: indentation depth and spacing among indentations. The levels for the indentation depth are 100, 200, and 300 nm. The spacing levels are 5, 7, 10, and 15 times the indentation depth. The same experimental investigation was conducted in bulk gold and epoxy.

The ANOVA analyses and p-value calculations here presented were conducted on the data analysis tools from MS Excel. Moreover, a significance level (α) of 0.05 and 8 replications for each treatment were considered. The p-values of the two factors and their interaction regarding hardness and modulus analyses are plotted in Figure 5.6 separately for each material. Since only the p-values from the factor indentation depth are below 0.05, it is assumed that only this factor has a statistically relevant effect on the measured values in this experiment. Thus, the initial concern about the interaction between the factors can be disregarded. On the other hand, the confirmation of the indentation depth's impact on the measured results was expected due to indentation size effects.

Although the ANOVA analysis indicated the indentation depth as the only statistically significant factor affecting the results, this does not guarantee a low spread of the data within the measurements carried out under the same indentation depth. Selecting an indentation line configuration that presents a low spread of the data within the same material is critical to attribute a property variation to the proximity to the interface. The spread of the data from an experiment can be directly analysed by the coefficient of variance, which is the ratio between the standard deviation, σ , over the mean values, \bar{x} . Therefore, the coefficient of variance for each testing protocol was plotted in Figure 5.7 for each level of the statistically significant factor (indentation depth), each material, and separately for the hardness and modulus results.

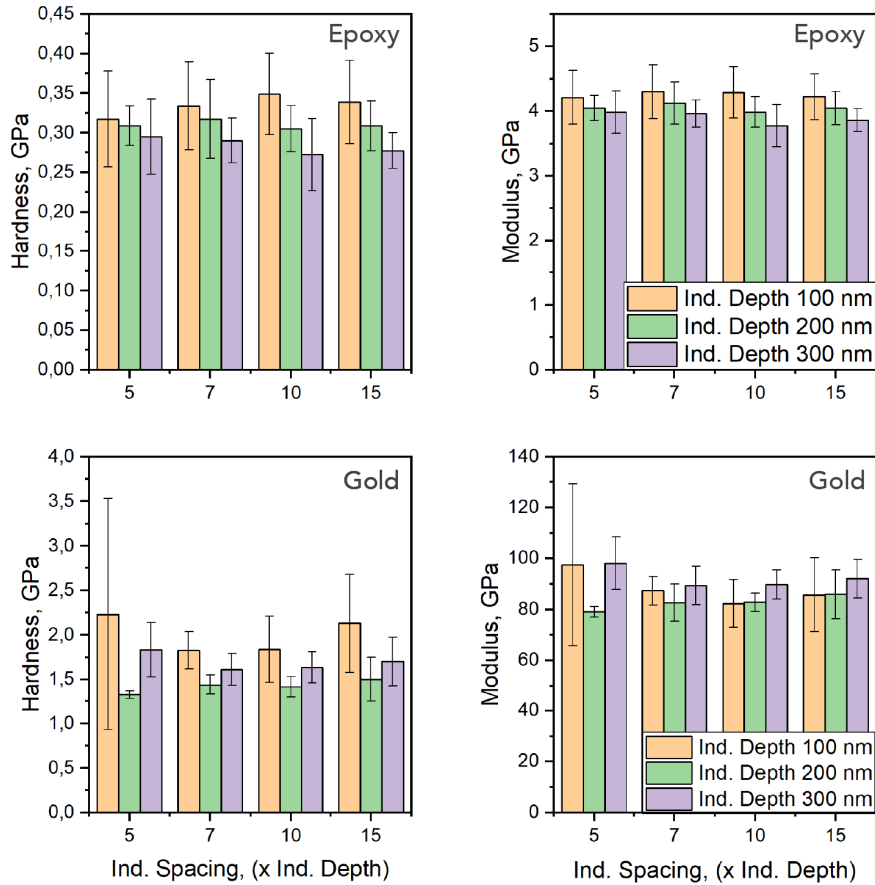


Figure 5.5: Results for the nanoindentations in line carried out in gold and epoxy samples evaluating the effect of two factors: indentation depth and spacing between the indentations. Each bar represents the average result of 8 measurements performed for each treatment, and the error bars indicate one standard deviation about the mean value.

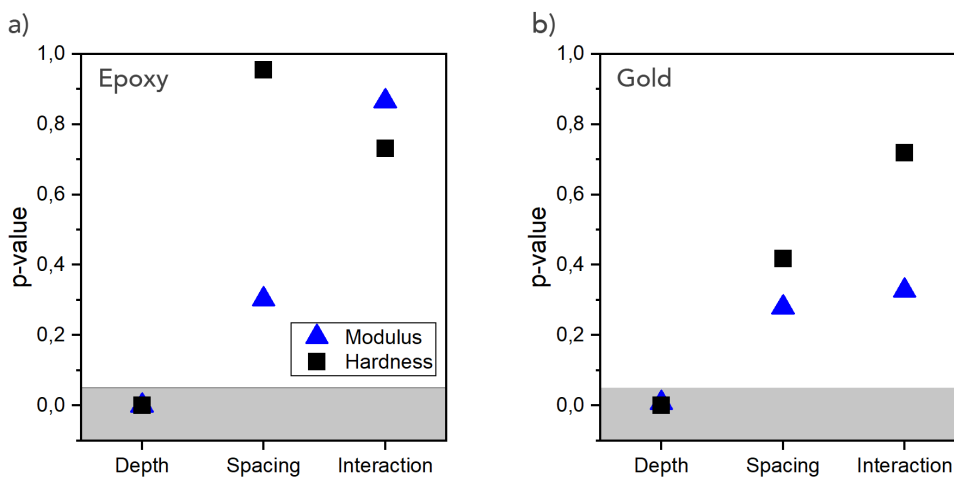


Figure 5.6: The plots present the p-values on the hypothesis testing for the effects of two factors (indentation depth and spacing among the indentations) and the interaction between them for the modulus in blue and hardness in black separated by the two materials. A p-value ≤ 0.05 indicates strong evidence against the null hypothesis.

The analysis presented in Figure 5.7 showed a broader spread in the data, i.e., a larger coefficient of variance, in the hardness results than the modulus ones. In the epoxy, the average of all coefficients of variance in hardness was 0.13, while in the modulus, it was 0.07. Similarly, the average values were 0.17 and 0.1 for hardness and modulus in gold, respectively. The relative higher coefficient in the hardness can be attributed to the size difference between the plastic and elastic zones in nanoindentation experiments [185, 186]. Since the elastic zone is bigger than the plastic zone, the effect of any local artefact is diluted in the larger volume of analysis, which can contribute to a smaller spread of measurements. On the other hand, the plastic zone is more susceptible to the local variation due to the comparatively smaller size. Additionally, the comparison within the levels of indentation depth showed that the indentation performed at 100 nm presented the spread of the data twice as high as the other indentation depths. This again indicates the more susceptibility of shallow indentation to localized phenomena.

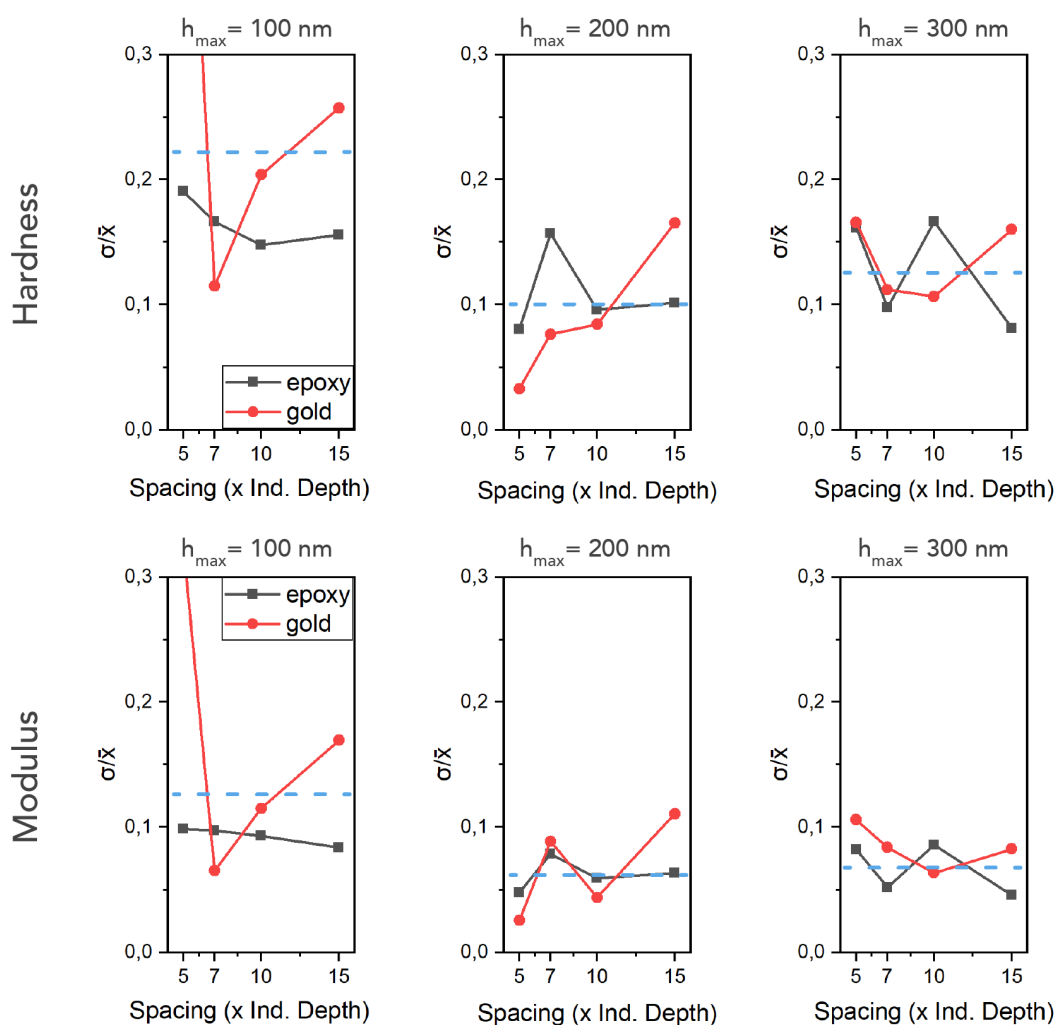


Figure 5.7: Coefficient of variance plotted for each level of indentation spacing separated by the indentation depths. The spacing levels among indentations are relative to the indentation depth, and the colours represent the results for the gold in red and black for the epoxy. The dotted line shows the average of all data within each plot.

In summary, the ANOVA analyses showed that varying indentation depth would affect the measured properties. For this reason, experiments in which the line of indentation crosses the interface must consider the depth of the carried-out indentation. The analysis of the coefficient of variance showed within the indentation depth levels the configuration with a smaller spread of results. Therefore, two indentation protocols from the indentation depth with a smaller spread were selected to continue the experiments crossing the interface: 200 nm deep and spacing of 5 times the indentation depth, and 300 nm deep and spacing 7 times the indentation depth. The abbreviation used for each protocol is D200S5 and D300S7, respectively.

5.2.2 Properties crossing an inclined interface

This section focuses on measuring the transitional properties of a gold-epoxy inclined interface by carrying out series of nanoindentations inline using the indentation configuration developed in the previous section. The plastic deformation created during a nanoindentation experiment generates dislocation that affects the local dislocation density, altering the response of a subsequent nearby indentation. In the previous section, the ANOVA analysis showed that this effect was not significant on the indentation lines performed in bulk gold. Nevertheless, the inclined interface's geometry leads to a reduced volume of gold at the very boundary, which can potentially increase the local dislocation density. Questions regarding the effect of the dislocation density on the measured properties near the interface are addressed here by varying the indentation line's direction.

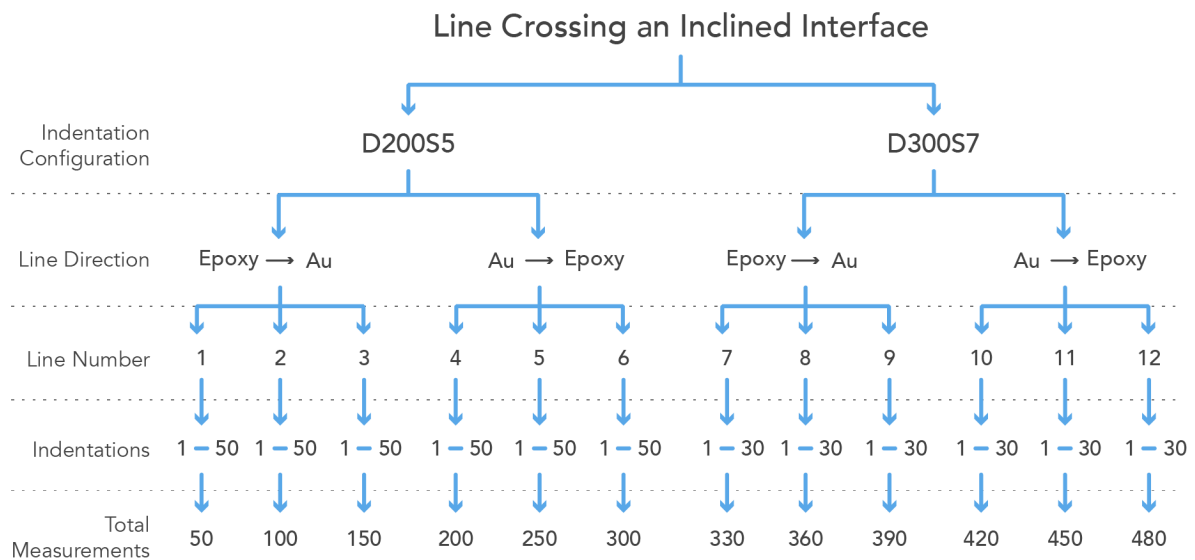


Figure 5.8: Sample tree designed to evaluate the transitional properties in an inclined gold-epoxy interface.

The test protocols D200S5 and D300S7 were utilized on the nanoindentation lines, and two line directions were tested: gold into epoxy and epoxy into gold.

Whenever a line starts in the gold phase, every subsequent indentation may influence the dislocations generated by previous indentations. At the interface, where the inclined geometry reduces the gold volume, this artefact might be increased, affecting the local mechanical response. Nevertheless, lines starting on the epoxy phase would prevent this dislocation/deformation effect toward the crossing of the interface. Therefore, an experiment was designed to address this issue and measure the transitional properties of an inclined gold-epoxy interface, in which the sample tree is represented schematically in Figure 5.8. In addition to the line direction, two configurations of indentations are tested, as follow

- D200S5: 200 nm of indentation depth and spacing of 5 times the indentation depth
- D300S7: 300 nm of indentation depth and spacing of 7 times the indentation depth

A total of 50 and 30 nanoindentations were carried out for each line of the D200S5 and D300S7 test protocol, respectively. The lines were performed 60° relative to the interface, which allowed for more measurements near the interface, increasing the spatial resolution comparing to a line perpendicular to the interface.

The local transitional mechanical response for the 12 lines separated by the nanoindentation treatments is presented in Figure 5.9 concerning hardness and modulus results and the distance to the interfaces. Red and blue colours represent lines starting in the gold and epoxy phases, respectively. The hardness response transitions from an expected bulk epoxy property in both tested indentation treatments. Nevertheless, the local modulus response did not reach the expected values for bulk gold. The local modulus response goes from the bulk epoxy into a slope that does not reach a plateau, as observed in the hardness response. Thus, this could be evidence that the lines were not long enough on the gold side. Regarding the line directions, the overlapping of red and blue lines indicates no difference near the interface for lines starting in the gold or the epoxy phase. Therefore, no evidence was found supporting the idea of pre-existing dislocations near the interface affecting the results of the nanoindentation line experiment for the tested length-scale.

Finally, the effect of the nanoindentation treatments on the measured transitional property was evaluated for the hardness and modulus responses. The data presented in Figure 5.10 shows the average of six lines and their corresponded standard deviation for each nanoindentation treatments. In terms of hardness response (Figure 5.10 (a)), a clear distinction can be observed on the gold side in which the D200S5 treatment reached higher values. This behaviour can be explained by the indentation size effect in gold, which presented strengthening as shallow indentation depths. Since the gold size effect is related to the plasticity of the material, the elastic response should not be affected. The results for the modulus response in Figure 5.10 (b) point also in this direction, showing no difference in terms of modulus response for the two tested nanoindentation treatments.

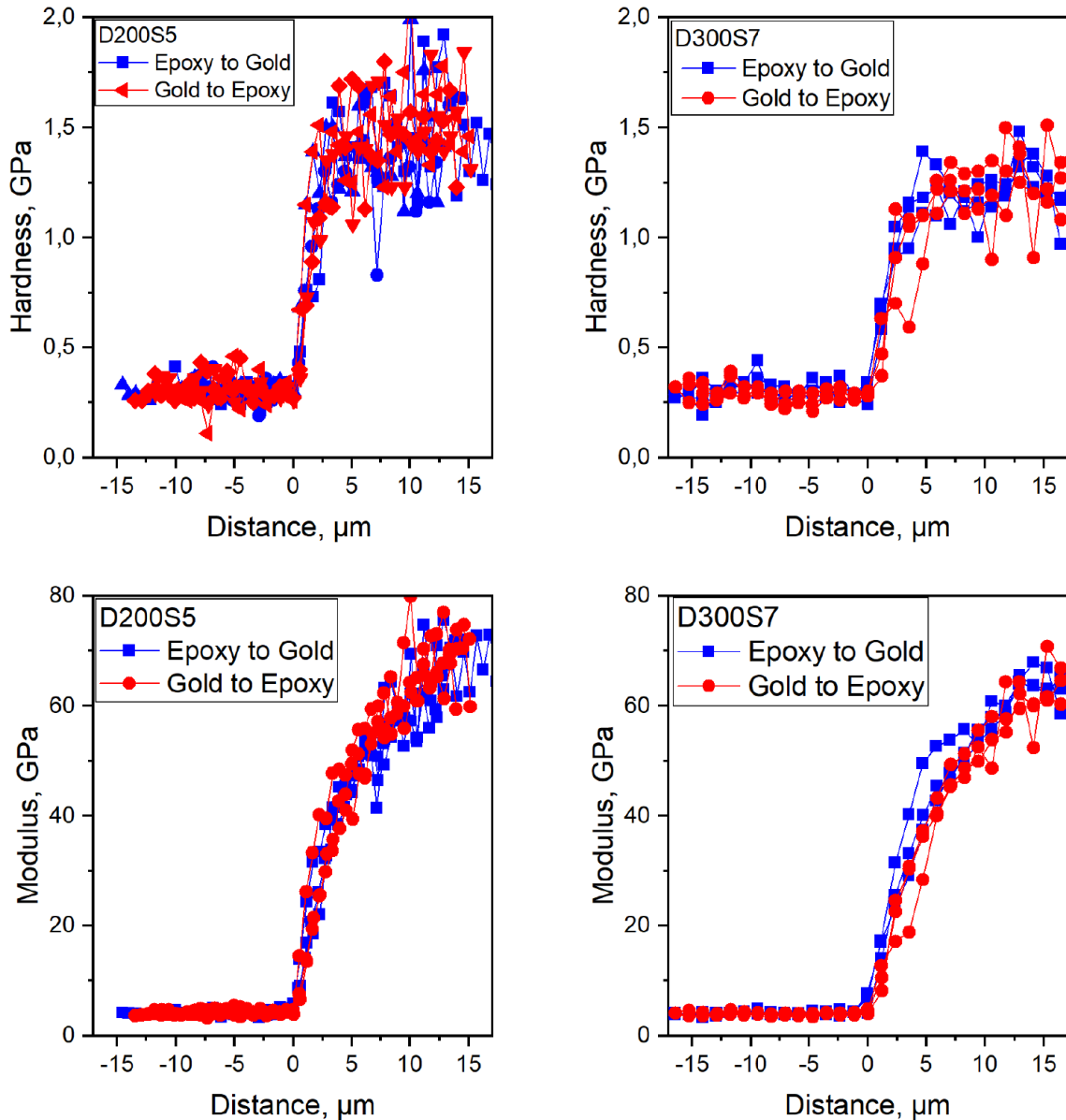


Figure 5.9: The four plots present the result from nanoindentation experiments performed in lines crossing an inclined gold-epoxy interface, in which 0 is the interface, and the positive values represent going toward the gold phase. The nanoindentation protocols are presented in separated plots, and the colours red and blue represent the lines starting in the gold and the epoxy phase, respectively. Three indentation lines were performed for each configuration.

In summary, no evidence was found that the direction of the lines plays a role in measuring the transitional properties on a gold-epoxy inclined interface. Additionally, 15 μm into the gold phase was enough to reach a plateau for bulk properties on hardness but not on the modulus, which indicates that a long line could be needed. Finally, the nanoindentation configuration can alter the transitional properties once the measurements are susceptible to depth-dependent responses. Nevertheless, even the D300S7 indentation protocol had 40% fewer indentations per line, and the same transitional behaviour could be observed in both configurations.

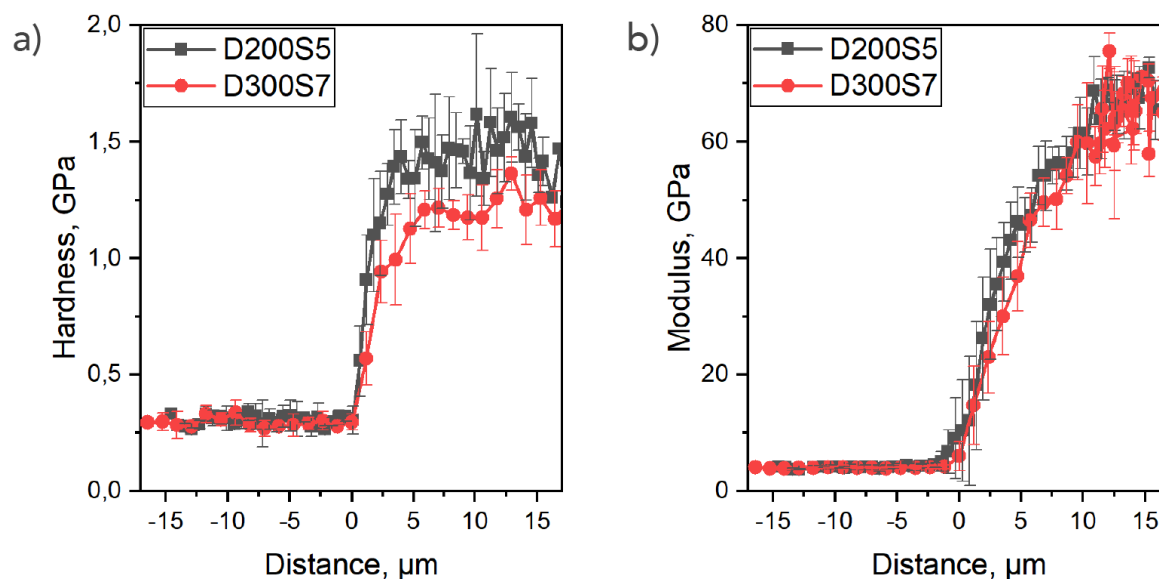


Figure 5.10: The two plots show the average of the transitional response for hardness (a) and modulus (b) crossing an inclined gold-epoxy interface. 0 is the interface, and the positive values represent going toward the gold phase. Each data point represents the mean of 6 measurements, and the error bar represents one standard deviation about the mean value.

5.2.3 Analysis of the transitional properties

This section aims to identify evidence of local mechanical response disturbances due to the interface. Therefore, the nanoindentation lines' transitional response was analysed separately into two parts: interface into epoxy and interface into gold. First, the analysis of the properties from the interface into the epoxy is presented. Figure 5.11 shows the results for eight nanoindentation lines, in which 0 is the interface. The negative values for distance mean moving away into the polymeric phase, consistent with the results presented in the last section. The solid grey lines represent the mean values for hardness and modulus measured in Section 5.2.1 for the D300S7 nanoindentation treatment. Additionally, the dotted lines represent three standard deviations about the mean values. Assuming that nanoindentation results follow a normal distribution, it is expected that 99.7% of the data spread to be contained within the dotted lines. As it can be observed, no trend could be identified on the results presented in Figure 5.11 on either the hardness or modulus responses.

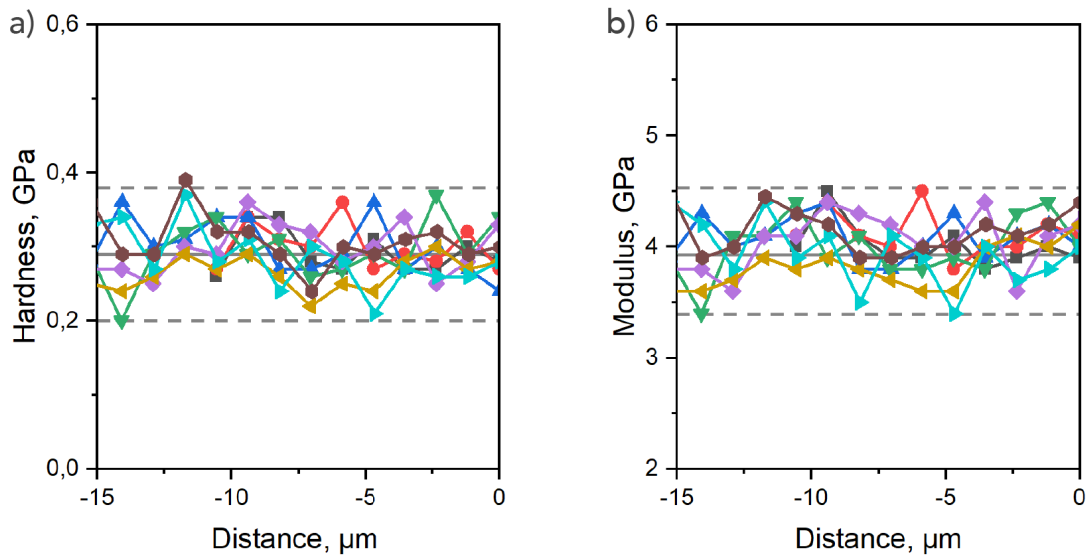


Figure 5.11: The two plots present the hardness and modulus response from the interface (0 distance) into the epoxy phase (negative values). A different colour represents each one of the eight nanoindentation lines. The solid grey lines represent the mean values for hardness and modulus found in Section 5.2.1 for the utilized nanoindentation parameters, and the dotted lines represent three standard deviations about the mean value.

Furthermore, the spread of data for all the lines was within the expected values for a normal distribution, which indicates no significant factor acting in the results. Thus, the data could not be differentiated from the spread of results in the bulk response. Therefore, for the length-scale tested in this investigation, no evidence of the interface influencing the local mechanical response on the vicinity of the interface into the epoxy side could be found.

Moreover, the analysis of the properties from the interface into the gold is presented. The transitional responses for two long lines of nanoindentation are presented in Figure 5.12, in which 0 is the interface, and the positive values mean moving away into the gold phase. Again, the solid grey lines represent the mean values for hardness and modulus measured in Section 5.2.1 for the D300S7 nanoindentation protocol, and the dotted lines represent three standard deviations about the mean values. It is possible to observe that the hardness response quickly reaches the bulk values of gold, and then the data spreads within the expected values considering a normal distribution in a bulk material. Concerning the modulus response, 80 μm into gold was enough to reach bulk values, but the transitional is less steep than the hardness response. Nevertheless, 80 μm is a very long distance for the interface to be influencing the mechanical properties, which motivated the analysis to consider a second possibility.

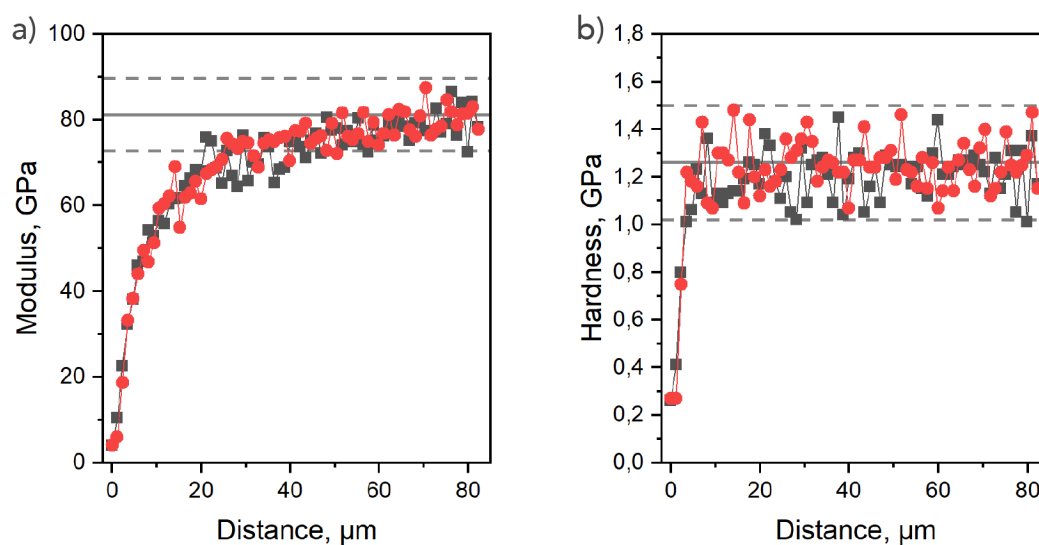


Figure 5.12: The two plots present the hardness and modulus response from two long nanoindentation lines, in which the interface is in 0 distance, and moving into the gold phase leads to positive values. The solid grey lines represent the mean values for hardness and modulus found in Section 5.2.1 for the utilized nanoindentation parameters, and the dotted lines represent three standard deviations about the mean value.

The inclined interface shown in Figure 5.3 shows that moving away from the interface increases the distance to the epoxy boundary and increases the thickness of gold under the nanoindentation. The influence of a decreasing gold thickness on the transitional property is unclear. Therefore, inspiration was taken from the approach used on thin films over soft substrates to analyse nanoindentation properties on the gold phase over epoxy in inclined interfaces. In this case, the gold phase would be considered a film over a soft substrate made of epoxy, and the film thickness decreases with the proximity to the interface.

The mean hardness response of 8 lines and the error bar representing one standard deviation is presented in Figure 5.13 to the gold thickness under the indentations. The solid grey lines represent the mean values for hardness measured in Section 5.2.1 for the D300S7 nanoindentation configuration, and the dotted lines represent three standard deviations about the mean values. It can be observed that the hardness reached the expected bulk values of gold whenever the gold thickness is about ten times the indentation depth. Typically, nanoindentation measurements are performed in indentation depth not greater than 10% of the film thickness to avoid the influence of the substrate [187–189]. The results presented in Figure 5.13 point to the same behaviour, suggesting the gold thickness is governing the transition of the hardness.

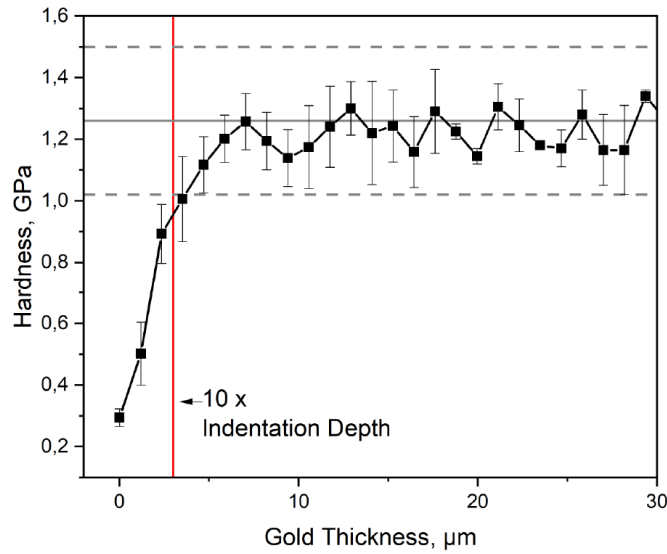


Figure 5.13: Hardness response to an increasing gold thickness resulted from nanoindentation lines performed in inclined interfaces. Each data point represents an average of 8 points, and the error bar is one standard deviation about the mean. The red line shows the point at which the gold thickness reaches ten times the indentation depth. The solid grey line represents the mean values for hardness found in Section 5.2.1 for the utilized nanoindentation parameters, and the dotted lines represent three standard deviations about the mean value.

The measurement of the elastic modulus in a thin film over soft substrates has been the subject of investigations for the last 30 years. Doerner and Nix first proposed an empirical model based on the offsetting of the indenter deformation to determine the elastic modulus presented in Equation 3.6. The model introduced weighting factors to the influence of the film and substrate and considered the film thickness and effective depth of the indentation [190]. Moreover, the work done by King [191] and then a second work from Saha-Nix [192] expanded the empirical model first developed by Doerner and Nix in order to uncouple from the measured reduced modulus E_r the contributions of the indenter, film, and substrate. Nowadays, Saha-Nix model is the typical approach utilized concerning investigations of the elastic properties in thin-film substrates system. The governing equation is:

$$\frac{1}{E_r} = \frac{1 - \nu_i^2}{E_i} + \frac{1 - \nu_f^2}{E_f} \left(1 - e^{-\frac{\alpha(t_f - h)}{a}} \right) + \frac{1 - \nu_s^2}{E_s} \left(e^{-\frac{\alpha(t_f - h)}{a}} \right) \quad (5.1)$$

where the subscripts i , f and s refer to the indenter, film and substrate properties. Additionally, a , t_f and h are the square root of the projected contact area, the film's thickness, and the indentation depth, respectively. Finally, α is a numerically determined scaling parameter which is a function of a/t .

Table 5.1: Evolution of the weighting factors on the analysis of the elastic response in thin-film over soft substrates and the proposed weighting factor concerning inclined interfaces.

Doerner-Nix Model [190]	King Model [191]	Saha-Nix Model [192]	Proposed Model
$e^{-\frac{at_f}{h}}$	$e^{-\frac{at_f}{a}}$	$e^{-\frac{\alpha(t_f-h)}{a}}$	$e^{-\frac{\alpha \cdot 2 \cdot \ln(t_f-h)}{a}}$

The differences in a thin-film and an inclined interface sample motivated an adaptation on the weighting factors. Since a 45° inclined interface has only half of the gold phases a film would have, it is safe to expect that the local responses would be more complied considering the same thickness of gold. Therefore, an adjustment on the weighting factor was developed empirically, still using the same variable of previous models. The evolution of the weighting factor is shown in Table 5.1, and the proposed empirical model for analysing the inclined interface cases is:

$$\frac{1}{E_r} = \frac{1 - \nu_i^2}{E_i} + \frac{1 - \nu_f^2}{E_f} \left(1 - e^{-\frac{\alpha \cdot 2 \cdot \ln(t_f-h)}{a}} \right) + \frac{1 - \nu_s^2}{E_s} \left(e^{-\frac{\alpha \cdot 2 \cdot \ln(t_f-h)}{a}} \right) \quad (5.2)$$

Figure 5.14 shows the transition of the reduced modulus response from the interface into the gold phase in terms of the increasing gold thickness for experimental results (black), and the simulated values to King's model (red), Saha-Nix model (blue) and the proposed model (green). For the simulated values, the properties of the materials followed the characterized properties found in Section 5.2.1. The only difference among the models is the weighting factor that balances the contributions of film and substrate according to the film thickness. As shown in Figure 5.14, the models for thin-films present good agreement with the experimental results in the extremes of the evaluated gold thickness. The experimental results confirm that the inclined interfacial sample is more compliant than the simulated values for the thin-films. The proposed model captures the transitional behaviour of the inclined samples, as it does with the extreme cases of very thin and thick thicknesses. In summary, it was possible to predict the local properties on inclined interfacial samples based on the underlying thickness of the gold below the indentation by adjusting the weighting factors on a well-established thin-film model [192]. Therefore, the modulus and hardness analyses converge, indicating the gold thickness as the governing factor on the transition properties near a gold-epoxy inclined interface.

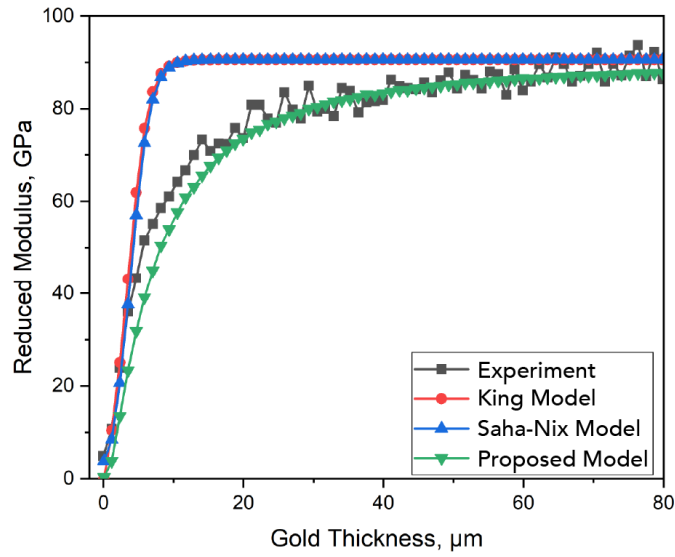


Figure 5.14: Reduced Modulus response to an increasing gold thickness measured experimentally (black) and simulated using King model (red), Saha-Nix model (blue), and the proposed model presented in Equation 5.2 (green).

5.3 Conclusions

In closing, no evidence was found supporting the presence of an interlayer between gold and epoxy. For the investigated length scales, both materials could still be assumed as a continuous solid with a sharp interface, which circumvents the implications of a geometrically undefined polymeric interphase. The measurement of the transitional properties in the interfacial region was challenging since the measurement system affected the mechanical response. Nevertheless, using statistical methods, a nanoindentation protocol was developed to ensure the reliability of the measured transitional response. No evidence was found supporting the interface affecting the transitional properties in an inclined interfacial sample. Also, measurements carried out in the polymer phase at the vicinity of the interface could not be differentiated from the bulk polymer ones. On the gold side, the hardness and modulus analyses converge, attributing the transitional response as an artefact governed by the gold's thickness.

The absence of an interlayer and the direct transition of bulk properties are fundamental characteristics of a gold-epoxy interface. Therefore, it is expected that the same findings found in the planar samples can be assumed to the NPG-polymer composites. Despite the difference in the constitutional length-scale and morphology, it is reasonable to assume no interlayer and the local mechanical response not being affected by the proximity to the interface.

6 The effect of the interfacial strength

In this chapter, the interfacial strength is investigated in a simplified sample model composed of the same constituent phases of an NPG-epoxy composite. The inclination between the phases was explored to evaluate the interfacial shear strength by compressing bi-material microcolumns. Here, the characteristic bonding strength between gold and epoxy at a small length-scale is measured, and the interfacial failure mode is presented. In addition to the micromechanical experiments themselves, this section presents the development of a finite element method to simulate the interfacial behaviour of a gold-epoxy contact. Based on the properties measured experimentally and the interfacial characteristic presented in Chapter 5, a surface-based cohesive behaviour model was employed. The comparison between the FEM simulations and experimental results is presented for the compression of bi-materials microcolumns. Additionally, the influence of the model's parameters (damage initiation and fracture energy) is evaluated in relation to the stress conditions at the interface.

6.1 Measuring the bonding strength between gold and epoxy

6.1.1 Failure mode identification

In this section, interfacial shear strength testing was utilized to evaluate the bonding between a two-material system. The approach developed by Chen and colleagues tested the shear strength of the Ti interlayer in a TiN/Ti/Si(100) sample [151]. Although this methodology was developed to evaluate the critical shear strength of thin interlayers between two phases and the results from Chapters 4 and 5 found no evidence regarding the presence of an interlayer between gold and epoxy, a similar experimental approach could be employed here to estimate the direct bonding between the two phases. Additionally, a micromechanical approach would probe extremely small interfacial areas compared with traditional macromechanical methods. Therefore,

the bonding strength measured would circumvent the contribution of the mechanical interlocking mechanism originated by macroscopic surface features. Assuming the fractal nature of a polymeric interphase, the mechanical anchoring acting in the experiments comes only from submicron features that resemble the smooth contact in a NPG-epoxy composite.

An example of the square cross-sectional microcolumns with an inclined gold-epoxy interface is shown in Figure 6.1 (a). The top part of the column is made of epoxy, while the bottom solid gold. It was found that this design provided a relatively small deformation of the substrate during the compression process in comparison to microcolumns with an epoxy substrate. Additionally, in microcolumns with gold on the top part, the small gold volume was prone to deform throughout slip band deformation, which unnecessarily complicated the analysis.

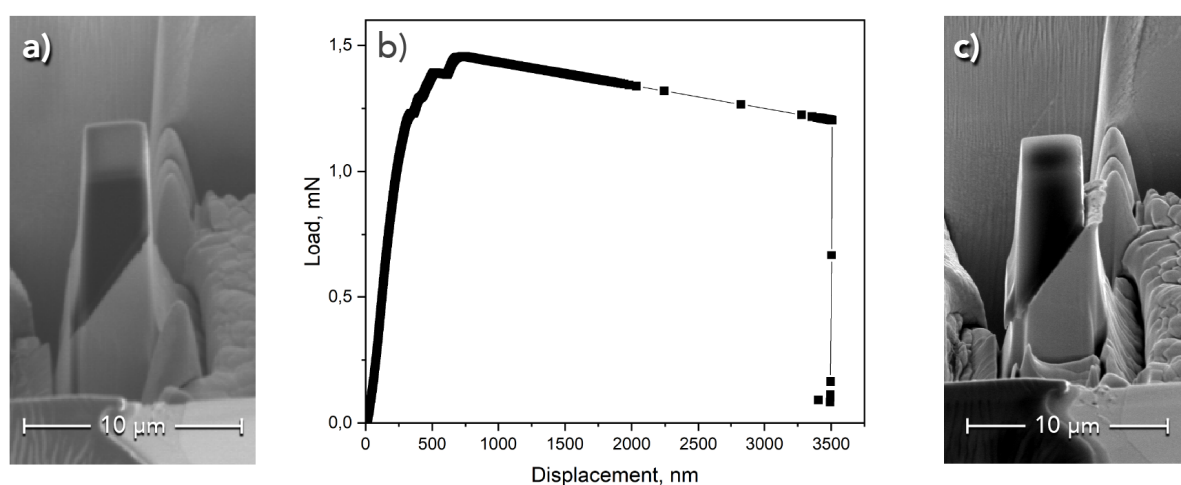


Figure 6.1: (a) SEM image showing a microcolumn milled in a planar model sample with an inclined interface with epoxy on the top and gold on the bottom. (b) load-displacement data for the same interfacial shear strength test. (c) the same microcolumn after the compression in which can be observed the collapse of the interface.

The representative curve presented in Figure 6.1 (b) shows the load-displacement response for microcompression, which testing protocols are described in Section 3.4.2. The overall behaviour is similar to the one reported by Chen on the shear strength testing of the Ti interlayer [188, 193]. The load reaches a peak and then displays a displacement burst attributed to the interfacial collapse. Furthermore, the SEM image of the aftermath of the microcompression confirmed the interfacial failure, and the top part of the microcolumn slid over the bottom part. Figure 6.1 (c) shows the microcolumn after the microcompression.

The interface strength has been calculated using the maximum load in previous works [151–154], which can be problematic since there is no evidence that the interfacial failure occurs entirely at the peak load. Here, a more reliable approach to identifying the interface's failure is proposed based on the loading stiffness response. The loading stiffness is the first derivative of

the load over the displacement, and it was calculated in this work as the slope of every five neighbour points in the loading segment of the load-displacement curve. Figure 6.2 shows the loading stiffness and the load over the displacement in red and black, respectively. The first inflexion point in the loading stiffness curve is typically associated with establishing full contact between the indenter tip and microcolumn. The subsequent multiple inflexions indicate a more complex yielding behaviour than fully dense epoxy microcolumns, which are later discussed. It is proposed here that the interface can be considered completely debonded at a critical displacement when the response starts being governed by the indenter spring. The critical displacement can be identified whenever the loading stiffness reaches the characteristic response of the spring constant from the nanoindenter equipment. The inset in Figure 6.2 shows a plateau being reached by the loading stiffness at the characteristic load spring constant of the nanoindenter instrument used in this work ($K_s = 91 \text{ N/m}$). In the approach developed in this work, the load at the beginning of the stiffness plateau was considered to calculate the interfacial strength. At this level, only the springs barres the applied load. Consequently, the displacements bursts in the load curve can be interpreted as an artefact of the measurement system, which should not be associated with the material's response. Further loading segments are likely related to localized deformation necessary to the sliding of the top part of the microcolumn.

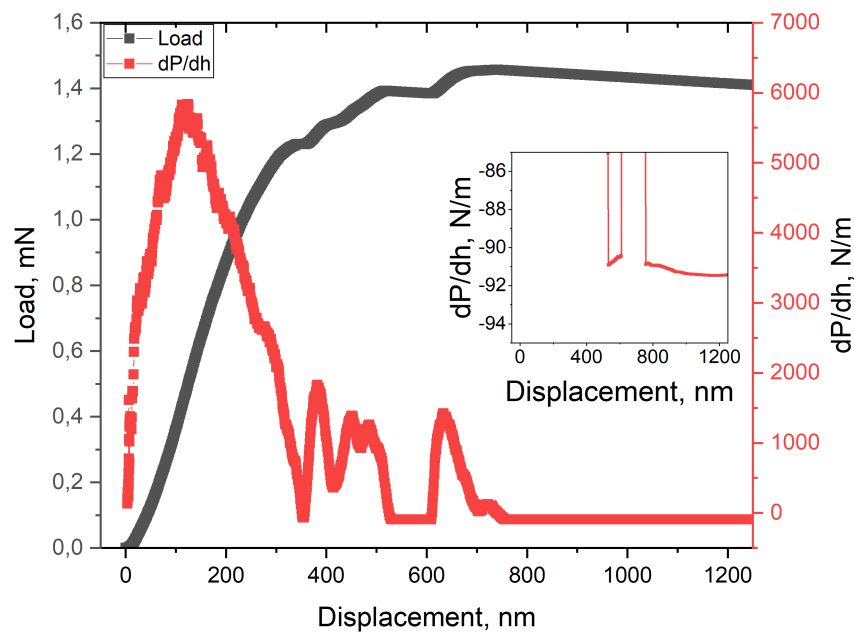


Figure 6.2: Load and loading stiffness per displacement for the test present in Figure 6.1. The loading stiffness during the displacement burst is shown in detail in the inset. The constant value can be associated with the spring constant of the nanoindenter equipment ($K_s = 91 \text{ N/m}$).

The microcompression of fully dense gold and epoxy microcolumns allows for identifying each constituent phase's failure mechanics. The details of the microcompression testing protocol are described in Section 3.4.2. Figure 6.3 shows a diagram compiling the mechanic response and

SEM pictures of the compressed cylindrical microcolumn of gold (a), inclined interface (b), and epoxy (c). Additionally, the plots present the load, loading stiffness, and harmonic contact stiffness (HCS) versus displacement. The difference between the loading stiffness and the harmonic stiffness is that while the former gives the slope of the loading segment, the latter is related to the small dynamic oscillation of the CSM indentation mode.

Although the absolute values can not be correlated, the comparison of the mechanical responses revealed how the microcolumns withstood the applied load. Figure 6.3 (a) presents the microcompression results of a solid gold microcolumn. The loading segment starts whenever the flat punch indenter first established contact with the top of the microcolumn. Then, accommodation occurs, which alters the slope of the loading curve until full contact is established between the indenter tip and microcolumn. The reaching of a plateau in the HCS curve indicates establishing the full contact, and from that displacement forward, the microcompression data can be interpreted accurately as the materials property. The loading stiffness before the yielding display fluctuations that may relate to localized events. Moreover, the yielding is reached, and due to the size of the microcolumn, slip band activity occurs, which can be observed by the rapid drops on the HCS response. Although the plot only presents one slip activity, the deformed microcolumn presents the microcolumn further compressed in which multiple slip activities took place.

Figure 6.3 (c) presents the results for a solid epoxy microcolumn. After the HCS curve indicated the full contact between indenter and microcolumn, the HCS remains stable throughout the compression. The loading stiffness first increases and then decreases, indicating the start of yielding. The single inflexion point in the loading stiffness curve indicates that the epoxy column deformed as one, which was later confirmed by the SEM image showing the compressed microcolumn.

The microcolumn results containing an inclined interface between gold and epoxy are shown in Figure 6.3 (b). Once again, the full contact is indicated by the HCS curve, which remained in a plateau. Then, the lack of rapid drops on the HCS curve indicates the absence of slip activity in the gold part of the microcolumn. Not surprisingly, the first section of the loading stiffness curve is similar to the epoxy microcolumn response. Then, after the maximum point on the loading stiffness curve, the response fluctuates, resembling the response of the fully dense gold microcolumn. Nevertheless, no slip-band activity could be identified either on the HCS curve and after the compression by imaging the microcolumn. Instead, the loading stiffness drops and forms and plateaus in the level associated with the spring constant from the nanoindenter. Imaging the microcolumn after the compression confirmed the interface's failure, and consequently, the two parts were separated. In closing, the mechanical response of microcolumns with inclined interfaces combine the deformation response of both constituent phases, but the interfacial failure was activated here before the failure mechanism observed in the solid microcolumns.

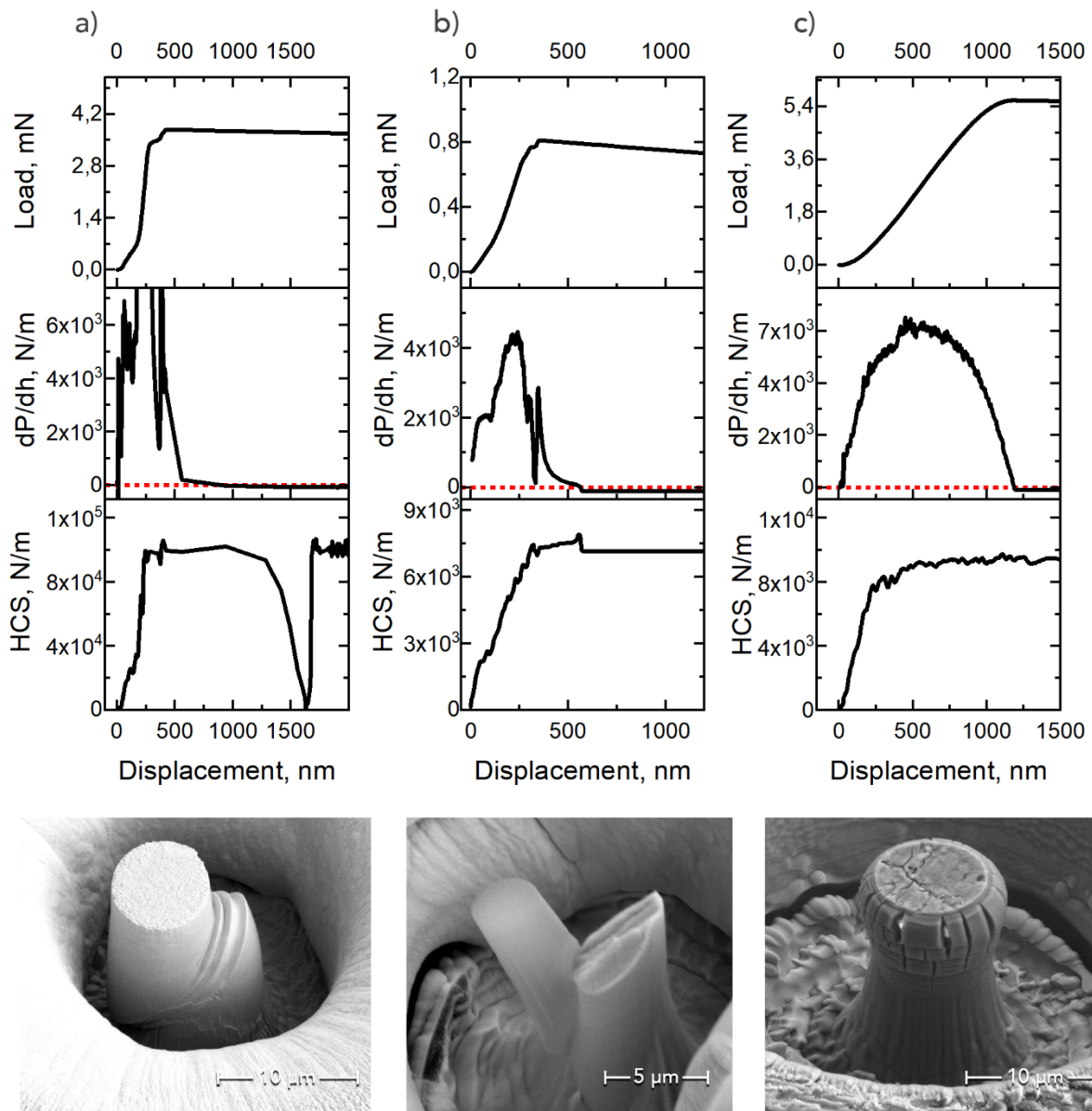


Figure 6.3: Figure 6.3: Microcompression of a gold (a), inclined gold-epoxy interface (b) and epoxy (c) microcolumns. The plots show the load, loading stiffness $\left(\frac{dP}{dh}\right)$ and harmonic contact stiffness (HCS) versus displacement from each microcolumn configuration. The SEM micrographs show the aftermath of the microcompression. In the bi-material microcolumn in (b), the response displays the deformation characteristics from the solid microcolumns, but the interface collapsed before the activation of other failure mechanisms.

6.1.2 Interfacial shear strength

In this section, the interfacial shear strength method is used to measure the characteristic bonding strength between gold and epoxy and to investigate the sensitivity of the measured strength to the size of the analysed interfacial area. Figure 6.4 shows the mechanical response of 5 microcolumns with different interfacial areas but with the same inclination and proportion between the constituent phases. As shown in Figure 6.4 (a), the load-displacement behaviour shows increasing peak loads, which was expected due to the difference in size among the microcolumns. Nevertheless, all samples presented the characteristic displacement bursts after reaching the peak load, which is typical attributed to the interfacial collapse in interfacial shear strength testing.

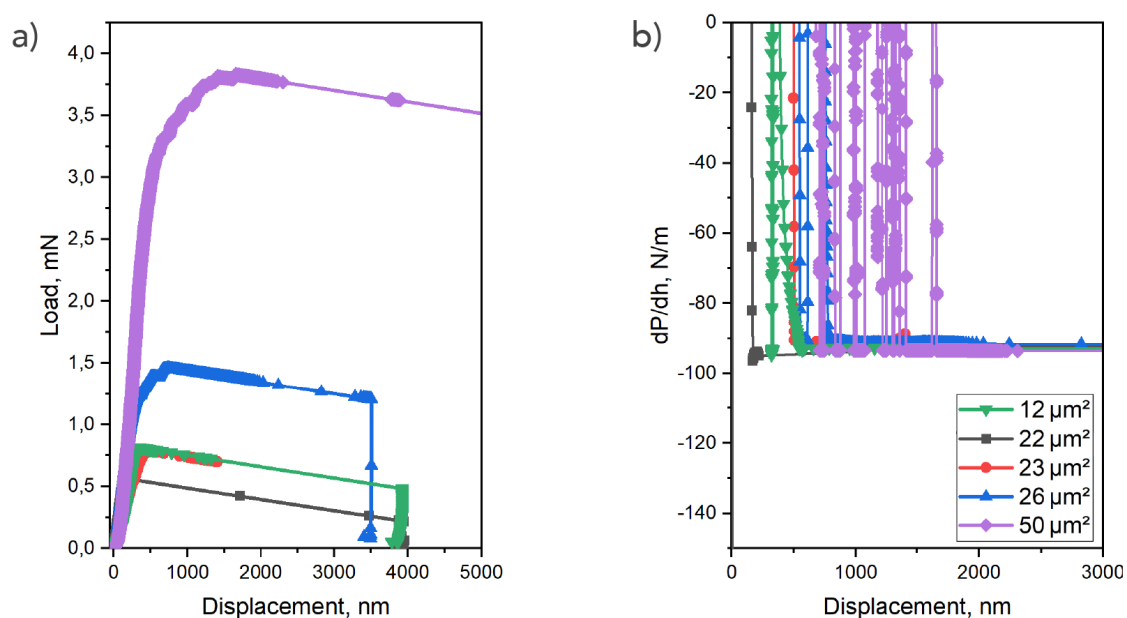


Figure 6.4: (a) Load-displacement response of 5 microcolumns with different interfacial areas submitted to interfacial shear strength testing between gold and epoxy. (b) the loading-stiffness response for the same microcolumns showing the plateaus in which the tests are governed by the indenter spring.

Moreover, the loading stiffness was used to identify the exact displacement associated with the interface collapsed, as described in the last section. Figure 6.4 (b) presents the loading stiffness response showing the characteristic plateau for all measurements. This behaviour indicates that all tested microcolumns had the same failure mechanism and that the indenter spring governed the mechanical responses. Nevertheless, reaching the spring constant can only be correlated with the end of the interfacial failure, and the determination of the beginning of the interfacial delamination remains complicated in an experimental approach. The subsequent rise and drops in the loading stiffness attributed to localized mechanical deformation during the slide of the top part of the interface are present independently of the microcolumn size. However, the number of cycles

varied considerably, with the larger microcolumn presenting a higher fluctuation. This can be explained readily since larger microcolumns can accommodate more localized deformation during the slide of the top part of the microcolumns.

The stress-strain curves presented in Figure 6.5 were obtained by calculating the shear stress in the 45° plane using Equation 3.20 and estimating the strain considering the microcolumns' total height. The critical displacement in which the interface collapsed found by the loading stiffness method is represented using dotted lines in the corresponded colour for each test. Then, the critical shear stresses were determined by the shear stress level crossing the dotted lines. It can be observed that the interfaces collapsed in shear levels close to 45 MPa for the microcolumns with interfacial area equal to 12, 26, and 50 μm^2 . No evidence pointing to the influence of the interfacial area could be found regarding the critical stress for the tested microcolumns, which agrees with resulting in the literature showing the lack of correlation between increasing interfacial area the interfacial fracture toughness [194]. Although the different sizes, the microcolumns behave similarly with interface collapsing in strain levels between 0.03 and 0.04. Here, it is necessary to differentiate the interface's collapse from the start of the sliding of the microcolumns. The sliding might imply further deformation, such as regions adjacent to the interface and regions due to the geometry tapering of the microcolumns. Thus, both can be influenced by the sample size. This could explain the further loading of the larger microcolumns after the interfacial failure. Finally, the responses of two other microcolumns (22 and 23 μm^2) contrast with the first three, reaching only a fraction of the first measured critical stress.

In addition to the mechanical responses, the microcolumns were imaged by SEM before and after the compression. Figure 6.6 shows the SEM micrographs of the two representative microcolumns before and after the microcompression. It can be observed that in the microcolumns, which presented a higher interfacial shear strength, the interface was perfectly bonded before the test, as seen in Figure 6.6 (a). On the other hand, the microcolumn showed in Figure 6.6 (b) presented apparent delamination before the compression took place. However, the mechanical response of this column shows evidence that the interface was bonded since the microcolumn was able to carry a considerable load before the peak load. Finally, the microcolumn's stiffness, which can be estimated by the slope of the loading segment in Figure 6.5, shows that the defects on the interface turned the microcolumn more compliant, which could be explained by a reduced area transferring the load from the epoxy into the bottom of the microcolumn.

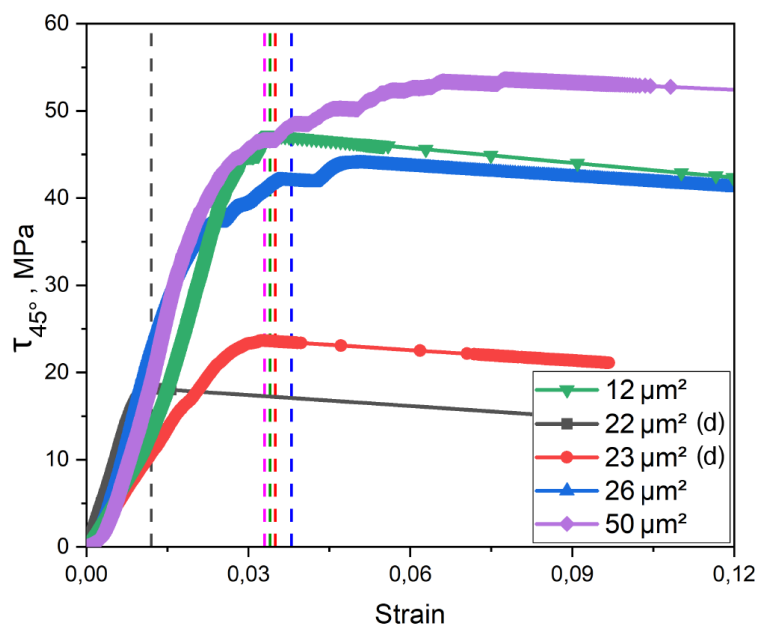


Figure 6.5: Shear stress in the 45° plane versus strain for five microcolumns with an inclined interface between gold and epoxy. Each line represents a microcolumn with a specific interfacial area. The microcolumns with 22 and 23 μm² presented defects on the interface observed by SEM before testing. The dotted lines for each corresponded colour indicate the exact strain in which the interface collapsed identified using the loading stiffness approach.

In addition to the fundamental bonding strength between a perfect bonded gold-epoxy sample, the results are presented here as experimental evidence of the influence of interfacial defects on the measured bonding strength. As presented in Chapter 2, the interface strength is a characteristic of a contact pair. Therefore, even that the microcolumns are composed of the same constituent phases, the surface's defect can drastically alter the measured critical shear stresses. A micromechanical approach allows for testing interfacial areas small enough that no visible flaw can be identified at a micron to submicron scale. In principle, these quasi-flawless interfaces should present higher bonding strength since they have a reduced influence on surface defects presented on a larger scale. Macromechanical method to evaluate the interfacial shear strength such as single lap joints and pull-out testing examine much larger interfacial areas, which are statistically more likely to present defects. Some typical critical shear stress values reported for these macromechanical approaches in a bi-materials interface with epoxy are 20 MPa to aluminium [195, 196], 12 MPa to steel [197] and 35 MPa to bronze [198]. Not surprisingly, these values are similar to those found in this investigation for the interface with defects rather than those that perfectly bond together.

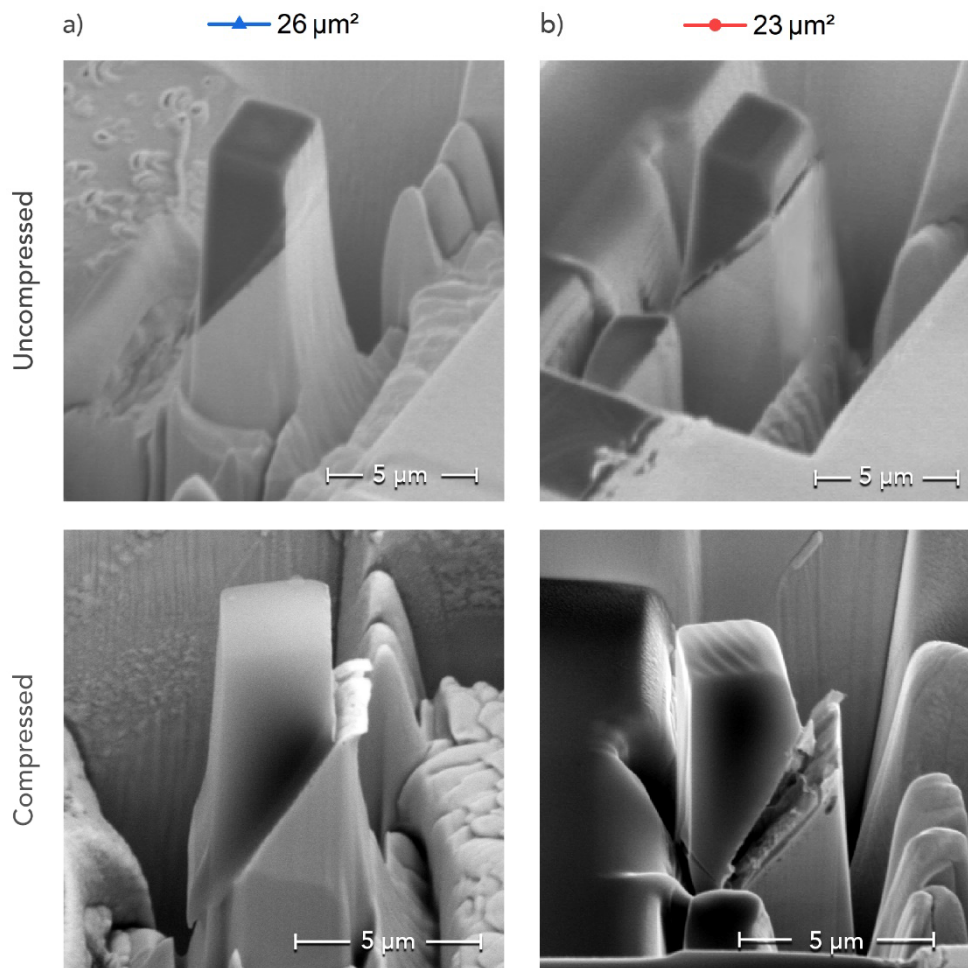


Figure 6.6: SEM micrographs showing the microcolumns before and after the interfacial shear strength test. The colour coding matches the respective data presented in Figure 6.5. While the microcolumn with $26 \mu\text{m}^2$ interfacial area presented before the test a perfectly bonded interface, the microcolumn with $23 \mu\text{m}^2$ displayed defects on the interface even before the compression.

6.2 Finite element method for a gold-epoxy interface

The interfaces modelled in this work follow a surface-based cohesive contact approach, primarily intended for cases in which the interfacial thickness is negligibly small [199–202]. The cohesive contact behaviour allows for interfaces initially in contact to separate due to an applied load. Thus, the established bonds may be damaged and fail due to a loading process. The same laws govern the cohesive contact as a cohesive element method. However, as a surface property, the calculations are done for each contact constraint, which is related to the number of nodes acting as slave nodes [203]. Although a small element size may be computationally demanding, this

method allows for localized interfacial behaviour, even for complex geometries. First, the contact state needs to be adequately defined between the contact pair. For the simulations in this work, no gap between the phases was considered. Then, the resolution of the method according to the loading process takes place. Its constitutive behaviour is detailed by a linear elastic traction-separation mode, damage initiation, and damage evolution laws [203]. Each one of these pieces is following described and are represented in Figure 6.7.

Abaqus assumes a linear elastic behaviour initially for the traction-separation model, in which tractions are defined as the nodal cohesive force divided by the contact surface area at each contact node [204]. The elastic response can be represented in terms of an elastic constitutive matrix that correlates the normal and shear stresses to the normal and shear separations across the interface. The nominal traction stress vector, \mathbf{t} , consists of three components t_n , t_s and t_t , where they represent the normal, first, and second orthogonal in-plane shear components of the traction vector, respectively, and are defined within the cohesive contact element coordinate system [203]. The corresponding separations are denoted by δ_n , δ_s , and δ_t , which are related to the tractions via the cohesive stiffness matrix, K . The elastic behaviour can then be written as:

$$\mathbf{t} = \begin{Bmatrix} t_n \\ t_s \\ t_t \end{Bmatrix} = \begin{bmatrix} K_{nn} & K_{ns} & K_{nt} \\ K_{ns} & K_{ss} & K_{st} \\ K_{nt} & K_{st} & K_{tt} \end{bmatrix} \begin{Bmatrix} \delta_n \\ \delta_s \\ \delta_t \end{Bmatrix} = K \delta \quad (6.1)$$

In this work, elastic isotropy was assumed for the interfacial stiffness. Therefore, the contact enforces the interfacial stiffness independent of the direction. Also, a penalty stiffness is set against contact penetration following Abaqus' default of ten times the underlying element stiffness.

Damage initiation and evolution need to be defined to describe the criteria in which the bond fails and the subsequent stiffness reduction during failure propagation. The damage initiation criteria set the starting of the degradation on the cohesive interaction at a contact pair. In this study, a maximum stress criterion is used to define the damage initiation. It assumes that damage initiates whenever a prescribed maximum contact stress is reached. This criterion can be written as:

$$\max \left\{ \frac{\langle t_n \rangle}{t_n^o}, \frac{t_s}{t_s^o}, \frac{t_t}{t_t^o} \right\} = 1 \quad (6.2)$$

where t_n , t_s and t_t are the already defined stresses in normal, first shear, and second shear direction, respectively. And, t_n^o , t_s^o and t_t^o represent the limiting stresses for damage initiation in normal, first and second shear directions, respectively. A purely compressive stress state does not trigger the damage initiation, which is represented by Macaulay brackets.

After the criterion for initiation is reached, the damage evolution initiates the degradation of the cohesive stiffness. The damage at any contact pair of the cohesive surfaces follows a linear softening, which can be represented by a scalar damage variable D_v , defined as:

$$D_v = \frac{\delta_m^f (\delta_m^{max} - \delta_m^o)}{\delta_m^{max} (\delta_m^f - \delta_m^o)} \quad (6.3)$$

Where δ_m^f , δ_m^o and δ_m^{max} are the effective separation at complete failure, the effective separation at damage initiation and the maximum value of the effective separation attained during the loading history, respectively. The value of D_v lies between 0 to 1, where 0 is an undamaged case, and 1 is a fully damage interaction. Intermediary values represent cases in between the beginning of the damaging process up to failure. Then, the contact stress components that softens through damage evolution are affected by the scalar damage variable D according to:

$$t_n = \begin{cases} (1 - D_v)\bar{t}_n, & \bar{t}_n \geq 0 \\ \bar{t}_n, & \text{otherwise} \end{cases} \quad (6.4)$$

$$t_s = (1 - D_v)\bar{t}_s, \quad (6.5)$$

$$t_t = (1 - D_v)\bar{t}_t, \quad (6.6)$$

where \bar{t}_n , \bar{t}_s and \bar{t}_t are the contact stress components predicted by the elastic traction-separation behaviour for the current separations without damage in normal, first and second shear directions, respectively. Although the damage evolution formula is given about the separation, it can also be defined in energy [201, 203]. In this case, the energy dissipated during the damage or the fracture energy, G_c , is used to define the damage evolution. Which can be associated to the area under the curve from the plot presented in Figure 6.7.

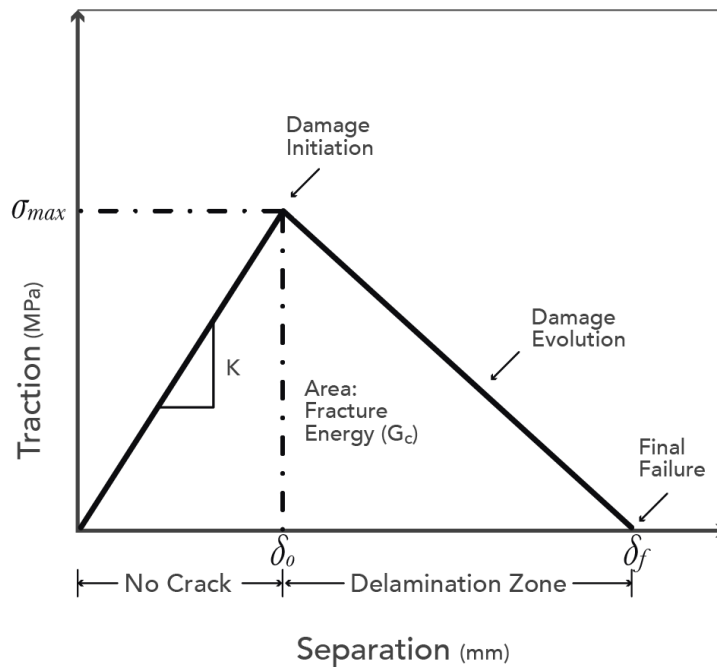


Figure 6.7: Schematic of a bilinear traction-separation law for cohesive zone model. The damage initiation and damage evolution criteria are indicated by σ_{max} and G_c , respectively.

In the simulations developed in this work, the damage initiation and evolution described the interaction properties of a gold-epoxy interface. The findings of previous chapters allowed for the surface-based cohesive behaviour modelling, in which no interlayer was considered, and the properties at the vicinity of the interface maintained their underlying responses. The damage initiation of 45 MPa was defined by a maximum stress criterion, obtained experimentally by the interfacial shear strength experiment described in the last section. Additionally, the damage evolution was described in terms of fracture energy. A typical value for metal-epoxy fracture energy is relatively low [205–208]; the value adopted in this work was 0.05 kJ/m². The materials constitutive laws and the boundary conditions of the simulations in this chapter are presented in Section 3.5.1.

6.2.1 Simulating the interfacial shear strength test

In this section, the interface between gold-epoxy was modelled to simulate an interfacial shear strength test. The surface-based method allows for assigning the interface characteristics as a surface interaction, which was limited to the two surfaces in contact between the top and bottom parts of the microcolumns. The comparison between the simulation and experimental results is presented in the diagram of Figure 6.8. Here, simulated cylindrical and square-cross-sectional microcolumns are compared with the experiment presented in Figure 6.1, considering the same interfacial area in all microcolumns. In addition to the load-displacement curves, the diagram presented in Figure 6.8 shows the simulated microcolumns in three instances:

1. Before the load is applied, showing the phases are in full contact with one another.
2. Before the peak load, showing the accommodation of the deformation, mainly at the top of the microcolumn.
3. After the interface failure, showing that the top part has slid over the bottom part of the microcolumns, which was also the failure mechanism observed in the physical experiment shown in Figure 6.1.

A good agreement in terms of the load-bearing capability of the microcolumns was observed, which indicates that a maximum stress criterion is adequate to determine the collapse of the interface. The response of the two simulated microcolumns was very similar once the interfacial areas were equal. Furthermore, the comparison of the stiffness shows that the experimental results were more compliant during the loading segment. Nevertheless, since the simulations avoided all the implications of establishing contact between the indenter and the top of the microcolumn, a stiffer response is expected. Finally, as discussed in Section 6.1.1, the experimental response is governed by the indenter springs after the interface's collapse. Therefore, the comparison between simulation and experiment can not be correlated after the beginning of the sliding process.

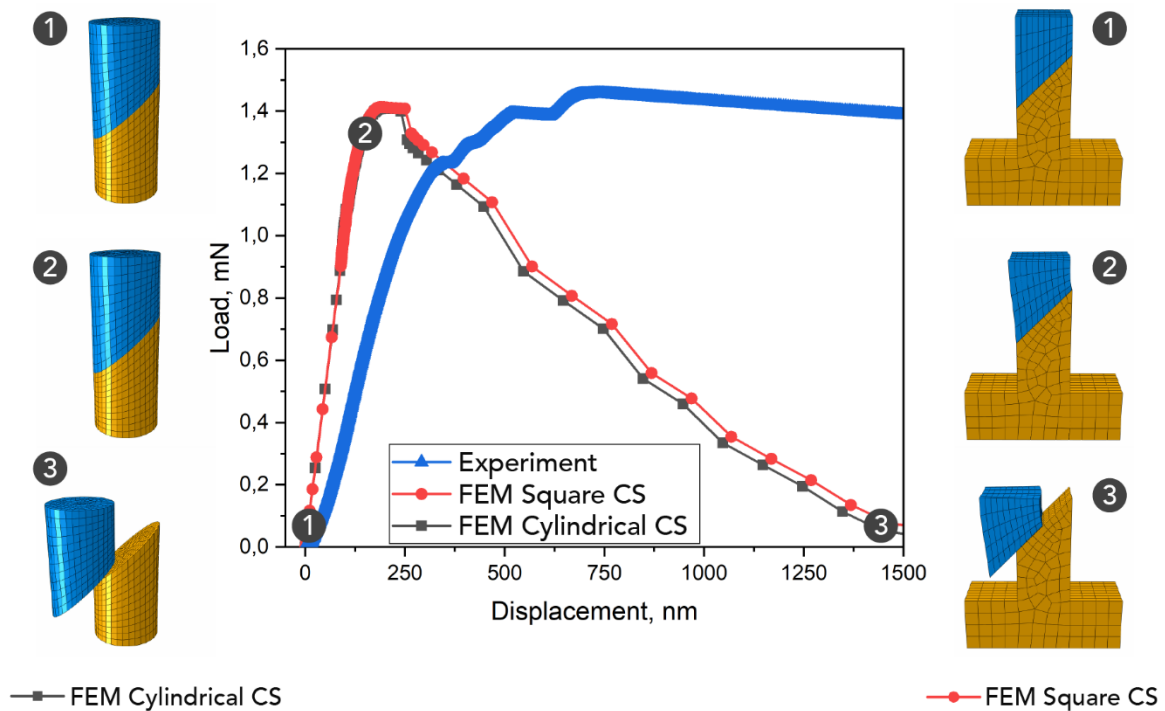


Figure 6.8: Comparison between physical experiment and FEM simulations of cylindrical and square cross-sectional microcolumns for interfacial shear strength testing. The representation of the two simulated microcolumn shows how the displacement is accommodated in three instants during the compression, which are indicated in the load-displacement curves.

The FEM allowed for a more detailed investigation of the stress conditions at the interface. Here, the surfaces in contact at the interface were analysed using two of Abaqus' outputs: CShear1 and CSMAX. The former gives the shear stress component in the slip direction, while the latter tracks the damage initiation criterion in the cohesive surface on a 0 to 1 scale, in which values < 1.0 indicate that the damage initiation criterion has not been met. Figure 6.9 shows the load-displacement curve of the simulated microcolumn compression with an inclined interface. The two indication points in the curve indicate the beginning and the end of the interface collapse. Additionally, the CShear1 and CSMAX outputs are shown in the interfacial surface of the epoxy part of the microcolumn. The colour in the CShear1 transition gradually from blue (0 MPa) to red (45 MPa), while in the CSMAX, only two colours constitute the scale, blue (0) and red (1). Therefore, in both cases, the colour red represents that the damage initiation criterion has been met. Additionally, Figure 6.9 also shows the stress distribution along the loading direction before interface collapse.

As shown in Figure 6.9, the microcolumn's structural integrity is intimately related to the interfacial behaviour. Although some interfacial regions start to fail at relatively low loads, the microcolumn's collapse only occurs whenever the whole interface fails. The microcolumn geometry prevents the delaminated regions from sliding before the critical stress is reached in the

totality of the interfacial area. Therefore, the microcolumn's load-bearing capability is directly proportional to the bonding strength between the phases and the stress distribution. Hence, the simulation reproduced the experimental results.

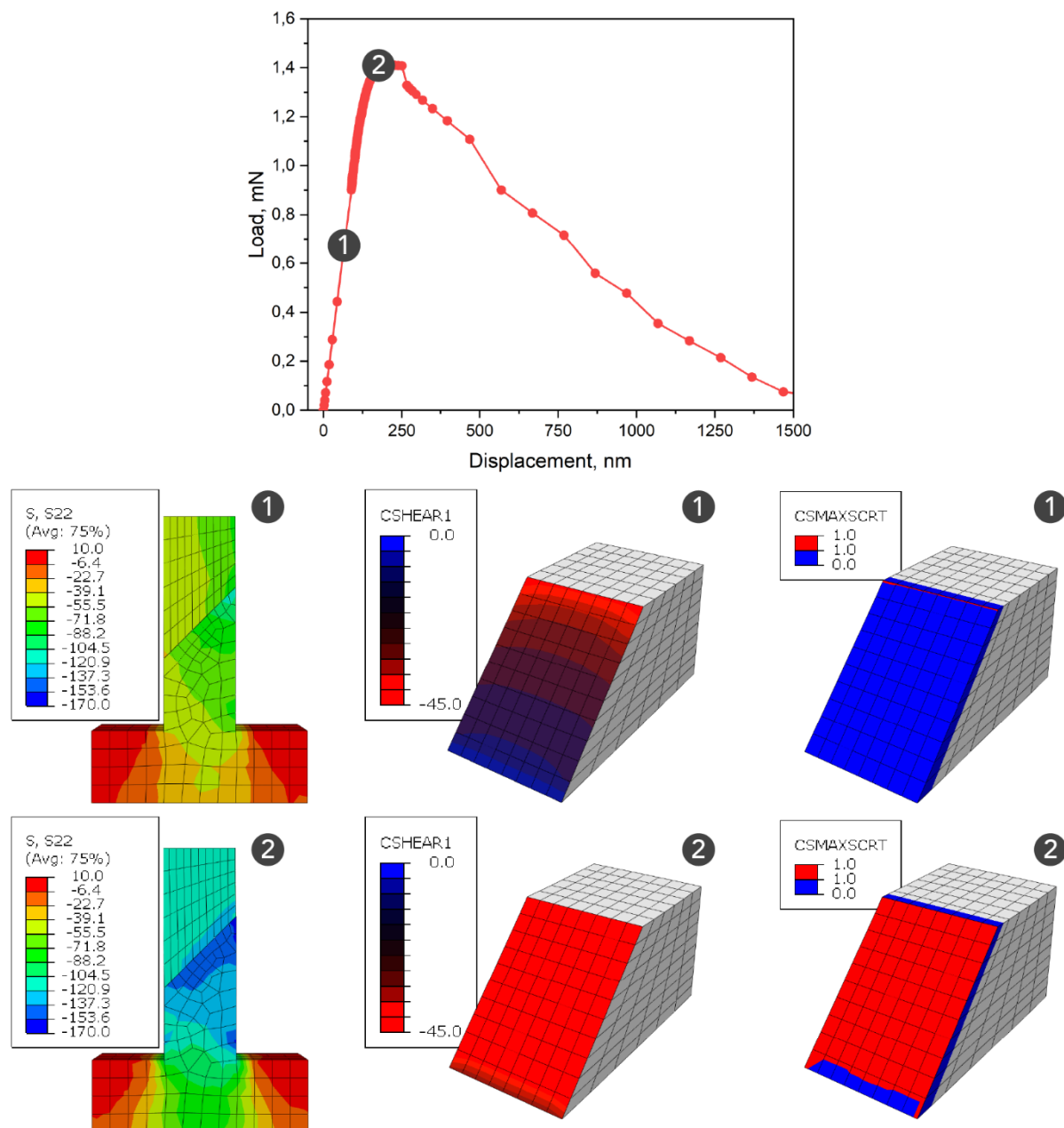


Figure 6.9: Load-displacement curve of an interfacial shear strength test. The diagram shows the corresponding outputs for CShear1 and CSMAX on the interfacial surface and stress on the loading direction. The colour red represents that the damage initiation criterion has been met in the CShear1 and CSMAX outputs.

6.2.2 The effect of interfacial properties on the interfacial behaviour

In this section, the influence of the simulation parameters is investigated in an interfacial shear strength test. Three parameters are investigated here: damage evolution, damage initiation, and the height of the polymer part in the inclined microcolumn. First, the influence of the damage evolution was investigated by simulating three levels of fracture energies: 0.03, 0.05 and 0.07 KJ/m². These values represent the typical range of property for a metal-polymer interface [205, 207]. Here, a low damage initiation (5 MPa) relative to the value measured experimentally was used to simplify the deformation analysis. Figure 6.10 shows the load-displacement curves for three simulation runs with an increase in damage evolution criteria. As it can be observed, the peak load remains constant for all curves, but the decay on the post-debonding behaviour is affected. Increasing the fracture energies allowed the microcolumns to carry slightly higher loads after the interface's debonding. Nevertheless, the influence of the damage evolution is limited since simulating higher fracture energy would diverge from a typical metal-polymer interface. Therefore, for epoxy-metal systems, the damage evolution does not alter the observed behaviour significantly.

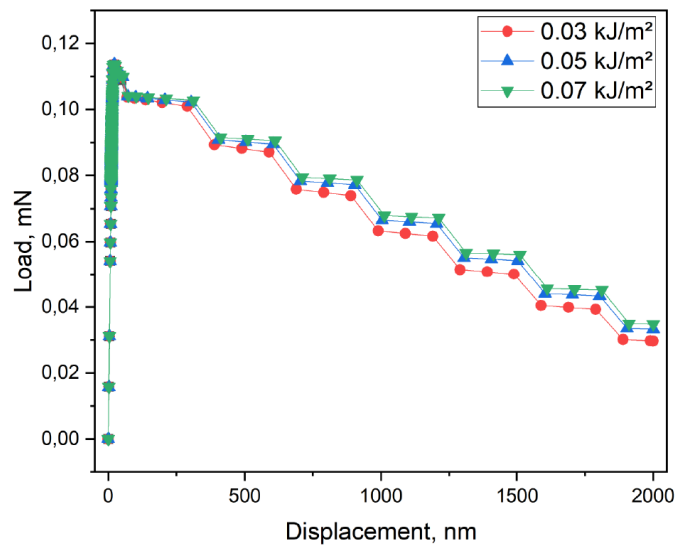


Figure 6.10: Load-displacement curves of three FEM simulations showing the effect of the damage evolution parameter on the load-bearing capability. The range of the simulated fracture energies corresponds to a typical property of metal-epoxy interfaces.

The influence of the damage initiation was investigated by simulating five levels of interfacial strength: 5, 20, 35, 50, and 65 MPa. Additionally, a damage evolution parameter of 0.05 kJ/m² was utilized in all simulation runs [205, 207]. Figure 6.11 shows the load-displacement curves for five simulation runs with increasing damage initiation criteria. As it can be observed, the damage initiation is proportional to the peak load in the interfacial shear strength test. The simulations for the 50 and 65 MPa showed the same peak load, which will be further discussed

later. Moreover, all the microcolumns presented the same stiffness until the maximum stress is reached, which is consistent with the literature presented in Section 2.2 regarding the effect of the interfacial properties in the stiffness of composite materials. After the interface collapses, the crossing of the curves can be understood as an artefact of the constant damage evolution. Since the damage evolution can be interpreted as the area below the curve in a stress-strain curve, reaching a higher peak load results in a steeper decay after the debonding.

Moreover, the stress distribution at the loading direction for the five simulations is shown in Figure 6.12. The microcolumns were compressed to a displacement of 650 nm. The colour scales show the stress distribution in MPa, except for the simulation for an interfacial strength of 65 MPa. Although the stress distribution is similar in all microcolumn, the stress levels increased with the increase of the bonding strength. In the 50 and 65 MPa interfacial strength simulations, the stress levels were sufficient to yield the top epoxy part of the microcolumns. In the 50 MPa interfacial strength simulation, the deformation is slightly concentrated at the top of the microcolumn. However, the interface does not delaminate entirely in the 65 MPa interfacial strength and instead results in a substantial deformation to accommodate the applied displacement.

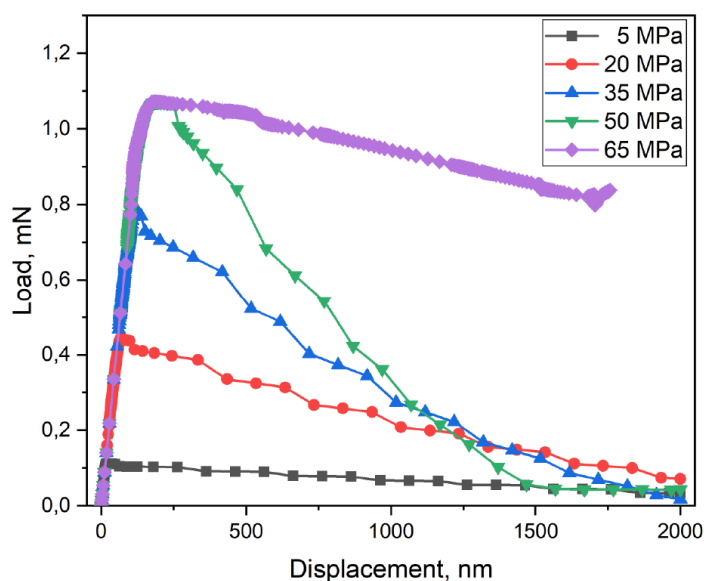


Figure 6.11: Load-displacement curves of five FEM simulations showing the effect of the damage initiation criteria on the load-bearing capability.

The combination of the plot in Figure 6.11 and the diagram in Figure 6.12 indicated that a low damage initiation activates interface collapse before the epoxy yielding. Due to the microcolumn's geometry, the top part slides over the bottom part, which allows the accommodation of the applied displacement without plastic deformation in the epoxy part. For an increasing bonding strength, the epoxy yielding starts before the interface collapses entirely. The balance between stress distribution and bonding strength determines if the interface collapses after

an initial deformation or the deformation of the epoxy entirely accommodates the displacement. The simulation 50 MPa and 65 MPa exemplifies these two possibilities, respectively.

The influence of the stress distribution on the interfacial behaviour motivated the investigation on the effect of the polymer height in the simulation of interface shear strength tests. The height of the polymer part is shown in Figure 3.6, and for the analyses here presented, the simulations included three heights levels: 2, 3, and 4 μm . Figure 6.13 shows four plots presenting microcolumns with a specific bonding strength: 5 MPa (a), 20 MPa (b), 35 MPa (c) and 50 MPa (d). In each plot, three curves are shown representing the simulated levels of polymer heights. In a general way, the stiffness of the microcolumns was affected by the polymer height. Not surprisingly, increasing the polymer height results in more epoxy in the simulated volume, which decreases the observed stiffness.

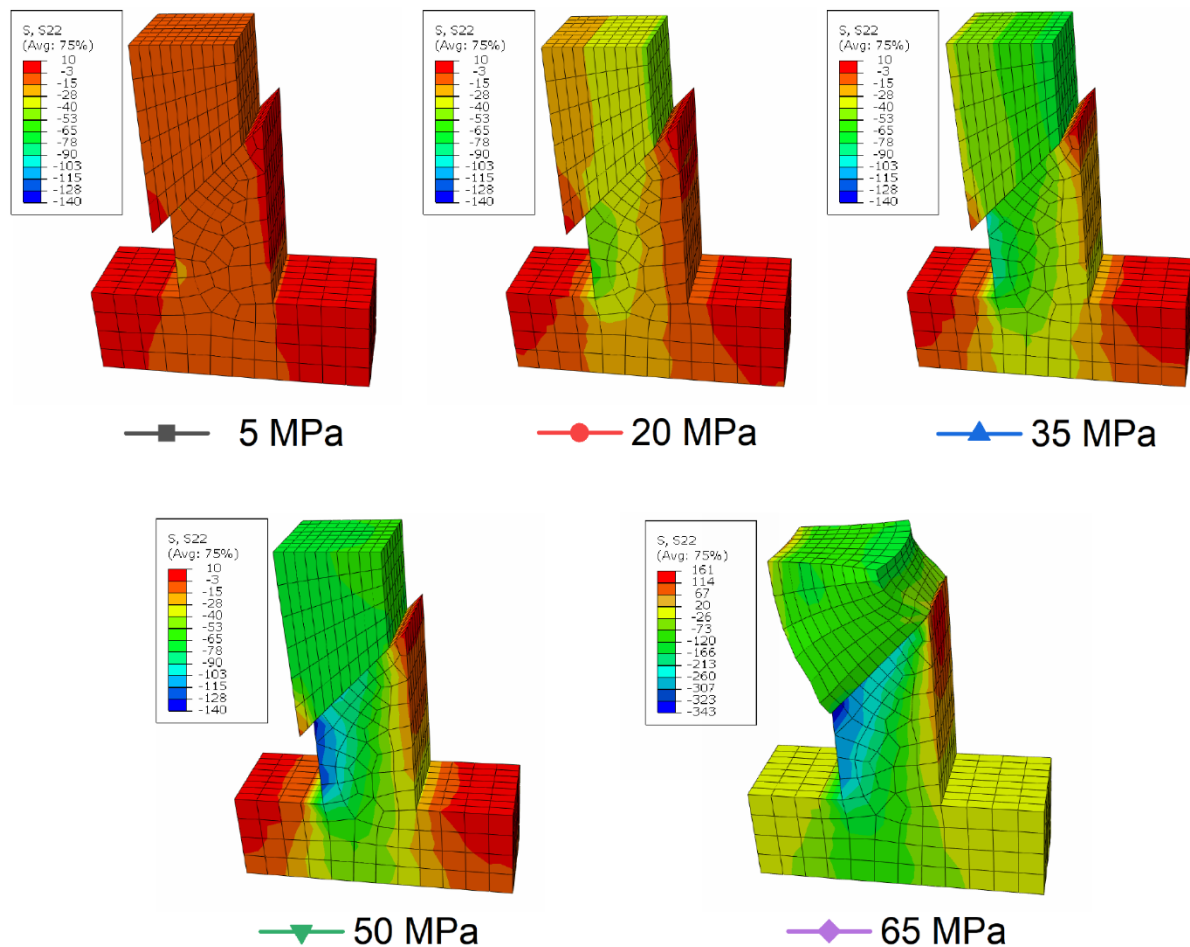


Figure 6.12: Stress distribution on the loading direction for the five simulation runs. The colour label is consistent with the damage initiation (bonding strength) presented in Figure 6.11. The presented microcolumns were compressed until 650 nm, the interface collapsed in all presented microcolumns but the 65 MPa simulation.

Moreover, no additional difference was found when varying the polymer height in the simulations of the bonding strength of 35 MPa and below, which indicates that the yielding stresses were not reached. However, the plot of 50 MPa (Figure 6.13 (d)) shows the interfacial behaviour varying according to the polymer height. For the 2 μm polymer height, the peak load is immediately followed by the decay, which indicates that the debonding happens before the epoxy yielding. In the case of the 3 μm polymer height, the decay only happens after a short plateau, which is substantially more significant in the 4 μm polymer height simulation. These plateaus represent the epoxy yielding, which continues until the interface collapses, and the top part of the microcolumn is free to slide.

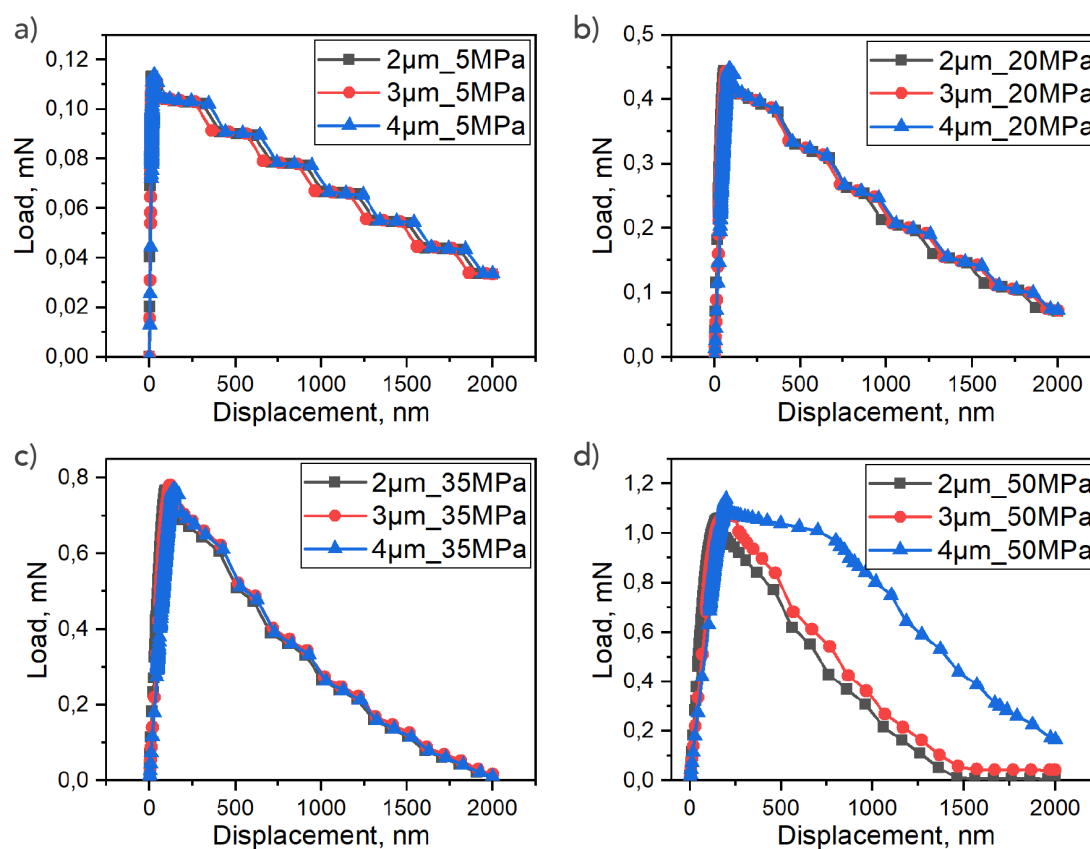


Figure 6.13: Plots showing the influence of the polymer height on the interfacial shear strength tests. Each plot shows the simulation of 3 microcolumns with an increasing polymer height at a specific damage initiation (bonding strength).

The interfacial behaviour observed in an interfacial shear strength test may vary according to bonding strength and the stress conditions at the interface. The interface's collapse only occurs whenever the stress distribution allows the critical stress levels to be reached on the entire interfacial area. Before that happens, the epoxy yield may occur, as represented in two cases in Figure 6.14. The first case exemplifies a microcolumn with strong bonding between the two phases (65 MPa in this case), which was sufficient to keep the interface attached during the totality of the

applied displacement. In the second case, even with a lower bonding strength (50 MPa), the higher polymer height is sufficient to alter the stress distribution and activate yielding near the top of the epoxy part of the microcolumn. Nevertheless, further compressing the microcolumn allows the critical stress to be reached on the entire interface area, which then activates the sliding of the top part. The load-displacement curves are presented in Figure 6.14 (a), and the magnitude of deformation on both examples is shown in the same colour scale in (b). The dashed outlines show the shape before deformation.

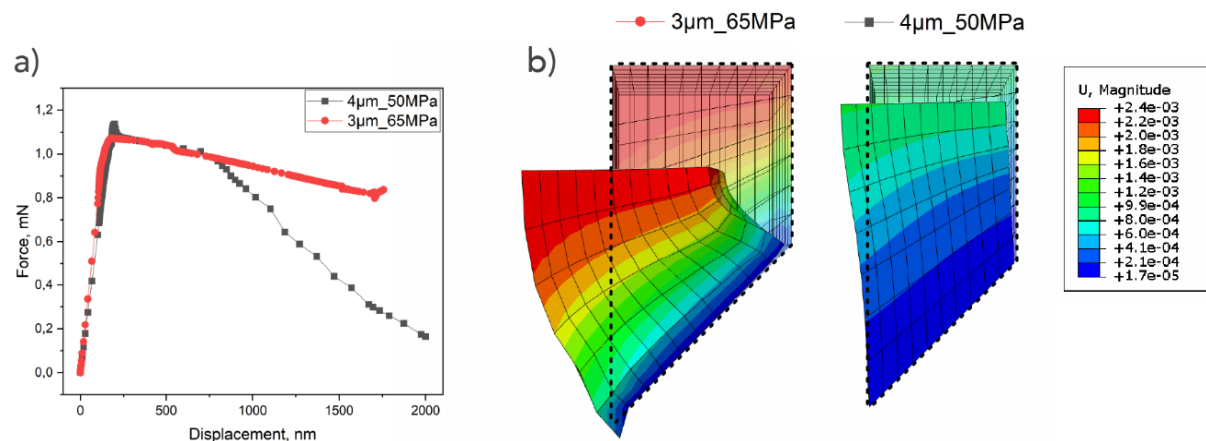


Figure 6.14: (a) Load-displacement curves showing the comparison between the two possible yielding behaviour observed in this work for the interfacial shear strength testing. The red curve represents a short microcolumn with a strong interfacial bonding, which does not collapse during compression. The grey line represents the response of a taller microcolumn with a lower bonding, which is slightly deformed before the debonding of the interface. (b) The deformation's magnitude on the top part of both microcolumns, where the dotted outlines show the shape before deformation.

6.3 Conclusions

The interfacial behaviour of the gold-epoxy interfaces was investigated experimentally using a shear-based method, which successfully activated the interfacial failure mechanism throughout the microcompression of microcolumns with an inclined interface. An analysis of the interfacial collapse from the load-displacement curves was developed using the loading stiffness response, which separated the slipping of the top part of the microcolumn to the load necessary to collapse the interface. The characteristic interfacial strength in the gold-epoxy interface was found to be 45 MPa, and no correlation between the interfacial shear strength with the interfacial area of perfectly bonded microcolumns was observed. However, whenever the interface presented defects, the measured strength dropped to levels similar to those measured using macromechanical approaches in similar materials systems [195, 196].

The interfacial shear strength measured here and the results from previous chapters allowed the development of a modelling approach based on the finite element method. The interfacial characteristics were assigned to the interfaces of bi-materials microcolumns, which the simulations presented a good prediction of the load-bearing capability. Additionally, the simulation approach was capable of replicating the interfacial failure and exhibited the sliding of the top part of the microcolumn after the interface collapse, as observed in the physical experiments. The tuning of the simulated parameters allowed for investigating the interfacial properties' independent effects on an interfacial shear strength test. In closing, the interfacial behaviour was found to be a balance between the bonding strength, the properties of the underlying materials, and the stress distribution as dictated by the morphology of the two phases.

7 The overall mechanical response of NPG-polymer composites

In this chapter, the findings of previous chapters are combined to improve understanding of the mechanics of NPG-epoxy composites, focusing on the contribution of the constituent phases and their bonding strength. A mesh of the 3D representation of NPG-epoxy composite was recently developed [11], and here it was adapted to account for the interfacial characteristics and the size-independent mechanical response of the epoxy phase. The FEM simulation was utilized to evaluate the composite's mechanical response under compression, and the interfacial failure was compared with the experimental delamination reported in the literature [11]. Furthermore, the strength of the bonding between constituent phases was extrapolated to reveal its contribution to the composite's overall response and to evaluate its potential in tailoring the composite properties. Moreover, the properties of the NPG-epoxy composites are analysed in relation to the bulk properties, and the values found for the characterisation of NPG and NPP samples. The results from the separated phases (NPG and NPP) are compared to the composite's response, revealing the phases' interplay to accommodate the loading in the composite material. Here, the hardness and elastic modulus results are discussed in terms of analytical models considering the bulk properties and respective volume fractions. Furthermore, the strengthening at small length-scales is evaluated in both the isolated phases and the composite, which motivated further study on the mechanisms behind the size effects in Au ligaments. To this end, TEM microscopy was used to investigate the dislocation activity of NPG samples with contrasting ligaments sizes.

7.1 On the effect of the interfacial property

The effect of the interfacial behaviour in NPG-epoxy composites is investigated here by finite element simulations. Hu recently developed a meshed 3D reconstruction of the composite with mean ligament size of the NPG, $\langle D \rangle$, equals 400 nm [11]. Hu also identified the minimum

representative volumes (RVs) for the global structural properties of the composites investigated in this thesis. Nevertheless, only a section with a cubic length of 2 μm of the original reconstruction was utilised in this thesis since simulation volumes closer to the RV were unable by the increased computational demand of the interfacial processing. Figure 7.1 (a) shows the simulated volume, in which the materials inputs and boundary conditions were introduced in Section 3.5.1.

The mechanical response of simulation volumes smaller than the RV may diverge from the global properties. Effects on the spatial variation and proportion of phases on the simulated volume can impact the load-bearing capability. Depending on the local structure, the mechanical response may also be affected by the load orientation. This artefact could be further impacted by the concept of an interfacial strength dependent on the load direction (α_{int}) introduced in Section 2.2. The shear-lag analysis, also introduced in Section 2.2, shows that axial and shear stresses vary drastically according to the position and load orientation. A simulated volume was selected containing a similar volume fraction of the constituent phases as the RV, which reduced the responses' deviation. Also, adopting an α_{int} equals to one ensures the interfacial failure at the same stress levels independently of the load orientation. Nevertheless, the effect of the internal constraints from the ligament network and the connectivity of the load-bearing structure are reduced in the simulations presented here.

Figure 7.1 shows the responses of the simulated volume according to the load orientation, in which the arrows in (a) represent individual uniaxial compressions of the composite reconstruction on the x , y , and z -directions. The engineering stress-strain behaviour for an 8% compression is shown for the three directions in Figure 7.1 (b). Additionally, two dashed lines are plotted, showing the literature result for FEM simulation of the composites' RV with unbreakable interfaces in black and experimental data from the microcompression of NPG-epoxy composites in grey [11]. Here, the elastic modulus obtained from the initial slope is 9 GPa for all the curves, which is slightly below the value found using the RV (9.7 GPa) [11]. However, the original RV mesh has 67 % of polymeric volume fraction, while the simulation volume simulated here have 70%. Therefore, the slight difference in the elastic modulus can be easily attributed to the higher volume fraction of polymer in the composite mesh simulated in this thesis.

Moreover, the yielding stresses, calculated by the 0.2% strain offset in the stress-strain curve, were 0.08, 0.1 and 0.11 GPa for compression along the x , y and z axes, respectively. As discussed in Section 2.2, the strength of composite material is a function of the interfacial strength. Although the interfacial model was the same in all simulation runs, the responses were different since the ligament network's orientation inside the simulated volume varied according to the analysed direction. Not surprisingly, the curves converge at higher strain levels when all the interfaces have collapsed. The yielding above the bulk epoxy strength (dotted line) confirms that the ligament network acts as a reinforcement, constraining the epoxy deformation. Nevertheless,

the comparison with the experimental results shows that the influence of the structural constraints is reduced in the simulations presented here.

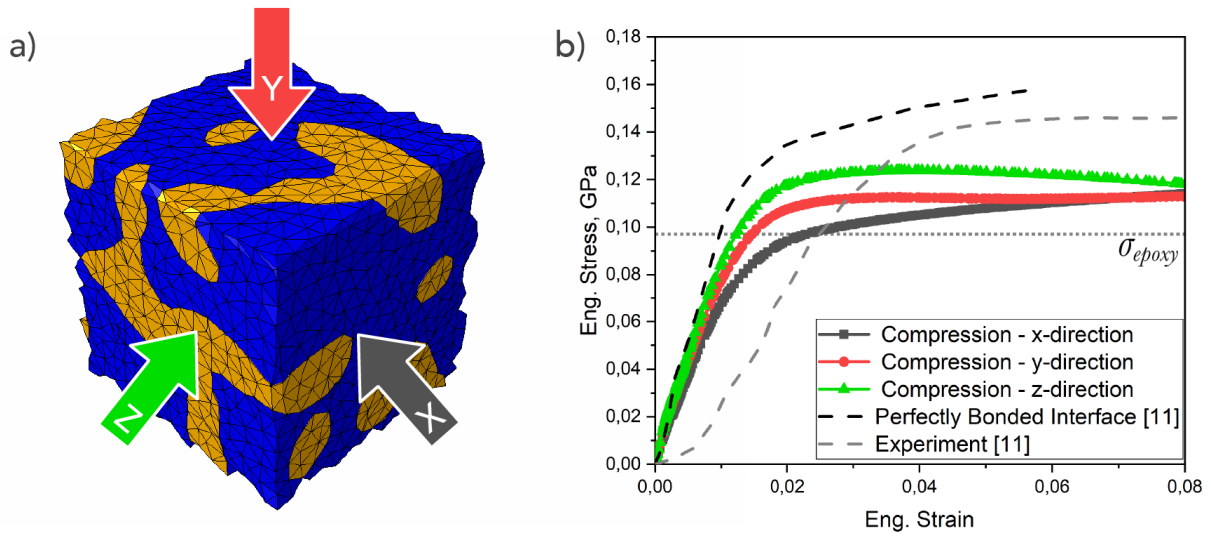


Figure 7.1: (a) Section with a cubic length of 2 μm of the 3D mesh developed by Hu from the 3D reconstruction of the NPG-epoxy composite [11]. The arrows indicate the directions in which the cube was uniaxially compressed. (b) engineering stress-strain curves of the FEM simulation on the x , y and z - directions. The dashed lines show literature result for FEM simulation of the RV of the composites with unbreakable interfaces in black and experimental data from the microcompression of NPG-epoxy composites in grey [11], and the dotted line represents the yield strength of the bulk epoxy.

The interfacial behaviour is further investigated for the compression in the x -direction, shown in Figure 7.2, where the stress-strain curve and the first derivative of the engineering stress are plotted for computing the slope every ten points. The diagram presents pictures showing the simulation outputs on the stress distribution, the criteria for collapsing the interface, CSMAX, and the deformation's magnitude. The colour scale indicates the stress levels and the deformation magnitude, while the CSMAX red indicates the interface failure. The outputs are shown in four instances, which are represented by the circles in the stress-strain curve.

Before the stress levels are capable of collapsing the interface, the stress and strain are well distributed throughout the cube., The phases are still in full contact with each other, which results in the composites maximal stiffness, as discussed in Section 2.2. The slope is constant, indicating a purely elastic response. Then, the criteria for collapsing the interface are widely reached, allowing the accommodation of the displacement separately. The slope fluctuates, which is likely a consequence of the localized interfacial collapse and further redistribution of stresses in accommodating the displacement. Nevertheless, the polymer yielding has not been initiated yet, and the strain distribution is still reasonably uniform.

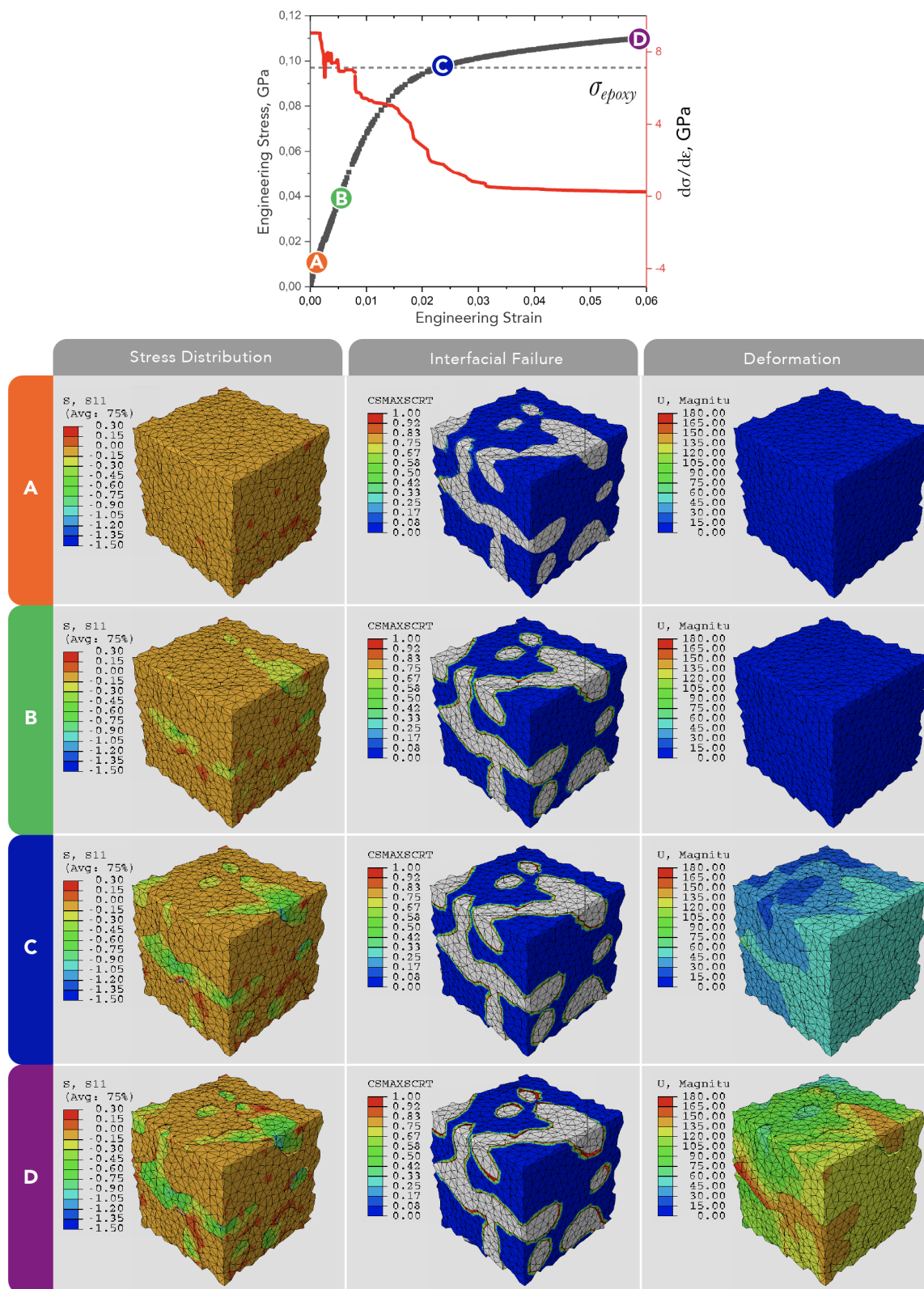


Figure 7.2: Engineering stress-strain behaviour and the first derivative of the stress curve complemented by the simulation outputs showing the stress distribution, the criteria for collapsing the interface (CSMAX), and the deformation's magnitude. The progression shows the interface collapsing while the stress is distributed all over the network structure. After the interface breaks, the phases are free to accommodate the displacement separately, and the polymer yielding governs the response.

As the load increases, the interface has collapsed in the entire structure, and the phases are not bonded anymore. Stress levels higher than the polymer yielding lead to the deformation concentrated near the face where the displacement is being imposed. The slope stops to present characteristic drops due to the localized interfacial collapse and follows a regular softening, which is reasonable associated with the composite yielding. Finally, the polymer phase further yields against the compressing plane and the Au ligaments concentrates stresses, acting as a constraint to the polymer deformation.

The delamination process was investigated by observing a cross-section of the simulated volume perpendicular to the loading direction. Figure 7.3 shows the same cross-section at 0, 1, 2, 6 and 10% of global strain, where the load was applied perpendicular to the paper plane and the Au ligaments are indicated by arrows. Once again, the colour scale shows the CSMAX output with red colour indicating interfacial failure. The progression in Figure 7.3 shows that the interface fails completely. Delamination takes place after the phases are free to accommodate the stress separately, creating some porous between the phases. The delamination sites are localised near regions of high curvature, and the shapes of the created porous resemble a “horseshoe”, which was also observed experimentally in NPG-epoxy composites [11]. As an example, the inset in Figure 7.3 shows experimental delamination observed in a cross-section of highly deformed microcolumns in which a very similar porous shape can be identified [11]. The formation of these delamination sites was associated with the lateral expansion under uniaxial compression [11].

The simulation results presented here reinforce the difference between the observed delamination and the actual debonding of the interfaces. In the case of the NPG-epoxy composite, the experimental observation of delamination sites is indicative of a weak interface since localised deformation to create the delamination pores required the separated deformation of the phases. The measurement of the characteristic interfacial strength in Section 6.1 and the simulation results in Figure 7.2 sum on the evidence for a weak interface in NPG-epoxy composites. However, the simulations results showed that the interfaces were weak enough so that the interfacial breaking took place in the entire structure. Thus, phenomena that depend on interfacial breaking could be exploited in these materials. Composites with weak interfaces are discussed briefly in Section 2.2, and generally, the energy dissipated in the breaking of the interface is explored as a toughness mechanism. On the other hand, the premature interfacial collapse could prevent the composite from reaching higher strengths. In the case of NPG-polymer composites, there is potential tailoring of the properties, and the effect of the interfacial properties can be exploited.

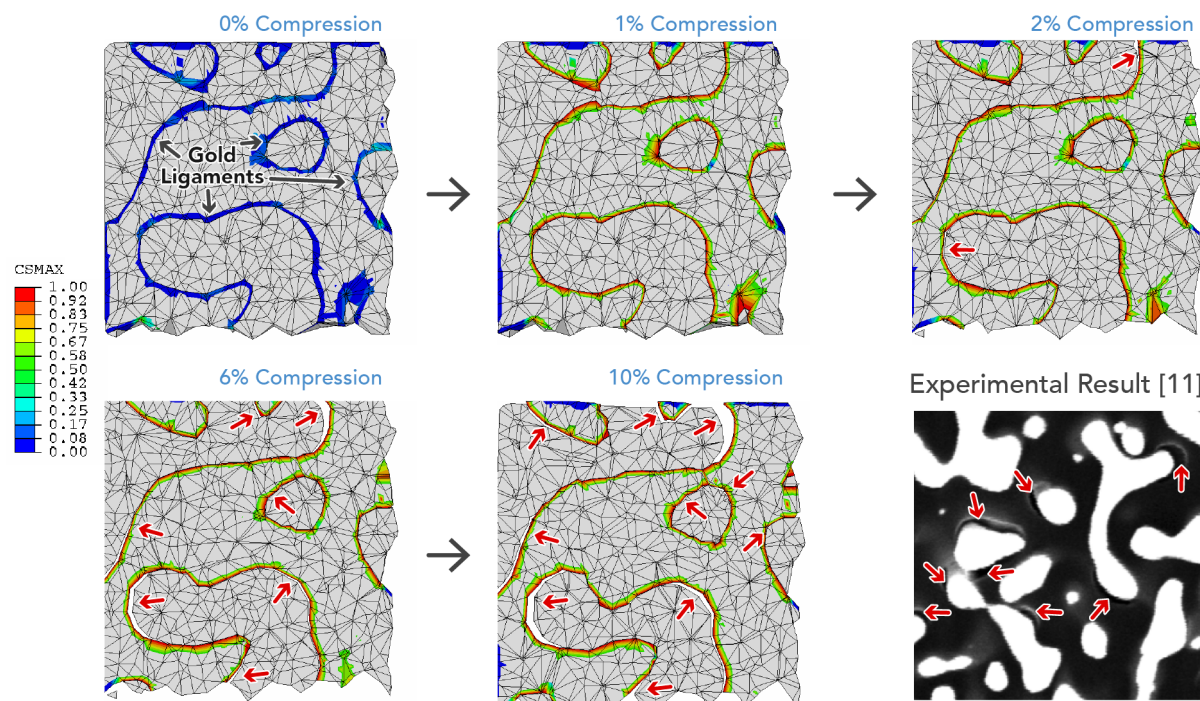


Figure 7.3: Composite cross-sections showing the CSMAX simulation output during a uniaxial compression in which the load is applied perpendicular to the paper plane, and red colour represent the reaching of the criteria for breaking the interface. The Au ligaments are indicated by arrows in the first cross-section before the load was applied. Additionally, four cross-sections show the delamination progression at 1, 2, 6 and 10 % of global strain, and the porous at the delaminated sites are indicated by red arrows. The last picture shows experimental delamination observed in a cross-section of highly deformed microcolumns in which a very similar porous shape can be identified [11].

The simulation results showed so far in this chapter utilized the interfacial strength measured experimentally in Section 6.1 (45 MPa). In Figure 7.4, the relationship between the interface property and the composite response is further addressed, in which various bonding strengths are simulated and compared with simulation from perfectly bonded interfaces and experimental results. The simulated interfacial strengths were 20, 45, 97, 150 and 200 MPa, represented respectively by the colours red, blue, green, pink and yellow. Additionally, two dotted lines are plotted, showing the literature result for FEM simulation with unbreakable interfaces in black and experimental data from the microcompression of NPG-epoxy composites in grey [11]. The dotted lines appear in Figure 7.4 (a), showing the stress-strain curves as upper and bottom limits for the simulated results at the initial strain levels. At first, all the simulations presented similar stiffness, with the elastic modulus obtained from the initial loading slope in the strain range up to 0.002 is 9 GPa. This behaviour can also be observed in Figure 7.4 (b), which shows the slope of the engineering stress as a function of the strain. Here, the purely elastic response can be observed. Although the experimental data is initially more compliant, this behaviour is likely an artefact of the measurement process. The elastic modulus of the composite measured by CSM of

microcompression testing, which circumvents the establishing of contact between indenter tip and sample's surface, also report values about 10 GPa [11].

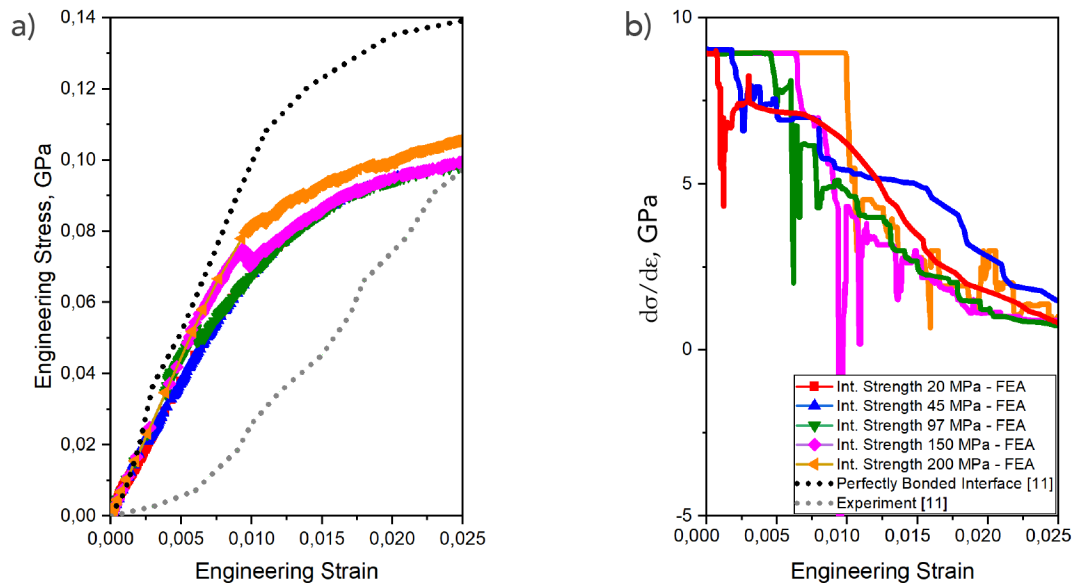


Figure 7.4: Simulated mechanical response of NPG-epoxy composite showing the effect of increasing interfacial strength compared to the literature value of simulation of perfectly bonded phases and experimental results. [11] (a) Stress-strain curves in which the literature values act as upper and bottom boundaries to the simulated interfacial strength. (b) Stress's first derivative according to engineering strain. Here, the first drops can be associated with the initiation of the interfacial failure.

The simulated responses start to differ at relatively low global stress levels whenever the weakest interface breaks. The drops in the first derivative response show the exact instants when each of the simulation responses stops being perfectly elastic, which could be correlated to the start of the interfacial debonding process. It is reasonable to assume that the location of the first interface to collapse depends on the stress distribution in the composite structure, but the progression of the interfacial debonding would diverge according to the stress levels in which the first interface breaks. This behaviour could explain the different fluctuations in Figure 7.4 (b). Therefore, the structures accommodate and redistribute the stresses differently according to the stress level. As can be observed, a higher interfacial strength allows the simulated composite to withstand higher loads retaining its initial stiffness, which ultimately would allow for higher strength, as discussed in Section 2.2.

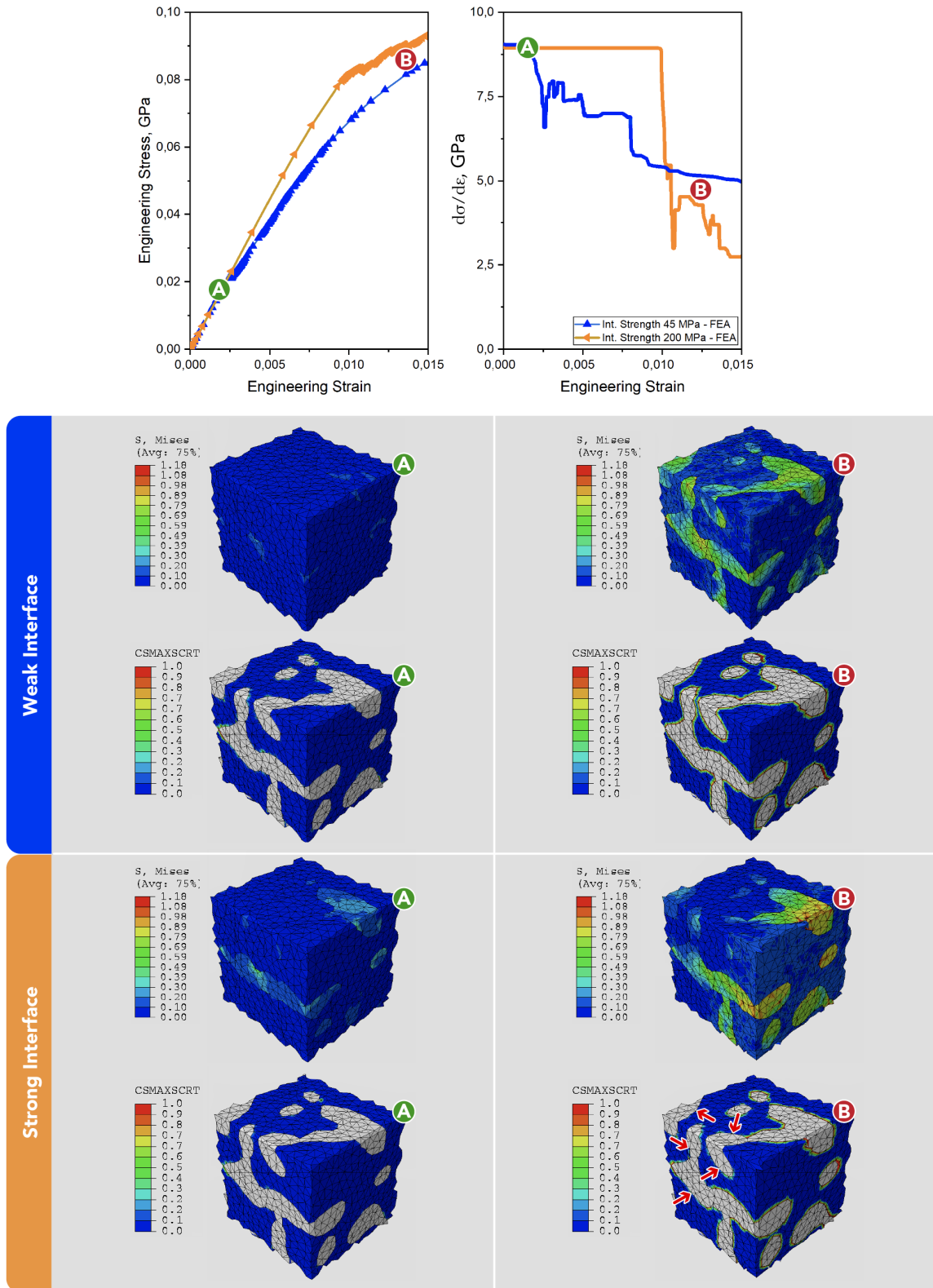


Figure 7.5: Engineering stress-stress and the first derivative of the stress curve complemented by the simulation outputs showing the stress distribution, the criteria for collapsing the interface (CSMAX) for the simulation of a weak (45 MPa) and strong (200 MPa) interfaces. The progression shows the interface collapsing entirely on the simulation with a weak interface, but there are regions still attached after the polymer starts to yield on the strong interface simulation. Arrows indicate these bonded regions.

In the simulated results presented here, the polymer yielding activation limited the potential to increase the composite strength, explaining the converging of all simulated curves at higher stress levels. Therefore, even as the weakest link in the deformation, the interfacial properties have a reduced impact under the compression. The interconnected composite structure allows the load transfer by the internal constraints even after the interfaces' debonding. Here, similar to the microcolumns simulation results in Section 6.2.2, local activation of polymer yielding or interfacial collapse depends strongly on the simulated structure. In the composite structure, the simulation results from strongly bonded interfaces show that interfacial debonding initiates before the polymer starts to yield. The contribution of the regions still bonded after the polymer starts to yield could be estimated by comparing the simulation curves presented here to the perfectly bonded simulation from the literature.

The effect of bonding strength between the constituent phases in the NPG-epoxy composite is analysed by comparing the compression behaviour from weak and strong interfaces. Figure 7.5 shows the stress-strain curves (a) and the first derivative of the stress curve (b) for the simulations of the interfacial strength of 45 and 200 MPa. In addition to the plots, pictures show the simulation outputs on the stress distribution and the criteria for collapsing the interface. The colour scale indicates the stress levels, while the CSMAX red indicates the collapse of the interfaces. The outputs are shown in two instances represented by the circles in the plots. Both simulations behaved similarly at lower load, displaying the same initial stiffness in Figure 7.5 (a). Initially, the stress is well distributed in both simulations. The phases are entirely bonded, which agrees with the influence of the interfacial strength in Section 6.2.2. Here, the elastic moduli equal to 9 GPa can be obtained directly from the first derivative curve.

As higher loads are reached, the response of the weak interface composite starts to soften, while the strong interface one keeps its purely elastic behaviour with the same stiffness. The softening can be explained by the accommodation of the imposed strain, mainly by the polymer deformation. Therefore, the CSMAX output shows the total collapse of the interface and the stress is well distributed on the Au network in the weak interface simulation. On the other hand, the strong interface composite remains partially attached after the polymer starts to yield. The CSMAX output shows that the interfaces have collapsed near the plane under compression, but many regions are still bonded together, indicated in Figure 7.5 by arrows.

This behaviour concentrates the stress distribution so that the ligaments adjacent to the debonded region reach higher stress levels, which further constrains the polymer yielding. It is debatable that whenever the interface is much stronger than the polymer strength, the simulation's interfacial failure could be activated by phase's separation criteria instead of the maximum stress criteria. In these cases, the deformation in one phase is so extensive that it breaks the interface, which could ultimately reduce the strength of the simulated composites. Although this effect could help explain the accentuated drop in the slope of the strong interface composite, a larger separation

criterion would be unrealistic to the properties of a metal-polymer interface. Therefore, it is reasonable that the weakest link of the chain, the polymer yielding here, would still govern the simulations' response.

7.2 On the contribution of each individual phase

This section further explores the mechanical response of NPG-polymer composites. When first introduced by Wang [97], the macrocompression response was reported as "much stronger" than each of its constituent phases. As presented in Section 2.1, the composite was compared by Wang to the NPG and the bulk epoxy property. Here, the composite response is put in perspective to its constituent phases and typical analytical models. Figure 7.6 shows a schematic of the bulk constituent phases, the separated constituent phases within the composite structure, and the NPG-epoxy composite. The morphology and structural length-scale of the composite can alter the response compared with the material's bulk property. Although the properties measured in the bulk materials lack the composite structure's influence, the alternative to characterize the composite combines the effects of structure with the interaction between the phase during a loading process. Therefore, an appropriate approach to evaluate a composite's property should acknowledge both the underlying bulk property and the effect of the composite structure.

As discussed in Section 2.2, gold and epoxy can present size-dependent mechanical responses at small sizes, but not necessarily these are activated from the structural length-scale. In the case of NPG, the small ligament size activates size effects, which improves strengthening at small structural length-scales. Additionally, dangling ligaments in the structure affect the connectivity and, therefore, the actual volume fraction contributing to the load-bearing capability. The idea of an effective load-bearing structure was proposed in the literature [11, 209] and recently supported by studies on the topological states showing rings on the NPG structures [210]. On the other hand, the investigation presented in Chapter 4 allows for a simplified analysis of the epoxy phase. Since no evidence supporting the structural size-effect was found and the higher volume fraction prevents dangling parts, the NPP property can be predicted based on the composite's actual volume fraction and the bulk property.

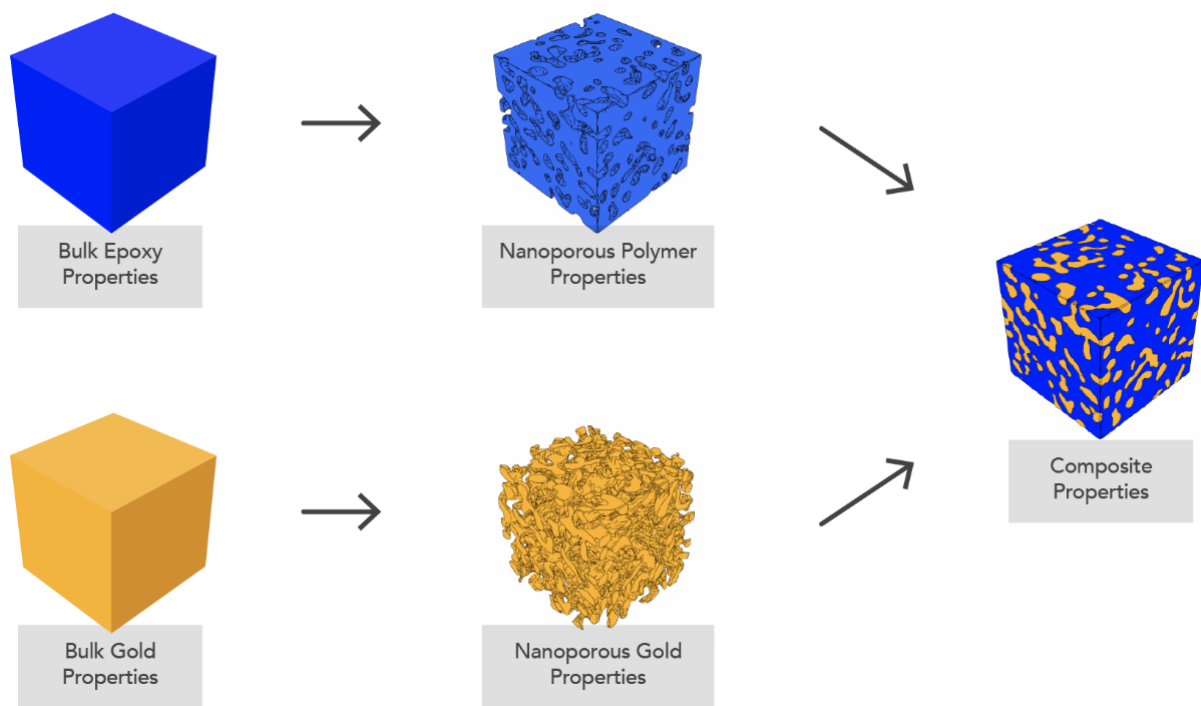


Figure 7.6: The diagram shows the NPG-epoxy composite, its bulk constituent phases and the separated phases within the composite morphology (NPG and NPP). Each of these pieces was separately characterized by nanoindentations.

The NPG can be characterized before the epoxy infiltration, and the properties of NPP were characterized in Chapter 4. Here, experimental results from the bulk materials, the separated composite phases, and the overall composite are analysed against themselves and analytical models. Figure 7.7 (a) and (b) show the respective hardness and modulus responses from nanoindentation results according to the average NPG ligament size, $\langle D \rangle$, including the responses of NPG, NPP, NPG-epoxy composite, and isostress and isostrain conditions. The dashed lines represent the bulk gold and epoxy's average properties using nanoindentation experiments from Chapter 5. The composite response was taken from Hu's works [11], which correspond to the same samples used in this NPP fabrication thesis. The value of $\langle D \rangle$ for the NPP samples corresponds to the average NPG ligament size before the etching treatment. Therefore, NPG, NPP, and composite can be analysed directly at the same corresponded $\langle D \rangle$. Each data point represents an average of at least ten measurements, and the error bars, whenever visible at the presented scale, indicate one standard deviation about the mean value. The isostrain and isostress conditions (dotted lines) were calculated using the bulk material properties and the effective relative density from the NPG structure identified by [11].

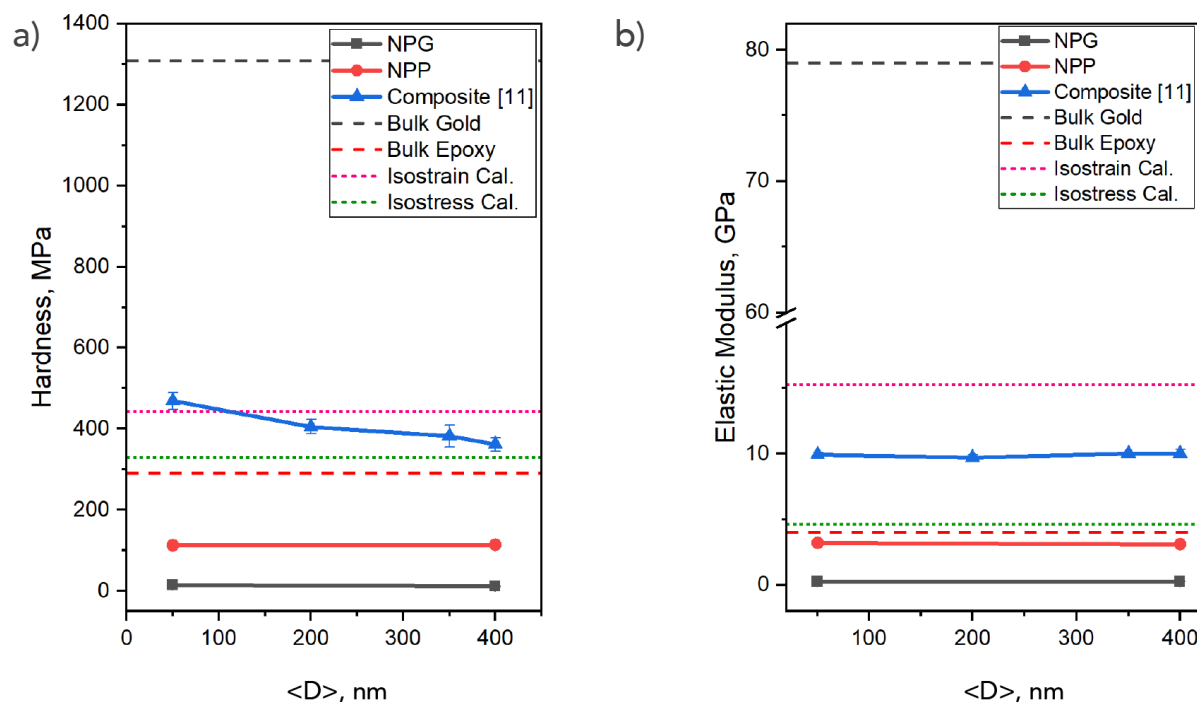


Figure 7.7: Nanoindentation results showing hardness (a) and elastic modulus (b) versus the NPG ligament size ($\langle D \rangle$) from nanoporous gold (NPG), nanoporous polymer (NPP) and NPG-epoxy composites. In the NPP results, $\langle D \rangle$ represents the size of the NPG ligaments before the etching treatment. The dashed lines represent the bulk gold and epoxy responses, and the dotted lines are analytical models. Each data point represents an average of at least ten measurements, and the error bars, whenever visible at the presented scale, indicate one standard deviation about the mean value.

Figure 7.7 shows higher values for hardness and modulus from the composite response than the separated constituent phases (NPP and NPG). Nonetheless, a comparison between the response of composite and the isolated parts, as presented in Figure 2.1, is not necessarily meaningful. The deformation processes in NPG and NPP are fundamentally more compliant due to the porosity that easily accommodates the imposed displacement. In the composite, internal constraints force a combined deformation of both phases bonded by the interface.

A more appropriate manner to evaluate a composite's response is to compare it with the bulk properties. As shown in both plots of Figure 7.7, the composite responses were between the range of the dotted lines representing the bulk gold and bulk epoxy properties. The values higher than the bulk epoxy confirm that the gold phase acted as the reinforcement in the NPG-polymer composite. Although the size effect can be observed, the NPG-epoxy composite responds as expected for reinforced materials. Therefore, the properties are in between the isostress and isostrain calculation. Importantly, in both analytical approaches, the volume fraction of gold needed to be adjusted by the effective relative density of the NPG, which deducted the dangling ligaments from the analysis.

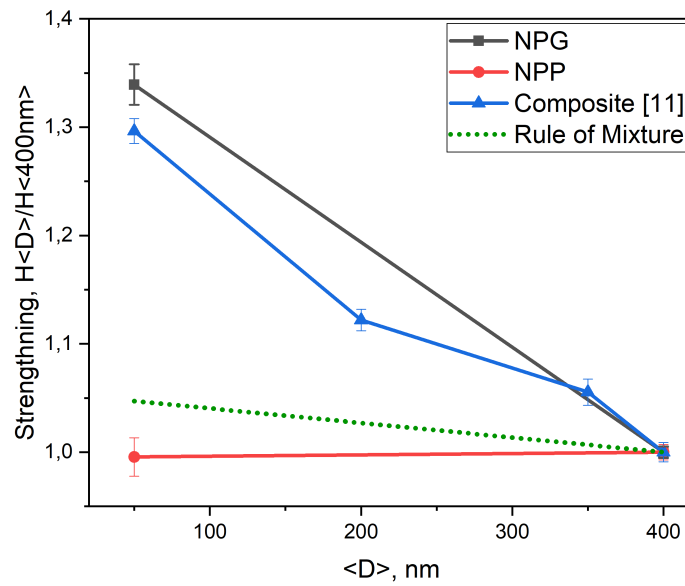


Figure 7.8: Structural length-scale strengthening compared with the response at $\langle D \rangle = 400 \text{ nm}$ for NPG, NPP, and NPG-epoxy samples. The dotted green line represents the rule of mixture calculated from the NPG properties and the effective volume fraction of gold. The error bars indicate one standard deviation about the mean value obtained by the division of uncertainties values.

The plot in Figure 7.8 further analyses the strengthening at small structural length scales. Here, the strengthening was calculated by dividing the hardness responses by the coarse structure's property (400 nm). The error bars indicate one standard deviation about the mean value obtained by the division of uncertainties values. Once again, the $\langle D \rangle$ of the NPP corresponds to the NPG ligament previous to the etching process. Therefore, NPG, NPP, and the NPG-epoxy composite can be compared. The comparison with bulk properties is not applicable here since the structural size effect is examined. In this case, the composite response is between the NPP and the NPG responses. Nevertheless, it is surprisingly high relative to the actual amount of NPG in the composite. A rule of mixture calculation is presented by the dotted green line using the NPG and NPP properties and their respective effective volume fraction. As it can be observed, the composite response is closer to the NPG boundary and considerably higher than the analytical calculation, which might be evidence that additional strengthening mechanisms in the composite deformation.

7.2.1 Considerations of the strengthening of the gold phase

In this section, the dislocation activity within the NPG ligaments, without the epoxy infiltration, was investigated by TEM microscopy. As described in Section 3.2.2, flat punch indentations were used to deform NPG structures with contrasting ligament sizes. Figure 7.9 shows TEM images of lamellae fabricated from deformed regions of NPG of average ligament

size of 20 nm (a) and (b), 50 nm (c) and (d) and 400 nm (e) and (f). To analyse the dislocation activity from the deformation process, it is necessary first to identify some particularities and artefacts of TEM microscopy in NPG samples.

First, it was found that the combination of the typical thickness of a lamella fabricated by FIB milling ($\approx 100\text{nm}$) and the gold's high-density complicate the imaging transparency process. Therefore, the analysis was limited in thickness to regions where the ligaments did not overlap, an obstacle common to other TEM investigations in NPG [1, 211–214]. Although HRTEM was only possible in fine NPG ligaments, the structure's tortuosity created thickness variation, which might affect the brightness uniformity. Blue arrows indicate examples in Figure 7.9 (a), (b) and (d), in which the ligament seems to bend over itself and overlap, and the thick regions appear in darkest contrast. The same artefact could be identified in the coarse structure shown in Figure 7.9 (e) and (f), in which only the central parts of the ligaments are visible in bright, and the thick nodes appear in black. Similarly, the Moiré fringes indicated by green arrows in Figure 7.9 (b) and (c) are associated with the overlapping of atomic layers [215]. Lastly, the presence of stacking-fault tetrahedra (STF) was found all over the ligaments and are indicated by red arrows in Figure 7.9 (a), (b), (c) and (d). In addition to the defects originated by plasticity, STF is typical artefacts of the ion-beam preparation of Au TEM samples already reported in bulk gold [216] and observed in other NPG investigations [213, 214].

The comparison between fine and coarse NPG reveals contrasting behaviour regarding the dislocation activity within the ligament structure. The 20 and 50 nm NPGs display eventual dislocations in the nodal region, which is likely a consequence of the ligament bending typical of the NPG deformation [1]. In contrast, dislocation activity can be easily observed in the central segment of the coarse ligaments. Even after deformation, the fine ligaments appear relatively free of dislocations which points to the dislocation starvation mechanisms on the strengthening of NPG. Therefore, the higher strength of fine NPG could be explained by the requirement of the continual dislocation nucleation, which contrasts with the pre-existing dislocations in the coarse structure.

Moreover, the dislocation activity is further investigated by comparing the dislocation configuration in ligaments of deformed and undeformed fine NPG structures. Figure 7.10 presents the HRTEM of undeformed ligaments in (a) and (c), while (b) and (d) show deformed ones. Red arrows indicate the stacking fault tetrahedra, characteristic of the sample preparation. Here, the physical aspect of the ligament surface with a free boundary is analysed. The surface of an undeformed ligament is shown in picture 7.10 (c). Although the surface is not perfectly straight as the ones fabricated by deposition techniques [217], it is relatively smooth, and no geometrical pattern can be identified.

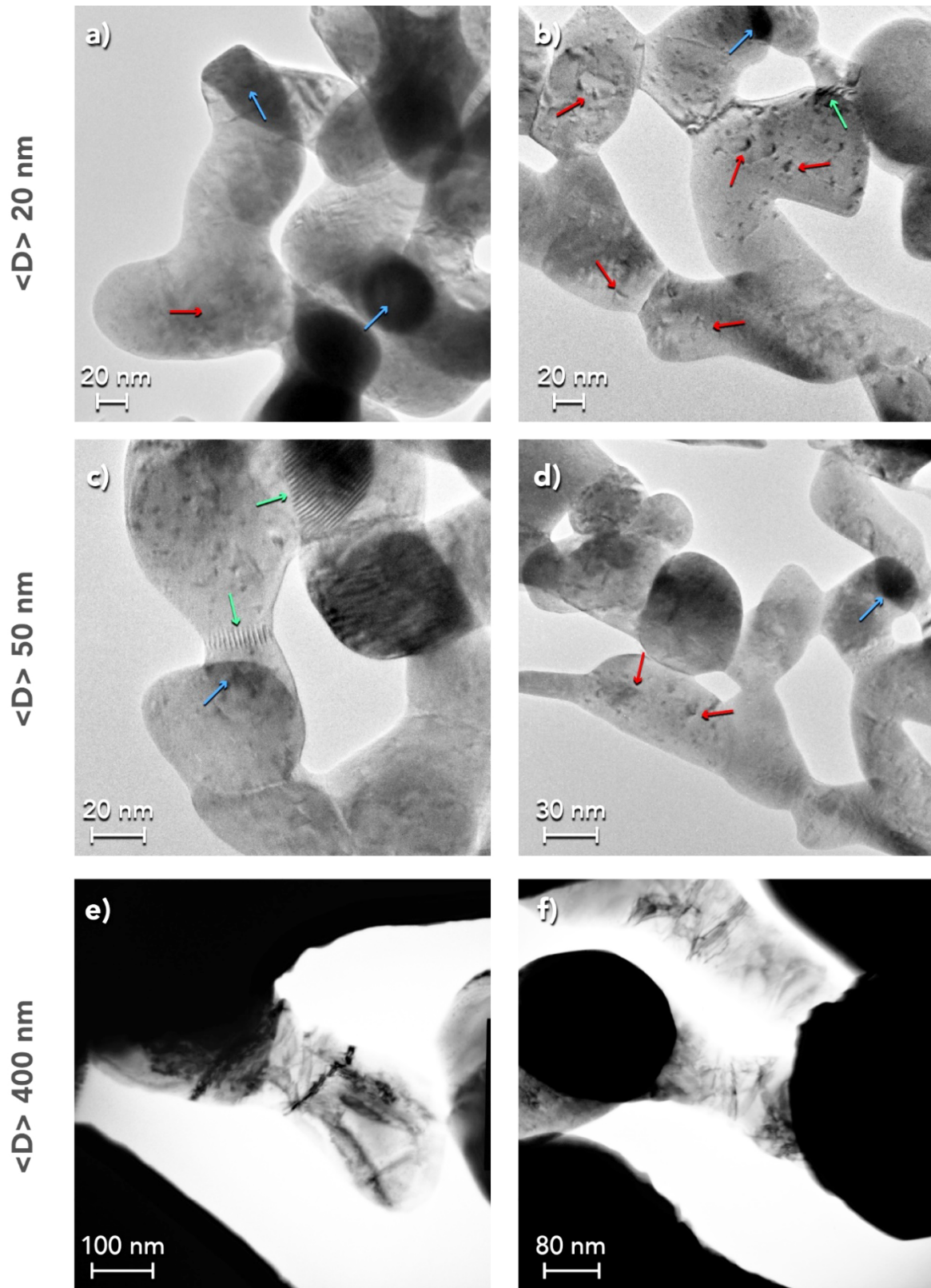


Figure 7.9: TEM micrographs showing the dislocation activity in deformed regions of NPG samples with $\langle D \rangle$ of 20 nm in (a) and (b), 50 nm in (c) and (d), and 400 nm in (e) and (f). The arrows show contrast disparities due to thickness variation (blue), Moiré fringes due to the overlapping of atomic layers (green) and stacking-fault likely due to the ion-beam irradiation from the sample preparation (red).

In contrast, a well-defined profile could be observed on the surface of deformed ligaments. Figure 7.10 (d) shows that a stepped staircase profile is easily identified. A similar pattern was observed during the in-situ deformation of sub-10 nm Au crystal, which attributed the primary carrier of the deformation in this system to the dislocation glide [218]. The escaping of the dislocation through the free surface creates slip steps associated with their Burgers vectors [219]. Figure 7.10 (e) shows an in-situ deformed microdog-bone of an Au single crystal showing the staircase profile taken from [218]. Additionally, the same profile was observed in the simulation of fracture behaviour of NPG using molecular dynamics [220]. The stepped pattern emerges from the accumulation of slip steps on the dislocation motion of atomic planes, which has a similar look to the aftermath of deformation in microcolumns by single slips [27].

The comparison presented in Figure 7.10 imply on dislocation activity involved in the deformation of the fine NPG, and the staircase profile on the surface indicates that the dislocations were able to emitted towards the free surface. Although this is strong evidence on the strengthening mechanism of NPG, questions arise regarding the behaviour in the NPG-polymer composites. In the composites, the dislocation interacts with the polymeric interface instead of a free surface. The implications of a boundary with a polymeric phase in the dislocation activity (propagation and nucleation) is unclear for the composite investigated here. Dislocation propagation occurs via glide, cross-slip, and climb, and many studies focused on the interaction with interfaces [221–224], thus in free surfaces, image forces act in the very vicinity to the interface driving the dislocations to emit towards free surfaces. In the case of a polymeric interface, it is expected the existence of similar forces driving the dislocation segments toward the softer material [224]. An example of dislocation interacting with a polymeric interface is given in the work of Ho Oh et al., in which the dislocations in Al films were able to emit towards a polyimide interface [219]. Therefore, the dislocation propagation required the breaking of the interface and rearrangement of the interfacial atoms. On the other hand, the dislocation nucleation is reasonable not altered since it usually takes place near a GPa regime [225, 226], which is well above the interfacial strength and yielding stress of the polymer phase.

The difference in the strengthening of NPG and NPG-polymer composites is that extrinsic mechanisms, i.e., size effects, can occur in the composite. The dislocation emission can only occur after breaking the interface to allow the polymer deformation at the vicinity to the interface and the formation of the staircase profile. In addition to other metal-polymer systems [219], interfacial strength would play an essential role in controlling the stability of interfacial dislocations. A weak interface would allow the interfacial atoms to slide freely and rearrange without the polymer substrate's influence. On the other hand, a stronger interface would restrict the sliding of interfacial atoms, which tend to pin dislocations near the interface, as observed in passivated surfaces [24, 219].

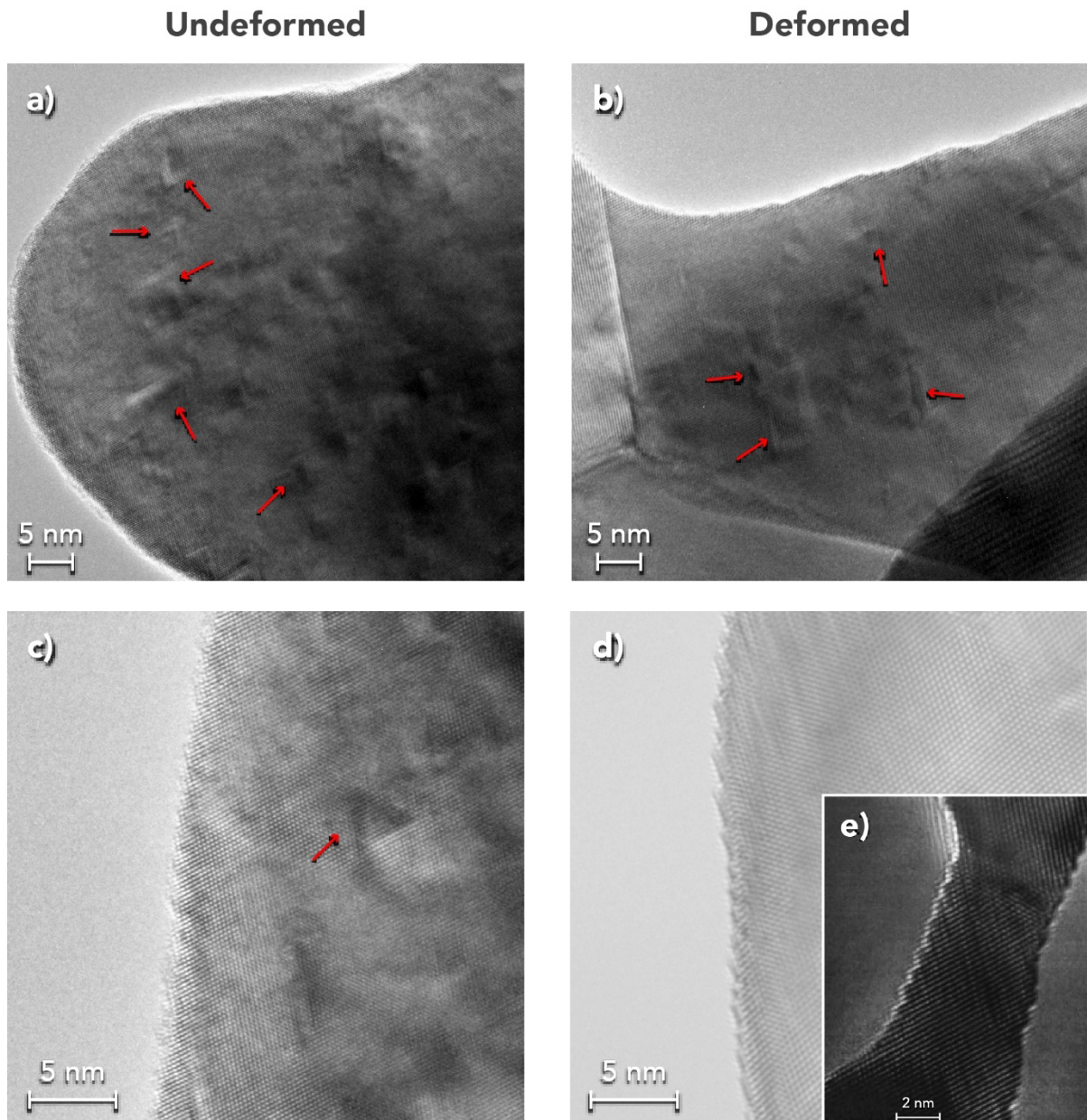


Figure 7.10: HRTEM micrographs showing undeformed NPG in (a) and (c) and deformed NPG in (b) and (d). The red arrows indicate stacking-fault likely due to the ion-beam irradiation from the sample preparation. Comparing the edge profile between (c) and (d) reinforces the staircase profile emerging from the rearrangement of interfacial atoms whenever dislocation emits towards the free surface. The same profile can be observed in the (e) showing an in-situ deformed microdog-bone of an Au single crystal, adapted from [218].

As shown in the previous chapter, gold and epoxy form a weak interface, which potentially activates mechanism related to the interfacial breaking and polymer deformation in the overall composite's response. Both mechanisms increase in effect with the increase of the interfacial area, which could explain the plot in Figure 7.8. Since the interfacial area is increased by reducing the average ligament size, it is expected that the strengthening would increase for smaller ligament

sizes, irrespective of the volume fraction of the Au phase. Here, a simplified analytical model is presented to evaluate the relation between the surface area and strengthening. First, the specific surface area of the NPG, taken from [227], was used as a reference for the interfacial area in the composites. Since it was observed that the hardness and specific surface areas, S_a , seems to follow a natural logarithm relation, the following relation is proposed:

$$\frac{H_{\langle D \rangle}}{H_{\langle 400 \rangle}} = \frac{\ln S_{a\langle D \rangle}}{\ln S_{a\langle 400 \rangle}} \quad (7.1)$$

where the strengthening is the ratio between the evaluated ligament and the coarse response ($\langle D \rangle = 400$ nm). A comparison of the experimentally measured hardness and the prediction from the analytical model on Eq. 7.1 is shown in Figure 7.11. As can be seen, there is a good agreement between the strengthening and the specific surface area, as an indicator of interfacial area, for the composite response.

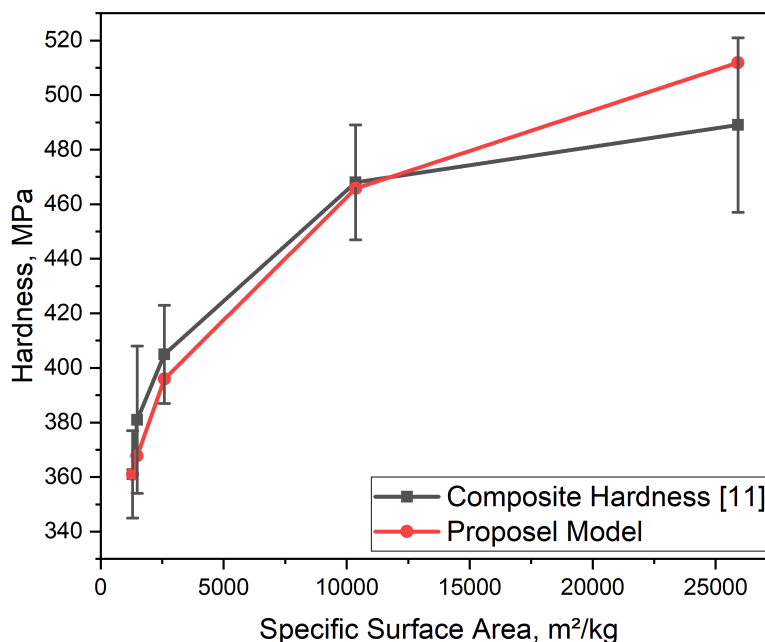


Figure 7.11: Hardness response versus the specific surface area for the NPG-epoxy composite. The red line corresponds to the analytical model proposed in this thesis based on the natural logarithm presented in Equation 7.1.

7.3 Conclusions

This chapter analysed the overall mechanical response of NPG-epoxy composites based on the findings from the previous chapters, including the interfacial characteristics from Chapter 5 and the interfacial properties of Chapter 6. The simulation work presented here showed the contribution of the constituent phases' properties and the interface on the composite deformation under compression. The interfacial strength measured experimentally is weak enough so that the interface fails ultimately on the entire composite. The extrapolation of the simulation parameters showed that in strong interface composites, the interface remains partially bonded after the polymer yield activation, which increases the composite constraints. Nevertheless, the interconnected composite structure allowed the phases to transfer load in both cases, which reduced the potential to tailor the composite strength based on controlling the interfacial property. Even though the interface was the weakest link in the deformation, the composite behaviour under compression was strongly dependent on the polymer deformation constrained by the Au ligament structure.

Moreover, the mechanical properties of NPG-epoxy composite were evaluated against the individual response of each constituent phase. It was found that hardness and elastic response behaved as expected for composite materials, with the composite response in between the responses of reinforcement and matrix phases. The composite's strengthening was attenuated compared to the NPG alone, but it is much higher than the expected strengthening considering the correspondent volume fraction. This finding motivated an investigation on the mechanics behind the strengthening in NPG-epoxy composites. The observation of the dislocation activity by TEM imaging of deformed NPG ligaments with contrasting sizes points to starvation mechanism in small ligaments. It was found evidence showing the emission of dislocations to the free surface, forming a staircase profile on the ligaments' surface. The same process in the composite would necessarily imply breaking the interface and local deformation of the polymer phases, which could explain the disproportional strengthening found in the NPG-epoxy composites. This idea is further supported by the correlation between the specific surface area of the samples with the respective increase in hardness results.

8 Summary and future work

8.1 Summary

The NPG-polymer composite was studied in this thesis by independently investigating each of the factors that build up its mechanical response, focusing on the reinforcement phase, i.e., the interconnected Au ligament network, the matrix, i.e., the continuous polymer structure, and the interface's capacity to transfer load between the phases. A set of strategies were developed to isolate the contribution and effect of each element. This included mechanical characterization of the polymer phase, potential size effects therein; characterization of the interfacial strength, investigation of possible interphase; and the evaluation of the composite as a whole as was achieved using FEM (finite element method). Ultimately, the findings were able to address the overarching questions posed in Chapter 1:

How do the small length-scales affect the properties of the polymeric phase within the composite structure?

The polymer phase within the composites assumes an interconnected structure with a sub-micron structural length scale. Here, nanoporous polymer (NPP) structures were fabricated for the first time, exploring mining etching technologies adapted to NPG-epoxy composites. The separation of the polymer phase allowed the investigation of the composite structure's effect without the contribution of the Au phase. It was found no evidence supporting the influence of the structure size in the elastic or plastic response, and the modulus of the NPP structures could be well predicted by an isostrain law applied to the modulus measured on bulk epoxy using the corresponding volume fraction. Therefore, differently from the NPG, the polymer phase does not show the strengthening potential at smaller structural length scales, and its contribution is mainly as the composite's matrix to improve stress distribution during loading.

How does a gold-polymer interface affect the nearby local mechanical characteristics?

No evidence was found supporting the presence of an interlayer between gold and epoxy in the interfaces of NPG-epoxy composites investigated in this work. For the examined length scales, both materials could still be assumed as a continuous solid with a sharp interface, which circumvents the implications of a geometrically undefined polymeric interphase. Mechanical characterization with nanoindentations shows no evidence supporting the interface affecting the transitional properties in an inclined interfacial sample. The lack of interphase simplified the subsequent evaluation of the complex composite structure as a whole.

How does the bonding strength affect the interfacial behaviour?

The interfacial behaviour of the gold-epoxy interfaces was investigated experimentally using a shear-based method, which allowed for a systematic experimental investigation throughout the microcompression of bi-material microcolumns with an inclined interface. The characteristic interfacial strength is 45 MPa, which was not dependent on the interfacial area but decreased significantly with interfacial defects. These experimental findings were used to develop a modelling approach of the interfaces based on a finite element method, which systematically evaluated the bonding strength's effect in the interfacial behaviour of the interfacial shear strength testing. The interfacial behaviour was found to balance the bonding strength, the properties of the underlying materials, and the stress distribution as dictated by the morphology of the two phases.

What is the influence of the interface properties in NPG-epoxy composites?

The influence of the interfacial properties in the NPG-epoxy composites was investigated by finite element analysis (FEA) and supported by the interpretation of experimental results. The simulations considering the interfacial strength measured experimentally was weak enough so that the interface failed ultimately on the entire composite structure. Additionally, the delamination process could be correlated with the experimental observation of highly deformed composite regions. The extrapolation of the interfacial properties showed that the phases remain partially bonded in a composite with a strong interface. Nevertheless, the potential to tailor the composite yielding was limited by the polymer yield strength. Overall, the composite's yielding depends on the polymer deformation constrained by the Au ligament structure. Nevertheless, the interfacial property could play a role in the strengthening of the composite at small structural length scales, since the starvation mechanism active in nano-scale NPG ligaments depends on the ability of dislocations to be emitted at a free-surface, which requires the local rupture of the interface and deformation in the polymer phase.

8.2 Suggestions for future work

The work developed in this thesis revealed the potential for further investigations:

Exploiting Fabrication

- The processing of NPP structures opened many possibilities for fabricating novel materials. The NPG ligament structure could be infiltrated with functional polymers, which would create functional NPP with an adjustable open porous size.
- The NPG could be coated by a controlled polymerization. After the Au etching, a polymeric tubes structure would be fabricated in a tailorable sub-micron scale.
- The open porosity of NPP could be further infiltrated, creating other bicontinuous composites. The characterization of these structures would clarify the effect of the structural length-scale in other polymer materials and even allow new applications for functional nanostructured polymers.

Modelling

- The interfacial modelling could be utilized on a simplified representation of the NPG-epoxy composites, which would allow for simulation volumes closer to the RV of the structure. Many studies utilize FE beam and level-cut Gaussian random field approaches on the micromechanical modelling of nanoporous metals. The surface-based cohesive behaviour could be incorporated in these models, which would provide the effect of the interfacial strength concerning the structural parameters and load-bearing structure of the NPG composites.

Mechanisms of deformation

- The investigation of the dislocation activity within the ligament structure of fine NPG could be facilitated by processing the lamellae's techniques that do not generate defects in the analysed surfaces. Circumventing the formation of stacking-fault due to the ion-beam irradiation would allow for a more reliable interpretation of the observed dislocations activity.
- Recent advances in the transmission electron microscopy of polymers could be used to investigate the interfacial rearrangements during the dislocation emission.

Bibliography

1. Dou, R., Derby, B.: Deformation mechanisms in gold nanowires and nanoporous gold. *Philos. Mag.* 91, 7–9 (2011). <https://doi.org/10.1080/14786435.2010.481271>
2. Farkas, D., Caro, A., Bringa, E., Crowson, D.: Mechanical response of nanoporous gold. *Acta Mater.* 61, 3249–3256 (2013). <https://doi.org/10.1016/j.actamat.2013.02.013>
3. Huber, N., Viswanath, R.N., Mameka, N., Markmann, J., Weißmüller, J.: Scaling laws of nanoporous metals under uniaxial compression. *Acta Mater.* (2014). <https://doi.org/10.1016/j.actamat.2013.12.003>
4. Lilleodden, E.T., Voorhees, P.W.: On the topological, morphological, and microstructural characterization of nanoporous metals. *MRS Bull.* 43, 20–26 (2018). <https://doi.org/10.1557/mrs.2017.303>
5. Weissmüller, J.: Charge-Induced Reversible Strain in a Metal. *Science* (80-.). 300, 312–315 (2003). <https://doi.org/10.1126/science.1081024>
6. Biener, J., Wittstock, A., Zepeda-Ruiz, L.A., Biener, M.M., Zielasek, V., Kramer, D., Viswanath, R.N., Weissmüller, J., Bäumer, M., Hamza, A. V: Surface-chemistry-driven actuation in nanoporous gold. *Nat. Mater.* 8, (2008). <https://doi.org/10.1038/NMAT2335>
7. Ding, Y., Chen, M.: Nanoporous Metals for Catalytic and Optical Applications. <https://doi.org/10.1557/mrs2009.156>
8. Wang, K., Kobler, A., Kübel, C., Jelitto, H., Schneider, G., Weissmüller, J.: Nanoporous-gold-based composites: toward tensile ductility. *NPG Asia Mater.* 7, 187 (2015). <https://doi.org/10.1038/am.2015.58>
9. Wang, K., Kobler, A., Kübel, C., Jelitto, H., Schneider, G., Weissmüller, J.: Nanoporous-gold-based composites: toward tensile ductility. *NPG Asia Mater.* 7, 187 (2015). <https://doi.org/10.1038/am.2015.58>
10. Griffiths, E., Bargmann, S., Reddy, B.D.: Elastic behaviour at the nanoscale of innovative composites of nanoporous gold and polymer. *Extrem. Mech. Lett.* 17, 16–23 (2017). <https://doi.org/10.1016/j.eml.2017.09.006>
11. Hu, K.: Three-Dimensional Microstructural and Micromechanical Characterization of Nanoporous Gold – Epoxy Composites , TUHH PhD Thesis, (2016)
12. Mameka, N., Wang, K., Markmann, J., Lilleodden, E.T., Weissmüller, J.: Nanoporous gold—testing macro-scale samples to probe small-scale mechanical behavior. *Mater. Res. Lett.* 4, 27–36 (2016). <https://doi.org/10.1080/21663831.2015.1094679>

13. Kumar, P.S., Ramachandra, S., Ramamurty, U.: Effect of displacement-rate on the indentation behavior of an aluminum foam. *Mater. Sci. Eng. A.* 347, 330–337 (2003). [https://doi.org/10.1016/S0921-5093\(02\)00608-1](https://doi.org/10.1016/S0921-5093(02)00608-1)
14. Jin, H.-J., Kurmanaeva, L., Schmauch, J., Rösner, H., Ivanisenko, Y., Weissmüller, J.: Deforming nanoporous metal: Role of lattice coherency. *Acta Mater.* 57, 2665–2672 (2009). <https://doi.org/10.1016/j.actamat.2009.02.017>
15. Wang, K., Weissmüller, J.: Composites of Nanoporous Gold and Polymer. *Adv. Mater.* 25, 1280–1284 (2013). <https://doi.org/10.1002/adma.201203740>
16. Jin, H.J., Weissmüller, J.: A material with electrically tunable strength and flow stress. *Science (80-.)*. 332, 1179–1182 (2011). <https://doi.org/10.1126/science.1202190>
17. Balk, T.J., Eberl, C., Sun, Y., Hemker, K.J., Gianola, D.S.: Tensile and compressive microspecimen testing of bulk nanoporous gold. *JOM.* 61, 26–31 (2009). <https://doi.org/10.1007/s11837-009-0176-6>
18. Badwe, N., Chen, X., Sieradzki, K.: Mechanical properties of nanoporous gold in tension. *Acta Mater.* 129, 251–258 (2017). <https://doi.org/10.1016/j.actamat.2017.02.040>
19. Mameka, N., Wang, K., Markmann, J., Lilleodden, E.T., Weissmüller, J.: Nanoporous Gold-Testing Macro-scale Samples to Probe Small-scale Mechanical Behavior. *Mater. Res. Lett.* 4, 27–36 (2016). <https://doi.org/10.1080/21663831.2015.1094679>
20. Griffiths, E., Bargmann, S., Reddy, B.D.: Elastic behaviour at the nanoscale of innovative composites of nanoporous gold and polymer. *Extrem. Mech. Lett.* 17, 16–23 (2017). <https://doi.org/10.1016/j.eml.2017.09.006>
21. Griffiths, E., Soyarslan, C., Bargmann, S., Reddy, B.D.: Insights into fracture mechanisms in nanoporous gold and polymer impregnated nanoporous gold. *Extrem. Mech. Lett.* 39, 100815 (2020). <https://doi.org/10.1016/j.eml.2020.100815>
22. Griffiths, E., Wilmers, J., Bargmann, S., Reddy, B.D.: Nanoporous metal based composites: Giving polymers strength and making metals move. *J. Mech. Phys. Solids.* 137, 103848 (2020). <https://doi.org/10.1016/j.jmps.2019.103848>
23. Thompson, C.V.: The yield stress of polycrystalline thin films. *J. Mater. Res.* 8, 237–238 (1993). <https://doi.org/10.1557/JMR.1993.0237>
24. Keller, R.-M., Baker, S.P., Arzt, E.: Quantitative analysis of strengthening mechanisms in thin Cu films: Effects of film thickness, grain size, and passivation. *J. Mater. Res.* 13, 1307–1317 (1998). <https://doi.org/10.1557/JMR.1998.0186>
25. Nix, W.D.: Yielding and strain hardening of thin metal films on substrates. *Scr. Mater.* 39, 545–554 (1998). [https://doi.org/10.1016/S1359-6462\(98\)00195-X](https://doi.org/10.1016/S1359-6462(98)00195-X)
26. Nix, W.D., Greer, J.R., Feng, G., Lilleodden, E.T.: Deformation at the nanometer and micrometer length scales: Effects of strain gradients and dislocation starvation. *Thin Solid Films.* (2007). <https://doi.org/10.1016/j.tsf.2006.01.030>
27. Volkert, C.A., Lilleodden, E.T.: Size effects in the deformation of sub-micron Au columns. *Philos. Mag.* 86, 33–35 (2006). <https://doi.org/10.1080/14786430600567739>
28. Norfleet, D.M., Dimiduk, D.M., Polasik, S.J., Uchic, M.D., Mills, M.J.: Dislocation structures and their relationship to strength in deformed nickel microcrystals. *Acta Mater.*

- 56, 2988–3001 (2008). <https://doi.org/10.1016/j.actamat.2008.02.046>
29. Mangipudi, K.R., Epler, E., Volkert, C.A.: Morphological similarity and structure-dependent scaling laws of nanoporous gold from different synthesis methods. *Acta Mater.* 140, 337–343 (2017). <https://doi.org/10.1016/j.actamat.2017.08.039>
 30. Huber, N., Viswanath, R.N., Mameka, N., Markmann, J., Weißmüller, J.: Scaling laws of nanoporous metals under uniaxial compression. *Acta Mater.* 67, 252–265 (2014). <https://doi.org/10.1016/j.actamat.2013.12.003>
 31. Biener, J., Hamza, A.V., Hodge, A.M.: Deformation Behavior of Nanoporous Metals. In: *Micro and Nano Mechanical Testing of Materials and Devices*. pp. 118–135. Springer US, Boston, MA (2008)
 32. Biener, J., Hodge, A.M., Hayes, J.R., Volkert, C.A., Zepeda-Ruiz, L.A., Hamza, A. V., Abraham, F.F.: Size Effects on the Mechanical Behavior of Nanoporous Au. *Nano Lett.* 6, 2379–2382 (2006). <https://doi.org/10.1021/nl061978i>
 33. Dou, R., Derby, B.: Strain gradients and the strength of nanoporous gold. *J. Mater. Res.* 25, 746–753 (2010). <https://doi.org/10.1557/JMR.2010.0099>
 34. Samaee, V., Gatti, R., Devincre, B., Pardoën, T., Schryvers, D., Idrissi, H.: Dislocation driven nanosample plasticity: new insights from quantitative in-situ TEM tensile testing. *Sci. Rep.* 8, 12012 (2018). <https://doi.org/10.1038/s41598-018-30639-8>
 35. Samaee, V., Sandfeld, S., Idrissi, H., Groten, J., Pardoën, T., Schwaiger, R., Schryvers, D.: Dislocation structures and the role of grain boundaries in cyclically deformed Ni micropillars. *Mater. Sci. Eng. A.* 769, 138295 (2020). <https://doi.org/10.1016/j.msea.2019.138295>
 36. Lam, D.C.C., Chong, A.C.M.: Effect of cross-link density on strain gradient plasticity in epoxy. *Mater. Sci. Eng. A.* 281, 156–161 (2000). [https://doi.org/10.1016/s0921-5093\(99\)00724-8](https://doi.org/10.1016/s0921-5093(99)00724-8)
 37. Lam, D.C.C., Yang, F., Chong, A.C.M., Wang, J., Tong, P.: Experiments and theory in strain gradient elasticity. *J. Mech. Phys. Solids.* 51, 1477–1508 (2003). [https://doi.org/10.1016/S0022-5096\(03\)00053-X](https://doi.org/10.1016/S0022-5096(03)00053-X)
 38. Chong, A.C.M., Lam, D.C.C.: Strain gradient plasticity effect in indentation hardness of polymers. *J. Mater. Res.* 14, 4103–4110 (1999). <https://doi.org/10.1557/JMR.1999.0554>
 39. Lam, D.C.C., Chong, A.C.M.: Characterization and modeling of specific strain gradient modulus of epoxy. *J. Mater. Res.* 16, 558–563 (2001). <https://doi.org/10.1557/JMR.2001.0080>
 40. Alisafaei, F., Han, C.S., Lakhera, N.: Characterization of indentation size effects in epoxy. *Polym. Test.* 40, 70–78 (2014). <https://doi.org/10.1016/j.polymertesting.2014.08.012>
 41. Dutta, A.K., Penumadu, D., Files, B.: Nanoindentation testing for evaluating modulus and hardness of single-walled carbon nanotube–reinforced epoxy composites. *J. Mater. Res.* 19, 158–164 (2004). <https://doi.org/10.1557/jmr.2004.19.1.158>
 42. Sánchez, M., Rams, J., Campo, M., Jiménez-Suárez, A., Ureña, A.: Characterization of carbon nanofiber/epoxy nanocomposites by the nanoindentation technique. *Compos. Part B Eng.* 42, 638–644 (2011). <https://doi.org/10.1016/j.compositesb.2011.02.017>

43. Briscoe, B.J., Fiori, L., Pelillo, E.: Nano-indentation of polymeric surfaces. *J. Phys. D. Appl. Phys.* 31, 2395–2405 (1998). <https://doi.org/10.1088/0022-3727/31/19/006>
44. Baltá Calleja, F.J., Flores, A., Michler, G.H.: Microindentation studies at the near surface of glassy polymers: Influence of molecular weight. *J. Appl. Polym. Sci.* 93, 1951–1956 (2004). <https://doi.org/10.1002/app.20665>
45. Mcfarland, A.W., Poggi, M.A., Bottomley, L.A.: Role of material microstructure in plate stiffness with relevance to microcantilever sensors Related content Characterization of microcantilevers. *J. Micromechanics Microengineering.* (2005). <https://doi.org/10.1088/0960-1317/15/5/024>
46. Voyiadjis, G.Z., Shojaei, A., Mozaffari, N.: Strain gradient plasticity for amorphous and crystalline polymers with application to micro- and nano-scale deformation analysis. *Polymer (Guildf).* 55, 4182–4198 (2014). <https://doi.org/10.1016/j.polymer.2014.06.015>
47. Lu, Y.C., Jones, D.C., Tandon, G.P., Putthanarat, S., Schoeppner, G.A.: High Temperature Nanoindentation of PMR-15 Polyimide. <https://doi.org/10.1007/s11340-009-9254-5>
48. Charitidis, C.: Nanoscale Deformation and Nanomechanical Properties of Soft Matter Study Cases: Polydimethylsiloxane, Cells and Tissues. *ISRN Nanotechnol.* 2011, 1–13 (2011). <https://doi.org/10.5402/2011/719512>
49. Charitidis, C.A.: Nanoscale Deformation and Nanomechanical Properties of Polydimethylsiloxane (PDMS). *Ind. Eng. Chem. Res.* 50, 565–570 (2011). <https://doi.org/10.1021/ie100099g>
50. Koumoulos, E.P., Jagdale, P., Kartsonakis, I.A., Giorcelli, M., Tagliaferro, A., Charitidis, C.A.: Carbon nanotube/polymer nanocomposites: A study on mechanical integrity through nanoindentation. *Polym. Compos.* 36, 1432–1446 (2015). <https://doi.org/10.1002/pc.23049>
51. Alisafaei, F., Han, C.-S.: Indentation Depth Dependent Mechanical Behavior in Polymers. (2015). <https://doi.org/10.1155/2015/391579>
52. Lim, Y.Y., Munawar Chaudhri, M.: Indentation of elastic solids with a rigid Vickers pyramidal indenter. *Mech. Mater.* 38, 1213–1228 (2006). <https://doi.org/10.1016/j.mechmat.2006.04.006>
53. Alisafaei, F., Han, C.S., Sanei, S.H.R.: On the time and indentation depth dependence of hardness, dissipation and stiffness in polydimethylsiloxane. *Polym. Test.* 32, 1220–1228 (2013). <https://doi.org/10.1016/j.polymertesting.2013.07.013>
54. Nikolov, S., Han, C.S., Raabe, D.: On the origin of size effects in small-strain elasticity of solid polymers. *Int. J. Solids Struct.* 44, 1582–1592 (2007). <https://doi.org/10.1016/j.ijsolstr.2006.06.039>
55. Swaddiwudhipong, S., Poh, L.H., Hua, J., Liu, Z.S., Tho, K.K.: Modeling nano-indentation tests of glassy polymers using finite elements with strain gradient plasticity. *Mater. Sci. Eng. A.* 404, 179–187 (2005). <https://doi.org/10.1016/j.msea.2005.05.063>
56. Zhang, T.-Y., Xu, W.-H.: Surface Effects on Nanoindentation. *J. Mater. Res.* 17, 1715–1720 (2002). <https://doi.org/10.1557/JMR.2002.0254>
57. Zhang, T.Y., Xu, W.H., Zhao, M.H.: The role of plastic deformation of rough surfaces in the size-dependent hardness. *Acta Mater.* 52, 57–68 (2004).

- <https://doi.org/10.1016/j.actamat.2003.08.026>
58. Han, C.-S., Nikolov, S.: Indentation size effects in polymers and related rotation gradients. *J. Mater. Res.* 22, 1662–1672 (2007). <https://doi.org/10.1557/JMR.2007.0197>
 59. Lee, L.H.: Molecular bonding and adhesion at polymer-metal interphases. *J. Adhes.* 46, 15–38 (1994). <https://doi.org/10.1080/00218469408026646>
 60. Müller, M.: Polymers at Interfaces and Surfaces and in Confined Geometries. In: *Polymer Science: A Comprehensive Reference*. pp. 387–416. Elsevier (2012)
 61. Wake, W.: *Adhesion and the formulation of adhesives*. Applied Science, London (1976)
 62. Durell, M., Macdonald, J.E., Trolley, D., Wehrum, A., Jukes, P.C., Jones, R.A.L., Walker, C.J., Brown, S.: The role of surface-induced ordering in the crystallisation of PET films. *Europhys. Lett.* 58, 844–850 (2002). <https://doi.org/10.1209/epl/i2002-00451-1>
 63. Nter Reiter, G., Sharma, A., Casoli, A., David, M.-O., Khanna, R., Auroy, P.: Thin Film Instability Induced by Long-Range Forces. (1999). <https://doi.org/10.1021/la981470y>
 64. Aufray Æ, M., Andre, A.: Epoxy–amine/metal interphases: Influences from sharp needle-like crystal formation. *Int. J. Adhes. Adhes.* 27, 387–393 (2007). <https://doi.org/10.1016/j.ijadhadh.2006.09.009>
 65. Roche, A.A., Bouchet, J., Bentadjine, S.: Formation of epoxy-diamine/metal interphases. *Int. J. Adhes. Adhes.* 22, 431–441 (2002). [https://doi.org/10.1016/S0143-7496\(02\)00021-0](https://doi.org/10.1016/S0143-7496(02)00021-0)
 66. Palmese, G.R., McCullough, R.L.: Effect of epoxy–amine stoichiometry on cured resin material properties. *J. Appl. Polym. Sci.* 46, 1863–1873 (1992). <https://doi.org/10.1002/app.1992.070461018>
 67. Edwin P. Plueddemann: *Interfaces in Polymer Matrix Composites*. Academic Press (1974)
 68. Putz, B., Milassin, G., Butenko, Y., Völker, B., Gammer, C., Semprimoschnig, C., Cordill, M.J.: Interfacial mutations in the Al-polyimide system. *Surf. Interface Anal.* 50, 579–586 (2018). <https://doi.org/10.1002/sia.6434>
 69. Guglielmi, P.O., Blaese, D., Hablitzel, M.P., Nunes, G.F., Lauth, V.R., Hotza, D., Al-Qureshi, H.A., Janssen, R.: Microstructure and flexural properties of multilayered fiber-reinforced oxide composites fabricated by a novel lamination route. *Ceram. Int.* 41, 7836–7846 (2015). <https://doi.org/10.1016/j.ceramint.2015.02.120>
 70. Blaese, D., Garcia, D.E., Guglielmi, P., Hotza, D., Fredel, M.C., Janssen, R.: ZrO₂ fiber-matrix interfaces in alumina fiber-reinforced model composites. *J. Eur. Ceram. Soc.* 35, 1593–1598 (2015). <https://doi.org/10.1016/j.jeurceramsoc.2014.10.027>
 71. Hablitzel, M.P., Garcia, D.E., Hotza, D.: Weak interfaces in alumina/alumina CMCS. *Matéria (Rio Janeiro)*. 16, 788–794 (2011). <https://doi.org/10.1590/S1517-70762011000300006>
 72. Kardos, J.L.: The Role of the Interface in Polymer Composites — Some Myths, Mechanisms, and Modifications. In: *Molecular Characterization of Composite Interfaces*. Springer Berlin Heidelberg, Berlin, Heidelberg (1985)
 73. Cox, H.L.: The elasticity and strength of paper and other fibrous materials. *Br. J. Appl. Phys.* 3, 72–79 (1952). <https://doi.org/10.1088/0508-3443/3/3/302>

74. Fukuda, H., Chou, T.-W.: An Advanced Shear-Lag Model Applicable to Discontinuous Fiber Composites. *J. Compos. Mater.* 15, 79–91 (1981). <https://doi.org/10.1177/002199838101500107>
75. Mondali, M., Abedian, A., Ghavami, A.: A new analytical shear-lag based model for prediction of the steady state creep deformations of some short fiber composites. *Mater. Des.* 30, 1075–1084 (2009). <https://doi.org/10.1016/j.matdes.2008.06.039>
76. Verpoest, I., Desaegeer, M., Ivens, J., Wevers, M.: Interfaces in polymer matrix composites from micromechanical tests to macromechanical properties. *Makromol. Chemie. Macromol. Symp.* 75, 85–98 (1993). <https://doi.org/10.1002/masy.19930750109>
77. T.W.Chou: Structure and Properties of Composites. In: *Materials Science and Technology*. Wiley-VCH, New York (1993)
78. Hodzic, A., Stachurski, Z., Kim, J.: Nano-indentation of polymer–glass interfaces Part I. Experimental and mechanical analysis. *Polymer (Guildf)*. 41, 6895–6905 (2000). [https://doi.org/10.1016/S0032-3861\(99\)00890-3](https://doi.org/10.1016/S0032-3861(99)00890-3)
79. Hodzic, A., Kim, J., Stachurski, Z.: Nano-indentation and nano-scratch of polymer/glass interfaces. II: model of interphases in water aged composite materials. *Polymer (Guildf)*. 42, 5701–5710 (2001). [https://doi.org/10.1016/S0032-3861\(01\)00029-5](https://doi.org/10.1016/S0032-3861(01)00029-5)
80. Schöneich, M., Zamanzade, M., Stommel, M.: Fiber-matrix interphase in applied short glass fiber composites determined by a nano-scratch method. *Compos. Sci. Technol.* 119, 100–107 (2015). <https://doi.org/10.1016/j.compscitech.2015.10.004>
81. Fuentes, C.A., Brughmans, G., Tran, L.Q.N., Dupont-Gillain, C., Verpoest, I., Van Vuure, A.W.: Mechanical behaviour and practical adhesion at a bamboo composite interface: Physical adhesion and mechanical interlocking. *Compos. Sci. Technol.* 109, 40–47 (2015). <https://doi.org/10.1016/j.compscitech.2015.01.013>
82. DiFrancia, C., Ward, T.C., Claus, R.O.: The single-fibre pull-out test. 1: Review and interpretation. *Compos. Part A Appl. Sci. Manuf.* 27, 597–612 (1996). [https://doi.org/10.1016/1359-835X\(95\)00069-E](https://doi.org/10.1016/1359-835X(95)00069-E)
83. Teklal, F., Djebbar, A., Allaoui, S., Hivet, G., Joliff, Y., Kacimi, B.: A review of analytical models to describe pull-out behavior – Fiber/matrix adhesion. *Compos. Struct.* 201, 791–815 (2018). <https://doi.org/10.1016/j.compstruct.2018.06.091>
84. Lin, F., Du, X., Li, W., Jiang, J., Chen, N.: Interfacial properties of high failure strain polyimide fiber/epoxy composites analyzed by a modified single fiber fragmentation test. *Appl. Surf. Sci.* 513, 145869 (2020). <https://doi.org/10.1016/j.apsusc.2020.145869>
85. Zhao, Z., Teng, K., Li, N., Li, X., Xu, Z., Chen, L., Niu, J., Fu, H., Zhao, L., Liu, Y.: Mechanical, thermal and interfacial performances of carbon fiber reinforced composites flavored by carbon nanotube in matrix/interface. *Compos. Struct.* 159, 761–772 (2017). <https://doi.org/10.1016/j.compstruct.2016.10.022>
86. Tang, Y., Ye, L., Zhang, D., Deng, S.: Characterization of transverse tensile, interlaminar shear and interlaminar fracture in CF/EP laminates with 10wt% and 20wt% silica nanoparticles in matrix resins. *Compos. Part A Appl. Sci. Manuf.* 42, 1943–1950 (2011). <https://doi.org/10.1016/j.compositesa.2011.08.019>
87. Shin, H.-S., Gorospe, A.: Characterization of transverse tensile stress response of critical current and delamination behaviour in GdBCO coated conductor tapes by anvil test.

- Supercond. Sci. Technol. 27, 025001 (2014). <https://doi.org/10.1088/0953-2048/27/2/025001>
88. Cai, X.J., Xu, J.Q.: Interfacial fracture criteria based on the nominal deformation energy of interface. *Theor. Appl. Fract. Mech.* 75, 16–21 (2015). <https://doi.org/10.1016/j.tafmec.2014.10.008>
89. Koyanagi, J., Nakatani, H., Ogihara, S.: Comparison of glass-epoxy interface strengths examined by cruciform specimen and single-fiber pull-out tests under combined stress state. *Compos. Part A Appl. Sci. Manuf.* 43, 1819–1827 (2012). <https://doi.org/10.1016/j.compositesa.2012.06.018>
90. Ogihara, S., Koyanagi, J.: Investigation of combined stress state failure criterion for glass fiber/epoxy interface by the cruciform specimen method. *Compos. Sci. Technol.* 70, 143–150 (2010). <https://doi.org/10.1016/j.compscitech.2009.10.002>
91. Ogihara, S., Sakamoto, Y., Kato, H.: Evaluation of glass fiber/epoxy interfacial strength using a cruciform specimen. *ICCM Int. Conf. Compos. Mater.* (2007)
92. Lin, G., Geubelle, P.H., Sottos, N.R.: Simulation of fiber debonding with friction in a model composite pushout test. *Int. J. Solids Struct.* 38, 8547–8562 (2001). [https://doi.org/10.1016/S0020-7683\(01\)00085-3](https://doi.org/10.1016/S0020-7683(01)00085-3)
93. Tan, W., Naya, F., Yang, L., Chang, T., Falzon, B.G., Zhan, L., Molina-Aldareguía, J.M., González, C., Llorca, J.: The role of interfacial properties on the intralaminar and interlaminar damage behaviour of unidirectional composite laminates: Experimental characterization and multiscale modelling. *Compos. Part B Eng.* 138, 206–221 (2018). <https://doi.org/10.1016/j.compositesb.2017.11.043>
94. Kenyon, A.S., Duffey, H.J.: Properties of a particulate-filled polymer. *Polym. Eng. Sci.* 7, 189–193 (1967). <https://doi.org/10.1002/pen.760070311>
95. Kenyon, A.: Role of the interface in glass-epoxy composites. *J. Colloid Interface Sci.* 27, 761–771 (1968). [https://doi.org/10.1016/0021-9797\(68\)90110-0](https://doi.org/10.1016/0021-9797(68)90110-0)
96. Kardos, J.L.: Structure property relations in short-fiber reinforced plastics. *C R C Crit. Rev. Solid State Sci.* 3, 419–450 (1973). <https://doi.org/10.1080/10408437308244870>
97. Wang, K., Weissmüller, J.: Composites of nanoporous gold and polymer. *Adv. Mater.* (2013). <https://doi.org/10.1002/adma.201203740>
98. Wang, K.: Composites of Nanoporous Gold and Polymer, TUHH PhD Thesis, (2015)
99. Hablitzel, M.P., Lilleodden, E.T.: On measuring the independent mechanical response of the polymer phase from nanoporous gold polymer composites. *Scr. Mater.* 170, 67–70 (2019). <https://doi.org/10.1016/j.scriptamat.2019.04.026>
100. Green, T.A.: Gold etching for microfabrication. (2014). <https://doi.org/10.1007/s13404-014-0143-z>
101. Abbott, N.L., Kumar, A., Whitesides, G.M.: Using Micromachining, Molecular Self-Assembly, and Wet Etching to Fabricate 0.1-1-.mu.m-scale structures of Gold and Silicon. *Chem. Mater.* 6, 596–602 (1994). <https://doi.org/10.1021/cm00041a007>
102. Tan, H., Feng, D., Lukey, G.C., Van Deventer, J.S.J.: The behaviour of carbonaceous matter in cyanide leaching of gold. *Hydrometallurgy.* 78, 226–235 (2005).

- <https://doi.org/10.1016/j.hydromet.2005.03.001>
103. Arslan, F., Duby, P.F.: Electrooxidation of gold-bearing sulfide concentrate. *Mining, Metall. Explor.* 20, 10–14 (2003). <https://doi.org/10.1007/BF03403108>
 104. Yue, C., Sun, H., Liu, W.-J., Guan, B., Deng, X., Zhang, X., Yang, P.: Environmentally Benign, Rapid, and Selective Extraction of Gold from Ores and Waste Electronic Materials. *Angew. Chemie.* 129, 9459–9463 (2017). <https://doi.org/10.1002/ange.201703412>
 105. Burdick, J., Alonas, E., Huang, H.-C.: Growth of segmented gold nanorods with nanogaps by the electrochemical wet etching technique for single-electron transistor applications Related content High-throughput templated multisegment synthesis of gold nanowires and nanorods. *Nanotechnology.* 20, 125607 (2009). <https://doi.org/10.1088/0957-4484/20/12/125607>
 106. Eidelloth, W., Sandstrom, R.L.: Wet etching of gold films compatible with high T_c superconducting thin films. *Appl. Phys. Lett.* 59, 1632 (1991). <https://doi.org/10.1063/1.106253>
 107. Grandjean, P., White, R.F., Nielsen, A., Cleary, D., de Oliveira Santos, E.C.: Methylmercury neurotoxicity in Amazonian children downstream from gold mining. *Environ. Health Perspect.* 107, 587–591 (1999). <https://doi.org/10.1289/ehp.99107587>
 108. Malm, O.: Gold Mining as a Source of Mercury Exposure in the Brazilian Amazon. *Environ. Res.* 77, 73–78 (1998). <https://doi.org/10.1006/enrs.1998.3828>
 109. Chudnenko, K., Pal'Yanova, G.: Thermodynamic properties of Ag-Au-Hg solid solutions. *Thermochim. Acta.* 572, 65–70 (2013). <https://doi.org/10.1016/j.tca.2013.08.024>
 110. Okamoto, H., Massalski, T.B.: The Au-Hg (Gold-Mercury) system. *Bull. Alloy Phase Diagrams.* 10, 50–58 (1989). <https://doi.org/10.1007/BF02882176>
 111. Wang, H.-X., Sun, C.-B., Li, S.-Y., Fu, P.-F., Song, Y.-G., Li, L., Xie, W.-Q.: Study on gold concentrate leaching by iodine-iodide. *Int. J. Miner. Metall. Mater.* V olume. 20, (2013). <https://doi.org/10.1007/s12613-013-0730-7>
 112. Angelidis, T.N., Kydros, K.A., Matis, K.A.: A fundamental rotating disk study of gold dissolution in iodine-iodide solutions. *Hydrometallurgy.* 34, 49–64 (1993). [https://doi.org/10.1016/0304-386X\(93\)90080-W](https://doi.org/10.1016/0304-386X(93)90080-W)
 113. Volkert, C.A., Minor, A.M.: Focused Ion Beam Microscopy and Micromachining The FIB Instrument. <https://doi.org/10.1557/mrs2007.62>
 114. Giannuzzi, L.A., Prenitzer, B.I., Kempshall, B.W.: Ion - Solid Interactions. In: *Introduction to Focused Ion Beams*. pp. 13–52. Springer US, Boston, MA (2005)
 115. Phaneuf, M.W.: Applications of focused ion beam microscopy to materials science specimens. *Micron.* 30, 277–288 (1999). [https://doi.org/10.1016/S0968-4328\(99\)00012-8](https://doi.org/10.1016/S0968-4328(99)00012-8)
 116. Doube, M., Klosowski, M.M., Arganda-Carreras, I., Cordelières, F.P., Dougherty, R.P., Jackson, J.S., Schmid, B., Hutchinson, J.R., Shefelbine, S.J.: BoneJ: Free and extensible bone image analysis in ImageJ. *Bone.* 47, 1076–1079 (2010). <https://doi.org/10.1016/j.bone.2010.08.023>
 117. Zuo, J.M., Spence, J.C.H.: *Advanced Transmission Electron Microscopy*. Springer New York, New York, NY (2017)

118. Wiktor, C., Meledina, M., Turner, S., Lebedev, O.I., Fischer, R.A.: Transmission electron microscopy on metal-organic frameworks-a review. (2017). <https://doi.org/10.1039/c7ta00194k>
119. Gu, L.: Aberration Corrected Transmission Electron Microscopy and Its Applications. In: Springer Tracts in Modern Physics. pp. 301–379. Springer Verlag (2018)
120. Dou, P., Kimura, A., Kasada, R., Okuda, T., Inoue, M., Ukai, S., Ohnuki, S., Fujisawa, T., Abe, F., Jiang, S., Yang, Z.: TEM and HRTEM study of oxide particles in an Al-alloyed high-Cr oxide dispersion strengthened ferritic steel with Hf addition. *J. Nucl. Mater.* 485, 189–201 (2017). <https://doi.org/10.1016/j.jnucmat.2016.12.001>
121. Xu, H., Qin, I., Clauberg, H., Chylak, B., Acoff, V.L.: New observation of nanoscale interfacial evolution in micro Cu-Al wire bonds by in-situ high resolution TEM study. *Scr. Mater.* 115, 1–5 (2016). <https://doi.org/10.1016/j.scriptamat.2015.12.025>
122. Pan, B., Xie, H., Wang, Z., Qian, K., Wang, Z.: Study on subset size selection in digital image correlation for speckle patterns. *Opt. Express.* 16, 7037 (2008). <https://doi.org/10.1364/OE.16.007037>
123. Li, J., Malis, T., Dionne, S.: Recent advances in FIB-TEM specimen preparation techniques. *Mater. Charact.* 57, 64–70 (2006). <https://doi.org/10.1016/j.matchar.2005.12.007>
124. Mayer, J., Giannuzzi, L.A., Kamino, T., Michael, J.: TEM Sample Preparation and FIB-Induced Damage. *MRS Bull.* 32, 400–407 (2007). <https://doi.org/10.1557/mrs2007.63>
125. Krekeler, T., Straßer, A. V., Graf, M., Wang, K., Hartig, C., Ritter, M., Weissmüller, J.: Silver-rich clusters in nanoporous gold. *Mater. Res. Lett.* 5, 314–321 (2017). <https://doi.org/10.1080/21663831.2016.1276485>
126. Campbell, W.C.: Energy-dispersive X-ray emission analysis. A review. *Analyst.* 104, 177 (1979). <https://doi.org/10.1039/an9790400177>
127. Sahin, Y., Karabulut, A., Budak, G.: A Practical Method for the Analysis of Overlapped Peaks in Energy Dispersive X-Ray Spectra. *Appl. Spectrosc. Rev.* 31, 333–345 (1996). <https://doi.org/10.1080/05704929608000573>
128. Prencipe, I., Dellasega, D., Zani, A., Rizzo, D., Passoni, M.: Energy dispersive x-ray spectroscopy for nanostructured thin film density evaluatio. *Sci. Technol. Adv. Mater.* 16, 25007 (2015). <https://doi.org/10.1088/1468-6996/16/2/025007>
129. Allen, L.J., D’Alfonso, A.J., Freitag, B., Klenov, D.O.: Chemical mapping at atomic resolution using energy-dispersive x-ray spectroscopy. *MRS Bull.* 37, 47–52 (2012). <https://doi.org/10.1557/mrs.2011.331>
130. Hay, J.L.: Instrumented Indentation Testing. In: Mechanical Testing and Evaluation. pp. 232–243. ASM International (2000)
131. VanLandingham, M.R.: Review of instrumented indentation. *J. Res. Natl. Inst. Stand. Technol.* 108, 249 (2003). <https://doi.org/10.6028/jres.108.024>
132. Oliver, W.C., Pharr, G.M.: Measurement of hardness and elastic modulus by instrumented indentation: Advances in understanding and refinements to methodology. *J. Mater. Res.* 19, 3–20 (2004). <https://doi.org/10.1557/jmr.2004.19.1.3>
133. Bei, H., George, E.P., Hay, J.L., Pharr, G.M.: Influence of Indenter Tip Geometry on

- Elastic Deformation during Nanoindentation. *Phys. Rev. Lett.* 95, 045501 (2005). <https://doi.org/10.1103/PhysRevLett.95.045501>
134. Bouzakis, K.D., Michailidis, N., Hadjiyiannis, S., Skordaris, G., Erkens, G.: The effect of specimen roughness and indenter tip geometry on the determination accuracy of thin hard coatings stress-strain laws by nanoindentation. *Mater. Charact.* 49, 149–156 (2002). [https://doi.org/10.1016/S1044-5803\(02\)00361-3](https://doi.org/10.1016/S1044-5803(02)00361-3)
 135. McElhaney, K.W., Vlassak, J.J., Nix, W.D.: Determination of indenter tip geometry and indentation contact area for depth-sensing indentation experiments. *J. Mater. Res.* 13, 1300–1306 (1998). <https://doi.org/10.1557/JMR.1998.0185>
 136. Fischer-Cripps, A.C.: *Introduction to Contact Mechanics*. Springer US, Boston, MA (2007)
 137. Riccardi, B., Montanari, R.: Indentation of metals by a flat-ended cylindrical punch. *Mater. Sci. Eng. A.* 381, 281–291 (2004). <https://doi.org/10.1016/j.msea.2004.04.041>
 138. Ciavarella, M., Hills, D.A., Monno, G.: The influence of rounded edges on indentation by a flat punch. *Proc. Inst. Mech. Eng. Part C J. Mech. Eng. Sci.* 212, 319–327 (1998). <https://doi.org/10.1243/0954406981521259>
 139. Oliver, W.C., Pharr, G.M.: An improved technique for determining hardness and elastic modulus using load and displacement sensing indentation experiments. (2020). <https://doi.org/10.1557/JMR.1992.1564>
 140. Oliver, W.C., Pharr, G.M.: Measurement of hardness and elastic modulus by instrumented indentation: Advances in understanding and refinements to methodology. *J. Mater. Res.* 19, 3–20 (2004). <https://doi.org/10.1557/jmr.2004.19.1.3>
 141. Hay, J., Herbert, E.: *Measuring the Complex Modulus of Polymers by Instrumented Indentation Testing*. (2013). <https://doi.org/10.1111/j.1747-1567.2011.00732.x>
 142. Sideridis, E., Prassianakis, I.N., Kytopoulos, V.N.: Storage and loss moduli behavior of plasticized epoxy polymers over a frequency and temperature range, and damaging effects assessment by means of the NDT method of ultrasounds and moisture absorption. *J. Appl. Polym. Sci.* 101, 3869–3880 (2006). <https://doi.org/10.1002/app.24525>
 143. Odegard, G.M., Gates, T.S., Herring, H.M.: Characterization of viscoelastic properties of polymeric materials through nanoindentation. *Exp. Mech.* 45, 130–136 (2005). <https://doi.org/10.1007/BF02428185>
 144. Sneddon, I.N.: The relation between load and penetration in the axisymmetric boussinesq problem for a punch of arbitrary profile. *Int. J. Eng. Sci.* 3, 47–57 (1965). [https://doi.org/10.1016/0020-7225\(65\)90019-4](https://doi.org/10.1016/0020-7225(65)90019-4)
 145. Uchic, M.D., Dimiduk, D.M.: A methodology to investigate size scale effects in crystalline plasticity using uniaxial compression testing. *Mater. Sci. Eng. A.* 400–401, 268–278 (2005). <https://doi.org/10.1016/j.msea.2005.03.082>
 146. Uchic, M.D.: Sample Dimensions Influence Strength and Crystal Plasticity. *Science* (80-.). 305, 986–989 (2004). <https://doi.org/10.1126/science.1098993>
 147. Hütsch, J., Lilleodden, E.T.: The influence of focused-ion beam preparation technique on microcompression investigations: Lathe vs. annular milling. *Scr. Mater.* (2014). <https://doi.org/10.1016/j.scriptamat.2014.01.016>

148. Wang, S., Yang, Y., Zhou, L. M., Mai, Y.-W.: Size effect in microcompression of epoxy micropillars. <https://doi.org/10.1007/s10853-012-6513-0>
149. Kupka, D., Lilleodden, E.T.: Mechanical Testing of Solid-Solid Interfaces at the Microscale. *Exp. Mech.* (2012). <https://doi.org/10.1007/s11340-011-9530-z>
150. Kupka, D., Huber, N., Lilleodden, E.T.: A combined experimental-numerical approach for elasto-plastic fracture of individual grain boundaries. *J. Mech. Phys. Solids.* 64, 455–467 (2014). <https://doi.org/10.1016/j.jmps.2013.12.004>
151. Chen, K., Mu, Y., Meng, W.J.: A new experimental approach for evaluating the mechanical integrity of interfaces between hard coatings and substrates. *MRS Commun.* 4, 19–23 (2014). <https://doi.org/10.1557/mrc.2014.3>
152. Mu, Y., Chen, K., Meng, W.J.: Thickness dependence of flow stress of Cu thin films in confined shear plastic flow. *MRS Commun.* 4, 129–133 (2014). <https://doi.org/10.1557/mrc.2014.26>
153. Zhang, X., Zhang, B., Mu, Y., Shao, S., Wick, C.D., Ramachandran, B.R., Meng, W.J.: Mechanical failure of metal/ceramic interfacial regions under shear loading. *Acta Mater.* 138, 224–236 (2017). <https://doi.org/10.1016/j.actamat.2017.07.053>
154. Mu, Y., Zhang, X., Hutchinson, J.W., Meng, W.J.: Measuring critical stress for shear failure of interfacial regions in coating/interlayer/substrate systems through a micro-pillar testing protocol. (2020). <https://doi.org/10.1557/jmr.2016.516>
155. Uchic, M.D., Shade, P.A., Dimiduk, D.M.: Plasticity of Micrometer-Scale Single Crystals in Compression. (2009). <https://doi.org/10.1146/annurev-matsci-082908-145422>
156. Zhang, H., Schuster, B.E., Wei, Q., Ramesh, K.T.: The design of accurate micro-compression experiments. *Scr. Mater.* 54, 181–186 (2006). <https://doi.org/10.1016/j.scriptamat.2005.06.043>
157. Kirchlechner, C., Keckes, J., Motz, C., Grosinger, W., Kapp, M.W., Micha, J.S., Ulrich, O., Dehm, G.: Impact of instrumental constraints and imperfections on the dislocation structure in micron-sized Cu compression pillars. *Acta Mater.* 59, 5618–5626 (2011). <https://doi.org/10.1016/j.actamat.2011.05.037>
158. Choi, Y.S., Uchic, M.D., Parthasarathy, T.A., Dimiduk, D.M.: Numerical study on microcompression tests of anisotropic single crystals. *Scr. Mater.* 57, 849–852 (2007). <https://doi.org/10.1016/j.scriptamat.2007.06.057>
159. Kiener, D., Motz, C., Dehm, G.: Micro-compression testing: A critical discussion of experimental constraints. *Mater. Sci. Eng. A.* (2009). <https://doi.org/10.1016/j.msea.2009.01.005>
160. Soler, R., Molina-Aldareguia, J.M., Segurado, J., Llorca, J., Merino, R.I., Orera, V.M.: Micropillar compression of LiF [111] single crystals: Effect of size, ion irradiation and misorientation. *Int. J. Plast.* 36, 50–63 (2012). <https://doi.org/10.1016/j.ijplas.2012.03.005>
161. Pharr, G.M., Herbert, E.G., Gao, Y.: The Indentation Size Effect: A Critical Examination of Experimental Observations and Mechanistic Interpretations. (2010). <https://doi.org/10.1146/annurev-matsci-070909-104456>
162. Han, C.-S.S.: Influence of the molecular structure on indentation size effect in polymers. *Mater. Sci. Eng. A.* 527, 619–624 (2010). <https://doi.org/10.1016/j.msea.2009.08.033>

163. Wang, S., Yang, Y., Zhou, L.M., Mai, Y.-W.: Size effect in microcompression of epoxy micropillars. <https://doi.org/10.1007/s10853-012-6513-0>
164. Heijboer, J.: Molecular origin of relaxations in polymers. *Ann. N. Y. Acad. Sci.* 279, 104–116 (1976). <https://doi.org/10.1111/j.1749-6632.1976.tb39700.x>
165. Singha, S., Thomas, M., Kulkarni, A.: Complex permittivity characteristics of epoxy nanocomposites at low frequencies. *IEEE Trans. Dielectr. Electr. Insul.* 17, 1249–1258 (2010). <https://doi.org/10.1109/TDEI.2010.5539697>
166. De F. F. Pinheiro, M., Rosenberg, H.M.: Thermal expansion of epoxy-resin/particle composites—a size effect. *J. Polym. Sci. Polym. Phys. Ed.* 18, 217–226 (1980). <https://doi.org/10.1002/pol.1980.180180204>
167. Sideridis, E., Prassianakis, I.N., Kytopoulos, V.N.: Storage and loss moduli behavior of plasticized epoxy polymers over a frequency and temperature range, and damaging effects assessment by means of the NDT method of ultrasounds and moisture absorption. *J. Appl. Polym. Sci.* 101, 3869–3880 (2006). <https://doi.org/10.1002/app.24525>
168. Mansfield, K.F., Theodorou, D.N.: Molecular dynamics simulation of a glassy polymer surface. *Macromolecules.* 24, 6283–6294 (1991). <https://doi.org/10.1021/ma00023a034>
169. Keddie, J.L., Jones, R.A.L., Cory, R.A.: Interface and surface effects on the glass-transition temperature in thin polymer films. *Faraday Discuss.* 98, 219 (1994). <https://doi.org/10.1039/fd9949800219>
170. Prasad, A., Grover, T., Basu, S.: Coarse – grained molecular dynamics simulation of cross – linking of DGEBA epoxy resin and estimation of the adhesive strength. *Int. J. Eng. Sci. Technol.* 2, 17–30 (2010). <https://doi.org/10.4314/ijest.v2i4.59196>
171. Juodkazis, K., Juodkazyte, J., Jasulaitiene, V., Lukinskas, A., Šebeka, B.: XPS studies on the gold oxide surface layer formation. *Electrochem. commun.* 2, 503–507 (2000). [https://doi.org/10.1016/S1388-2481\(00\)00069-2](https://doi.org/10.1016/S1388-2481(00)00069-2)
172. S. Suzuki, Y. Ishikawa, M. Isshiki, Y. Waseda: Native Oxide Layer Formed on the Surface of Ultra High-Purity Iron and Copper investigated by Angle Resolved XPS. *Mater. Trans.* 38, 1004–1009 (1997)
173. Hammer, B., Norskov, J.K.: Why gold is the noblest of all the metals. *Nature.* 376, 238–240 (1995). <https://doi.org/10.1038/376238a0>
174. Sunny, M.C., Sharma, C.P.: Titanium-Protein Interaction: Changes with Oxide Layer Thickness. *J. Biomater. Appl.* 6, 89–98 (1991). <https://doi.org/10.1177/088532829100600107>
175. Martin, J.E., Herzing, A.A., Yan, W., Li, X.-Q., Koel, B.E., Kiely, C.J., Zhang, W.-X.: Determination of the Oxide Layer Thickness in Core-Shell Zerovalent Iron Nanoparticles. (2008). <https://doi.org/10.1021/la703689k>
176. Burke, L.D., Nugent, P.F.: The electrochemistry of gold: I the redox behaviour of the metal in aqueous media. *Gold Bull.* 30, 43–53 (1997). <https://doi.org/10.1007/BF03214756>
177. Canning, N.D.S., Outka, D., Madix, R.J.: The adsorption of oxygen on gold. *Surf. Sci.* 141, 240–254 (1984). [https://doi.org/10.1016/0039-6028\(84\)90209-7](https://doi.org/10.1016/0039-6028(84)90209-7)
178. Putz, B., Milassin, G., Butenko, Y., Völker, B., Gammer, C., Semprimoschnig, C., Cordill,

- M.J.: Combined TEM and XPS studies of metal - polymer interfaces for space applications. *Surf. Coatings Technol.* 332, 368–375 (2017). <https://doi.org/10.1016/j.surfcoat.2017.07.079>
179. Transmission Electron Microscopy: Conventional and Special Investigations of Polymers. In: *Electron Microscopy of Polymers*. pp. 53–85. Springer Berlin Heidelberg, Berlin, Heidelberg (2008)
180. Singh, P., Venugopal, B.R., Nandini, D.R.: Effect of Electron Beam Irradiation on Polymers. *J. Mod. Mater.* 5, 24–33 (2018). <https://doi.org/10.21467/jmm.5.1.24-33>
181. He, P., Zhang, J., Zhou, R., Li, X.: Diffusion bonding technology of a titanium alloy to a stainless steel web with an Ni interlayer. *Mater. Charact.* 43, 287–292 (1999). [https://doi.org/10.1016/S1044-5803\(99\)00008-X](https://doi.org/10.1016/S1044-5803(99)00008-X)
182. Sudharshan Phani, P., Oliver, W.C.: A critical assessment of the effect of indentation spacing on the measurement of hardness and modulus using instrumented indentation testing. *Mater. Des.* 164, 107563 (2019). <https://doi.org/10.1016/j.matdes.2018.107563>
183. Oehlert, G.: *A First Course in Design and Analysis of Experiments*. W. H. Freeman and Company (2000)
184. Snell, J., Montgomery, D.C., Runger, G.C.: Applied Statistics and Probability for Engineers. *J. R. Stat. Soc. Ser. A (Statistics Soc.* 158, 355 (1995). <https://doi.org/10.2307/2983314>
185. Johnson, K.L.: *Contact Mechanics*. Cambridge University Press (1985)
186. Hintsala, E.D., Hangen, U., Stauffer, D.D.: High-Throughput Nanoindentation for Statistical and Spatial Property Determination. *JOM.* 70, 494–503 (2018). <https://doi.org/10.1007/s11837-018-2752-0>
187. Fischer-Cripps, A.C.: Nanoindentation of Thin Films. Presented at the (2004)
188. Chen, X., Vlassak, J.J.: Numerical study on the measurement of thin film mechanical properties by means of nanoindentation. *J. Mater. Res.* 16, 2974–2982 (2001). <https://doi.org/10.1557/JMR.2001.0408>
189. Wen, W., Becker, A.A., Sun, W.: Determination of material properties of thin films and coatings using indentation tests: a review. *J. Mater. Sci.* 52, <https://doi.org/10.1007/s10853-017-1348-3>
190. Doerner, M.F., Nix, W.D.: A method for interpreting the data from depth-sensing indentation instruments. *J. Mater. Res.* 1, 601–609 (1986). <https://doi.org/10.1557/JMR.1986.0601>
191. King, R.B.: Elastic analysis of some punch problems for a layered medium. *Int. J. Solids Struct.* 23, 1657–1664 (1987). [https://doi.org/10.1016/0020-7683\(87\)90116-8](https://doi.org/10.1016/0020-7683(87)90116-8)
192. Saha, R., Nix, W.D.: Effects of the substrate on the determination of thin film mechanical properties by nanoindentation. *Acta Mater.* 50, 23–38 (2002). [https://doi.org/10.1016/S1359-6454\(01\)00328-7](https://doi.org/10.1016/S1359-6454(01)00328-7)
193. Chen, X., Xiang, Y., Vlassak, J.J.: Novel technique for measuring the mechanical properties of porous materials by nanoindentation. (2017). <https://doi.org/10.1557/jmr.2006.0088>
194. Kim, W.S., Yun, I.H., Lee, J.J., Jung, H.T.: Evaluation of mechanical interlock effect on adhesion strength of polymermetal interfaces using micro-patterned surface topography.

- Int. J. Adhes. Adhes. (2010). <https://doi.org/10.1016/j.ijadhadh.2010.05.004>
195. Kahraman, R., Sunar, M., Yilbas, B.: Influence of adhesive thickness and filler content on the mechanical performance of aluminum single-lap joints bonded with aluminum powder filled epoxy adhesive. *J. Mater. Process. Technol.* 205, 183–189 (2008). <https://doi.org/10.1016/j.jmatprotec.2007.11.121>
196. Alexander, M.R., Zhou, X., Thompson, G.E., Duc, T.M., McAlpine, E., Tielsch, B.J.: Functionalized plasma polymer coatings for improved durability of aluminium-epoxy adhesive joints: fractography. *Surf. Interface Anal.* 30, 16–20 (2000). [https://doi.org/10.1002/1096-9918\(200008\)30:1<16::AID-SIA708>3.0.CO;2-J](https://doi.org/10.1002/1096-9918(200008)30:1<16::AID-SIA708>3.0.CO;2-J)
197. Sababi, M., Terryn, H., Mol, J.M.C.: The influence of a Zr-based conversion treatment on interfacial bonding strength and stability of epoxy coated carbon steel. *Prog. Org. Coatings.* 105, 29–36 (2017). <https://doi.org/10.1016/j.porgcoat.2016.11.016>
198. Ochi, M., Takashima, H.: Bonding properties of epoxy resin containing mesogenic group. *Polymer (Guildf)*. 42, 2379–2385 (2001). [https://doi.org/10.1016/S0032-3861\(00\)00588-7](https://doi.org/10.1016/S0032-3861(00)00588-7)
199. Ramamurthi, M., Lee, J.-S., Yang, S.-H., Kim, Y.-S.: Delamination Characterization of Bonded Interface in Polymer Coated Steel using Surface Based Cohesive Model. *Int. J. Precis. Eng. Manuf.* 14, 1755–1765 (2013). <https://doi.org/10.1007/s12541-013-0235-3>
200. Needleman, A.: Some issues in cohesive surface modeling. *Procedia IUTAM.* 10, 221–246 (2014). <https://doi.org/10.1016/j.piutam.2014.01.020>
201. Hassan, M., Ali, A., Ilyas, M., Hussain, G., Haq, I. ul: Experimental and numerical simulation of steel/steel (St/St) interface in bi-layer sheet metal. *Int. J. Light. Mater. Manuf.* 2, 89–96 (2019). <https://doi.org/10.1016/j.ijlmm.2019.03.002>
202. Jabłoński, Ł., Halicka, A.: Influence of surface based cohesive parameters on static performance of concrete composite T-shaped beams. <https://doi.org/10.1051/mateconf/201926208003>
203. Abaqus User's Manual version 6.14. Dassault Systèmes (2014)
204. Minnicino, M.A., Santare, M.H.: Modeling the progressive damage of the microdroplet test using contact surfaces with cohesive behavior. *Compos. Sci. Technol.* 72, 2024–2031 (2012). <https://doi.org/10.1016/j.compscitech.2012.09.009>
205. Bascom, W.D., Timmons, C.O., Jones, R.L.: Apparent interfacial failure in mixed-mode adhesive fracture. *J. Mater. Sci.* 10, 1037–1048 (1975). <https://doi.org/10.1007/BF00823223>
206. Cooper, G.A., Sillwood, J.M.: Multiple fracture in a steel reinforced epoxy resin composite. *J. Mater. Sci.* 7, 325–333 (1972). <https://doi.org/10.1007/BF00555634>
207. Hine, P.J., Muddarris, S. El, Packham, D.E., Muddarris, S.E.: Adhesion of microfibrous surfaces on steel and copper to epoxy resins. *J. Adhes. Sci. Technol.* 1, 69–78 (1987). <https://doi.org/10.1163/156856187X00085>
208. Gupta, S., Hydro, R.M., Pearson, R.A.: Fracture behaviour of isotropically conductive adhesives. In: *Proceedings of 3rd International Conference on Adhesive Joining and Coating Technology in Electronics Manufacturing 1998 (Cat. No.98EX180)*. pp. 38–43. IEEE (1998)

-
209. Liu, L.-Z., Ye, X.-L., Jin, H.-J.: Interpreting anomalous low-strength and low-stiffness of nanoporous gold: Quantification of network connectivity. *Acta Mater.* 118, 77–87 (2016). <https://doi.org/10.1016/j.actamat.2016.07.033>
210. Ziehmer, M., Lilleodden, E.T.: The isothermal evolution of nanoporous gold from the ring perspective - an application of graph theory. *Acta Mater.* 199, 669–679 (2020). <https://doi.org/10.1016/j.actamat.2020.08.026>
211. Tai, M.C., Gentle, A., Arnold, M.D., Cortie, M.B.: Optical in situ study of de-alloying kinetics in nanoporous gold sponges. *RSC Adv.* 6, 85773–85778 (2016). <https://doi.org/10.1039/C6RA18272K>
212. Qian, L.H., Chen, M.W.: Ultrafine nanoporous gold by low-temperature dealloying and kinetics of nanopore formation. *Appl. Phys. Lett.* (2007). <https://doi.org/10.1063/1.2773757>
213. Briot, N.J., Kosmidou, M., Dingreville, R., Hattar, K., Balk, T.J.: In situ TEM investigation of self-ion irradiation of nanoporous gold. *J. Mater. Sci.* 54, 7271–7287 (2019). <https://doi.org/10.1007/s10853-019-03385-z>
214. Parida, S., Kramer, D., Volkert, C.A., Rösner, H., Erlebacher, J., Weissmüller, J.: Volume Change during the Formation of Nanoporous Gold by Dealloying. *Phys. Rev. Lett.* 97, 035504 (2006). <https://doi.org/10.1103/PhysRevLett.97.035504>
215. Gontard, L.C., Dunin-Borkowski, R.E., Ozkaya, D.: Three-dimensional shapes and spatial distributions of Pt and PtCr catalyst nanoparticles on carbon black. *J. Microsc.* 232, 248–259 (2008). <https://doi.org/10.1111/j.1365-2818.2008.02096.x>
216. Cheng, Y., Yao, H., Duan, J., Xu, L., Zhai, P., Lyu, S., Chen, Y., Maaz, K., Mo, D., Sun, Y., Liu, J.: Surface Modification and Damage of MeV-Energy Heavy Ion Irradiation on Gold Nanowires. *Nanomaterials.* 7, 108 (2017). <https://doi.org/10.3390/nano7050108>
217. Akita, T., Kohyama, M., Haruta, M.: Electron Microscopy Study of Gold Nanoparticles Deposited on Transition Metal Oxides. *Acc. Chem. Res.* 46, 1773–1782 (2013). <https://doi.org/10.1021/ar300259n>
218. Zhu, X.Q., Feng, Q., Liu, D.Z., Nie, A.M., Liu, J.B., Zhang, X.B., Geng, L.M.: In situ high resolution transmission electron microscopy investigation of deformation mechanism in sub-10-nm Au crystals. *Mater. Sci. Technol.* 30, 774–781 (2014). <https://doi.org/10.1179/1743284713Y.0000000408>
219. Oh, S.H., Rentenberger, C., Im, J., Motz, C., Kiener, D., Karnthaler, H.-P., Dehm, G.: Dislocation plasticity of Al film on polyimide investigated by cross-sectional in situ transmission electron microscopy straining. *Scr. Mater.* 65, 456–459 (2011). <https://doi.org/10.1016/j.scriptamat.2011.06.001>
220. Beets, N., Stuckner, J., Murayama, M., Farkas, D.: Fracture in nanoporous gold: An integrated computational and experimental study. *Acta Mater.* 185, 257–270 (2020). <https://doi.org/10.1016/j.actamat.2019.12.008>
221. Chng, A.C., O'Day, M.P., Curtin, W.A., Tay, A.A.O., Lim, K.M.: Fracture in confined thin films: A discrete dislocation study. *Acta Mater.* 54, 1017–1027 (2006). <https://doi.org/10.1016/j.actamat.2005.10.038>
222. Mughrabi *, H., Pschenitzka, F.: Constrained glide and interaction of bowed-out screw dislocations in confined channels. *Philos. Mag.* 85, 3029–3045 (2005).

- <https://doi.org/10.1080/14786430500079975>
223. Zhang, Z., Shao, C., Wang, S., Luo, X., Zheng, K., Urbassek, H.M.: Interaction of Dislocations and Interfaces in Crystalline Heterostructures: A Review of Atomistic Studies. *Crystals*. 9, 584 (2019). <https://doi.org/10.3390/cryst9110584>
224. Han, X., Ghoniem *, N.M.: Stress field and interaction forces of dislocations in anisotropic multilayer thin films. *Philos. Mag.* 85, 1205–1225 (2005). <https://doi.org/10.1080/14786430412331331907>
225. Lu, Y., Song, J., Huang, J.Y., Lou, J.: Surface dislocation nucleation mediated deformation and ultrahigh strength in sub-10-nm gold nanowires. *Nano Res.* 4, 1261–1267 (2011). <https://doi.org/10.1007/s12274-011-0177-y>
226. Kacher, J., Eftink, B.P., Robertson, I.M.: In Situ Transmission Electron Microscopy Investigation of Dislocation Interactions. In: *Handbook of Mechanics of Materials*. pp. 131–166. Springer Singapore, Singapore (2019)
227. Detsi, E., De Jong, E., Zinchenko, A., Vuković, Z., Vuković, I., Punzhin, S., Loos, K., ten Brinke, G., De Raedt, H.A., Onck, P.R., De Hosson, J.T.M.: On the specific surface area of nanoporous materials. *Acta Mater.* 59, 7488–7497 (2011). <https://doi.org/10.1016/j.actamat.2011.08.025>

Curriculum Vitae

Family name	Pereira Hablitzel
Given name	Murilo
Date of birth	15.11.1990
Place of birth	Florianópolis, Brazil
01.93 – 12.95	Primary school in Palhoça, Brazil
01.96 – 12.04	Middle school in São José, Brazil
01.05 – 12.07	High school in São José, Brazil
01.08 – 09.13	Federal University of Santa Catarina, Bachelor in Materials Science and Engineering
09.13 – 01.17	Whirlpool Corporation, Materials Development Engineer
02.14 – 03.16	Federal University of Santa Catarina, Master in Materials Science and Engineering
02.17 – 06.21	Helmholtz-Zentrum Hereon, PhD candidate in the department of Experimental Materials Mechanics
07.21 – 01.22	Dow Chemical Company, Senior TS&D Specialist